

**Quasi-distributed Optical
Remote Sensing for Temperature,
Strain and Gas Leakage**

Mifang Lu

Electronic and Photonic Systems Engineering

A thesis submitted for the degree of PhD

August, 2014

Abstract

This dissertation studies on quasi-distributed optical fiber sensing system that is capable of tele-monitoring the change of temperature, pressure and the occurrence of gas leakages. Three techniques are involved, an improvement technique over the optical pulse correlation sensing continuously studied in our lab, an quasi-distributed optical fiber gas sensing method based on gas spectroscopy and region selectable technique, and a quasi-distributed plastic optical fiber gas sensing concept using gas sensitive material coated POF and OTDR.

Optical pulse correlation sensing system utilizes the time modulation of the optical signal propagating in the optical fiber transmission line to monitor the temperature, stress or pressure around the optical fiber. It provides high accuracy (sub-picosecond), large range linear response ($\sim 10\text{ps}$) and high time resolution ($\sim 0.01\text{ps}$). However, the sensing signal suffers from polarization fluctuation over long transmission line. Chapter 2 proposes a polarization scrambled pulse train (PSP) to reduce the polarization impact in remote fiber sensing, generating a polarization-insensitive pulse correlation measurement. In the PSP, the polarization state of each pulse is randomized. The polarization scrambling mechanism in pulse correlation measurement with PSP is theoretically explained, experimental generation of PSP has been specifically described, and the polarization fluctuation resistance of PSP has been experimentally demonstrate. Moreover, the fiber strain measurement using PSP-based pulse correlation tele-monitoring under various polarization states on a multi-region fiber sensing system has been implemented. The results show good stability against polarization fluctuation, indicating that the technique has great potential for use in harsh environment tele-monitoring.

Chapter 3 presents a novel optical gas tele-monitoring concept to construct a long distance

ABSTRACT

region selectable gas sensing, which can address gases of single and/or different types at multiple locations. The technique is based on the gas absorption spectroscopy in near infrared area and region selectable technique. Constructed with a wavelength scanning LD, optical fibers, gas sensing regions and region selectors, the technique is able to detect the occurrences, locations and types of the gas leakages along the transmission line from a long distance monitoring center. By accurate power monitoring, it is possible to analyze the concentration of the gas leakage. A multi-region tele-monitoring experiment using FBG monitor as spectroscopy unit, long propagation fibers, gas cells as leakage sensing regions and FBGs as region selectors is demonstrated. Available numbers and coverage of multi-sensing regions are estimated using loss of sensing unit and propagation. In addition, a technique to extend the number of the sensing regions is proposed and experimentally demonstrated. The technique provides long distance (\sim tens of km) sensing, super low pressure gas detection (10 Torr), and easy operation, showing potential to be applied to long distance lightweight fiber optic wide-region gas sensing.

Chapter 4 gives a gas detection concept using POF coated with gas sensitive chemical material whose refractive index is reduced in the presence of hydrocarbon gases owing to gas-absorption swelling. Combining with OTDR technique and silica fibers, a quasi-distributed gas sensing can be built which provides a practical possibility to be applied in hydrocarbon gas occurrence and location monitoring. The working principle of the gas recognition is explained. A pre-demonstration utilizing an OTDR, GI POFs, GI silica fibers, alcohol and water are completed.

A summary is presented in chapter 5 including a conclusion of the current work and an outlook for future study.

Contents

1	Introduction	1
1.1	Background	1
1.1.1	Development history of optical fibers	1
1.1.2	Types of optical fiber	3
1.2	Optical fiber sensor	6
1.2.1	Optical fiber sensor configurations and types	7
1.2.2	Optical fiber remote sensing	11
1.2.3	Common application of optical fiber sensors	13
1.3	Outline of the thesis	16
2	Polarization-insensitive Pulse Correlation Measurement for Remote Fiber Sensing Using Polarization Scrambled Pulses	21
2.1	Introduction	22
2.1.1	Optical fiber sensing based on pulse correlation measurement	22
2.1.2	Problem of Optical fiber sensing based on pulse correlation measurement	24
2.2	Pulse correlation measurement using collinear SHG process	24
2.3	Polarization fluctuation of pulse correlation term and its suppression	27
2.3.1	Polarization-induced fluctuation of pulse correlation term in SHG output	27
2.3.2	Suppression of the polarization fluctuation in the pules correlation measurement	29

CONTENTS

2.3.3	Experimental generation of PSP and stabilization of pulse correlation measurement	31
2.4	PSP-Based Wide-Region Optical Pulse Correlation Sensing	34
2.4.1	Principle of pulse correlation measurement for fiber strain/temperature sensing	34
2.4.2	Impact of polarization instability on tele-monitoring and improvements of optical pulse correlation technique using PSP light source	36
2.5	Experimental Results of Correlation Measurement under Various Polarization Conditions	39
2.5.1	Sensitivity stabilization against polarization instability	39
2.5.2	Strain measurement using PSP-based sensing for tele-monitoring	42
2.6	Discussion	43
2.6.1	Propagation loss	44
2.6.2	Chromatic dispersion	46
2.6.3	Sensing length and number of sensing regions	50
2.7	Summary	50
3	Quasi-distributed region selectable gas sensing for long distance pipeline maintenance	53
3.1	Introduction	54
3.2	Concept of region selectable gas sensing by tele-spectroscopy	56
3.2.1	Gas absorption spectroscopy and tele-spectroscopy	56
3.2.2	Concept of region selectable gas sensing by tele-spectroscopy	57
3.3	Tele-spectroscopy by scanning-LD, FBGs and fibers	58
3.3.1	Schematic of tele-spectroscopy	58
3.3.2	Tele-spectroscopy experiment and analysis	60
3.3.3	Discussion of tele-spectroscopy technique	61
3.3.3.1	Impact of absorption line broadening under varied temperatures and pressures	61

3.3.3.2	Impact of FBG instability	64
3.4	Multi-region gas sensing demonstration	64
3.4.1	Setup of three-region gas sensing demonstration	64
3.4.2	Results of three-region gas sensing demonstration	66
3.4.3	Analysis of multi-sensing situation	68
3.5	Long distance multi-region gas sensing	69
3.5.1	Demonstration of multi-region tele-monitoring	69
3.5.2	Impact of optical loss in the design of gas sensing	71
3.6	Extension of the number of sensing regions	72
3.6.1	Wavelength shift of FBG sensor monitor	73
3.6.2	Principle of the number extension of sensing regions	75
3.6.3	Experimental demonstration of sensing region extension technique	75
3.6.3.1	Experimental measurement of displayed wavelength shift on FBG sensor monitor	76
3.6.3.2	Experimental setup	76
3.6.3.3	Experimental results	78
3.7	Summary	80
4	Plastic Optical Fiber Gas Sensing using OTDR	81
4.1	Introduction	81
4.2	Principle and scheme of POF gas sensing using OTDR	83
4.2.1	Optical Time Domain Reflectometer OTDR [1]	83
4.2.2	Operation principle of the POF sensor head	85
4.2.3	Scheme of POF gas sensing using OTDR	88
4.3	Pre-demonstration of POF gas sensing using OTDR	91
4.3.1	Set-up	93
4.3.2	Results of experimental demonstration	95
4.4	Summary	99

CONTENTS

5 Conclusions	101
5.1 Summary	101
5.2 Outlooks	103
References	107
Appendix A The development of optical fiber sensing based on pulse correlation in the lab	115
List of Figures	117
List of Tables	121
Glossary	123
Acknowledgement	125
Publications	127

Chapter 1

Introduction

1.1 Background

Except for the rapid development of semiconductor lasers in 1960, the prosperity of optical fiber sensors benefits from the increasingly perfecting of optical fiber technology began in 1966 [2]. Since the initial experiments on low loss optical fibers being used for sensor purpose in 1970s, the field has continued to progress and has developed enormously.

1.1.1 Development history of optical fibers

When light rays incident into a water jet at a glancing angle, the total reflection of light at the common surface of two media of different reflective indices - water and air, would trap the light rays in the liquid, thereby the light can be guided downward along the flowing water generating a beautiful illuminated appearance [3], as shown in Fig 1.1. It is a famous demonstration of total internal reflection guiding light along flowing liquid invented in 1841. In the mid-nineteenth century, the physical phenomenon of total internal reflection has been widely used in light guiding and illumination. Light pipes for illumination, illuminating glass rods for medical utility, e.g., dental illuminator, and surgery illumination, were invented by physicists.

Glass fibers were made in 1920s, however they were not practical for information transmission as a result of light leakage until the deposition of a cladding layer around the fiber core

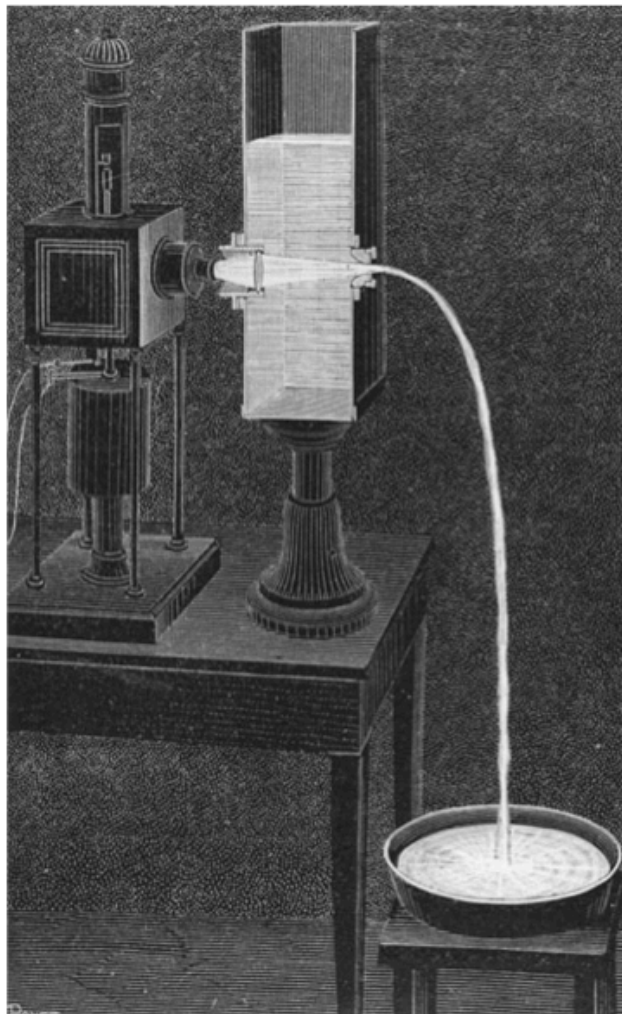


Figure 1.1 Fountain sparkles with light from an arc lamp, illustrated by Colladon in 1884 [3].

dramatically reduced the transmission loss to 1000dB/km [4]–[6]. In 1966, K . C. Kao, analyzed the light transmission in a dielectric-fiber waveguide with a circular cross-section showing glass or silica fibers can be potentially used in optical communication [7]. Following the suggestion of the paper [7], Corning corporation successfully reduced the transmission loss of silica fiber to below 20dB/km in 1970 [8]. In 1979, optical fibers with a transmission loss of 0.2dB/km at the 1.55 μ m spectrum region [9] led to the revolution in the field of light wave technology [10]. By the end of 1990s, fibers were being used worldwide not only for signal transmission but also for making many useful optical devices in the form of couplers, gratings, amplifiers, and sensors.

1.1.2 Types of optical fiber

An optical fiber consists of a cylindrical core with diameter less than 1mm, which is surrounded by a cladding whose refractive index is lower than that of the core. According to the refractive index change at the core-cladding interface, optical fibers are known as *step-index fibers* with abrupt index change, and *graded-index fibers* with a gradual refractive index reduction in the core. The refractive index difference between the core and the cladding make total internal reflection possible which confines light to the core of an optical fiber. In this section, a simple introduction of typical types of optical fibers is given from the application perspective.

Silica fibers

Both the core and the cladding of silica fibers are made using silicon dioxide, SiO₂ or silica as the basic materials. The difference of their refractive indexes is realized by the dopants in the core, or the cladding or both of them. Schematics of the structures of step-index fibers and graded-index fibers are shown in Fig 1.2 and Fig 1.3. For step-index fibers, the refractive index of the core is in the range from 1.44 to 1.46, depending on the wavelength. Examples of standard core and cladding diameters of step-index fibers are 8/123, 50/125, 62.5/125, 85/125, 100/140 (units of μ m) [11]. Especially, silica fibers show the least attenuation of 0.2dB/km at the wavelength of 1550nm.

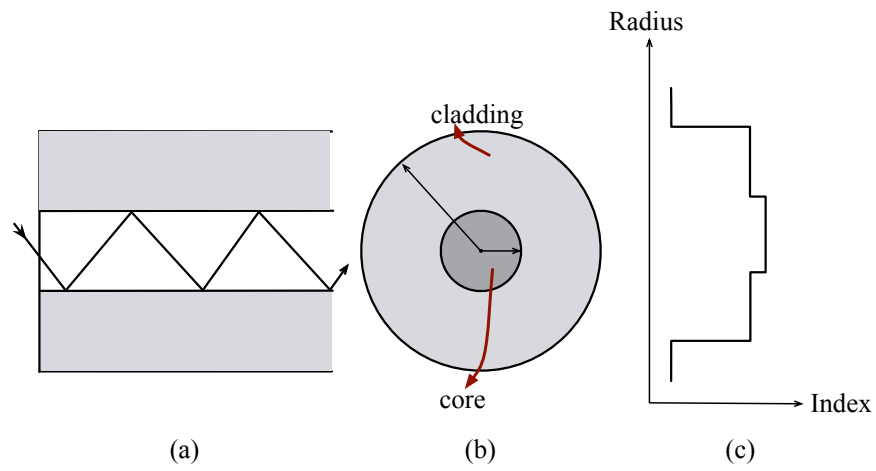


Figure 1.2 Structure of step-index fibers. (a) Light propagation. (b) Cross section. (c) Refractive index distribution.

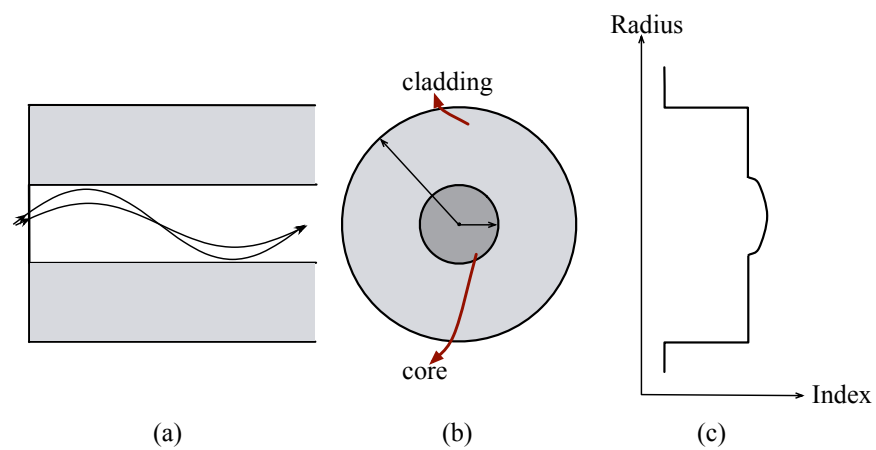


Figure 1.3 Structure of graded-index fibers. (a) Light propagation. (b) Cross section. (c) Refractive index distribution.

Plastic optical fibers

With the need of high bandwidth connectivity over short distance, known as the ‘last hundred meters’, in optical fiber infrastructure [12], plastic optical fibers (POFs) have caused tremendous interest since 1990s and growing quickly.

POFs has larger diameter than silica fibers do, the core diameter varing from 10 to 1000 μm and the cladding diameter approaching 200 μm , resulting in higher numerical aperture and higher coupling efficiency. Moreover, POFs are more flexible than silica fibers, and optical devices for POFs are cheaper than those for silica fibers [13]. Initially, POFs had large transmission loss, $\geq 50\text{dB/km}$ [14]. But the technology developed so quickly that the transmission loss of POFs are reduced to less than 20dB/km, acceptable transmission loss exhibition in long distance region ($\sim 1310\mu\text{m}$) enabling even more extensive application. Especially, Graded-index POFs (GI-POF) have been demonstrated to provide an ideal solution for transferring data among computers since they can greatly reduce mode dispersion, allowing transmission at faster than 1Gbps.

Plastic optical fibers use plastics in the form of organic polymers to make both the core and the cladding. Based on the core material, plastic optical fibers can be classified into fibers with PMMA (polymathy methacrylate) core, fibers with PS (polystyrene) core, fibers with PC (polycarbonate) core, and fibers with deuterated core [15], amorphous fluorinated polymer poly (perfluoro-butenylvinyl ether), and perfluoro-butenylvinylether (PFBVE) can be used to make POF as well [10].

Holey and photonic-crystal fibers

A holey fiber is a pure silica-glass fiber that contains multiple cylindrical wire holes parallel to, and along the length of, its axis. The holes are organized in a regular periodic pattern. As illustrated in Fig 1.4, the core is defined by a defect, or fault in the periodic structure, such as a missing hole, a hole of a different size, or and an extra hole [16].

The idea of photonic-crystal fibers emerged that light could be trapped inside a hollow fiber core by creating a periodic wavelength-scale lattice of microscopic holes in the cladding

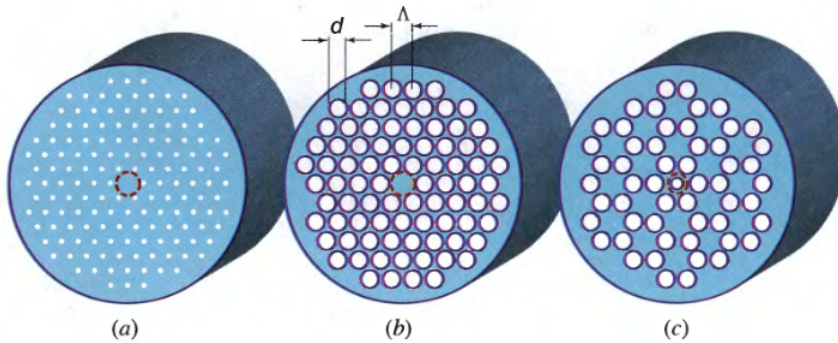


Figure 1.4 Scanning electron micrographs of microstructure fibers

glass [17]. As shown in Fig 1.4(b), the small hole microstructure has a dispersion diagram with photonics bandgaps. If the optical frequency lies within the photonics bandgap, propagation through the cladding is prohibited and the fiber serves as a photonic-crystal waveguide [16]. It is possible to produce the microstructure in air-glass PCF to accuracies of 10nm on the scale of $1\mu\text{m}$, allowing the control of key optical properties such as nonlinearity, birefringence and dispersion [18].

The versatile characteristics of PCFs allow their wide application areas, such as high-power and energy transmission [19]–[23], fiber lasers and amplifiers [24], [25], Brillouin scattering [26]–[29], and the analysis of gas in the fiber core [30]–[32].

1.2 Optical fiber sensor

Optical fiber sensors can be used in harsh measurement situations where conventional sensors are not well suitable to use because of the multiple advantages of optical fiber sensors, such as electromagnetic interference (EMI) immunity, lightweight, compact, and high flexibility. Up to now, plastic optical fibers (POFs) based optical sensors are drawing increasingly attention owing to their high flexibility allowing the sensors to withstand large strains, and a so-called “memory effect” of POF-based sensors that POFs are able to store the information of applied large strain due to their plastic deformation [33], [34].

The working principle of optical fiber sensors, some typical examples of fiber sensors, as well

as the common applications of optical fiber sensors are briefly introduced in this section.

1.2.1 Optical fiber sensor configurations and types

In an optical fiber sensor, the optical parameters of working optical waves, e.g., time, wavelength, power, phase and polarization are modulated by the variation of the temperature or pressure around the optical fiber, as shown in Fig 1.5. By analyzing the modulated optical parameter, we can estimate the variation of the temperature or pressure.

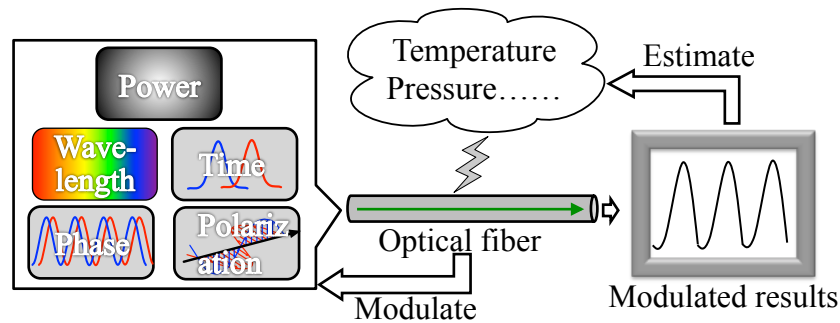


Figure 1.5 Principle of optical fiber sensors

Intensity-based optical fiber sensor

Intensity-based optical fiber sensor realizes the sensing according to the optical field distribution or the power loss caused by micro- or macro-bending. Since the optical field distribution is related to the longitudinal and axial distance between the transmitter fiber and a receiver fiber. By using a transducer, the distance between the transmitter fiber and monitoring fiber was modulated by the environment such as temperature and pressure, so the optical power detected by the receiving fiber was modulated and the sensing was realized. For the micro-and macro-bending sensor, the optical intensity is modulated by the distortion of fiber resulted in the power loss. Intensity-based fiber sensors have simple structure. However, they have a series of limitations imposed by various losses in the system that are not caused by the environmental change to be measured. Potential error sources include variable losses due to connectors, splices, and mechanical creep and misalignment of light sources and detectors.

Optical fiber interferometer

The optical fiber interferometer is developed based on coherent theory of optical beams. The interference fringe visibility is related to the phase difference between coherent beams. There are mainly four structures: Mach-Zehnder interferometer (MZI), fiber optic gyroscope (FOG) based on Sagnac interference, Michelson interferometer, and Fabry-Perot interferometer (FPI).

Fiber optic gyroscope obtained the contemporary development with optical fiber hydrophone, which was used to measure the rotation as a replacement of ring laser gyroscope firstly developed by V.Vali and R. E. Shorthill in 1976 [18]. Extrinsic Fabry-Perot interferometer (EFPI) has high resolution and small size, which has been widely used in health monitoring of large scale civil engineering structures, acoustic detection and aircraft [19, 20]. In 1996, Bhatia et al. demonstrated an absolute EFPI system for measuring values of cavity length d ranging from 40 to 300 μm with a demonstrated spectral resolution of 0.1 nm [21]. In 2001 M. Schmidt. et.al. proposed a fiber-optic extrinsic Fabry-Perot interferometer strain sensor with 50 pm displacement [22]. However, EFPI sensors are limited by the weak interferometric signal and difficulty in multiplexing. At present, many researchers are concentrated to solve these problems [23-25].

Fiber Bragg Gratings

When optical fibers are exposed to intense radiation from a laser, their optical properties can be changed permanently. This photosensitive effect can be used to induce periodic changes in the refractive index along the fiber length, resulting in the formation of fiber grating, which includes the Fiber Bragg grating (FBG) and the long-period fiber grating (LPG) [2], [35]–[38].

FBG is known as an effective wavelength selection component. Under phase matching conditions, a fiber Bragg grating (FBG) couples the forward propagating core mode to the backward propagating core mode. A LPG, which has a period Λ lies from hundreds of micrometers to millimeters, can couple the forward propagating core mode to one or a few of the forward propagating cladding modes. Other types of fiber gratings includes chirped fiber gratings, tilted fiber gratings, and sampled fiber gratings.

Grating based sensors have wide applications, especially in the area of distributed embedded

sensing in materials for creating smart structures. However, FBGs are the most widely used as they are well suited to quasi-distributed point measurements of strain or temperature at known positions in an optical fiber network, with simple configuration and high sensitivity. An remarkable characteristic of FBG sensors is their multiplexing ability [39], where by encoding directly in wavelength terms, the output does not depend on other physical parameters of the system, e.g., intensity, fiber or coupling loss, or input power. Thereby, measurands, such as temperature, strain, or gas absorption [40], can be determined by the corresponding wavelength associated with a particular spatial location.

Brillouin Optical Time-domain Reflectometer (BOTDR)

BOTDR is a sensor based on the Brillouin gain in an optical fiber. When two lasers, one is defined as the probe laser and the other is pump laser, are launched into an optical fiber, Brillouin effect will occur if the pump laser frequency is greater than that of the probe laser by the Brillouin frequency shift; the probe laser will be amplified, experiencing Brillouin gain. Since the Brillouin frequency shift depends on the environment around the fiber such as temperature or the strain, the sensing is realized. If the probe intensity emerging from the fiber is monitored following the launch of a pump pulse, an increase in the intensity will be observed whenever Brillouin gain occurs. The time delays between the launch of the pump pulse and these increases in the received probe signal correspond to round-trip times for light traveling to and from the regions of gain. These times provide the position information. Therefore the distribution sensing is available. BOTDR is powerful to realize the high-sensitivity distribution monitoring in long-range, however, its response time is required to be several minutes. So it is a little difficult to realize the real-time monitoring.

Optical pulse correlation measurement

In an optical fiber sensor, the environmental change around the optical fiber, such as temperature, pressure, etc, will cause the fiber to longitudinally extend, leading to propagation time become longer than expectation, as shown in Fig 1.6. The time extension, called time drift or time delay in this article, contains abundant informations about the ambient change. Thereby,

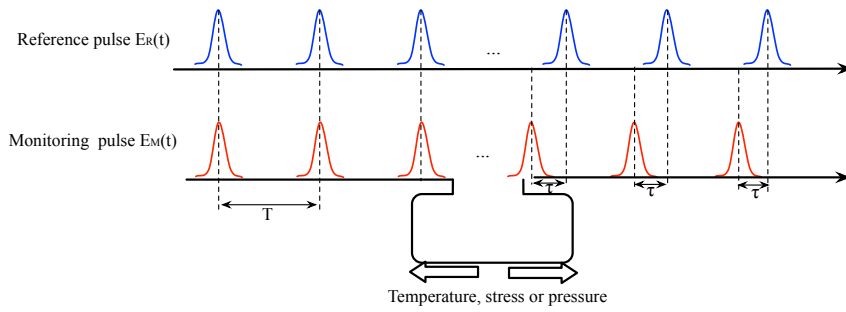


Figure 1.6 Time drift in optical fibers.

the monitoring of the time delay is valuable for understanding the environment condition.

Optical pulse correlation sensing is an effective way to monitor the environmental change around the fiber through the propagation time in the transmission line [41]–[43].

In an optical pulse correlation measurement, a monitoring pulse which reflected back from the monitoring region would be detected by an optical receiver where it going to correlate with a reference pulse that comes from the same light source with the monitoring pulse. The time delay τ is related to the overlapped area of the reference pulse and the monitoring pulse, as shown in Fig 1.7. The environmental change can be demodulated by analyzing the time delay τ .

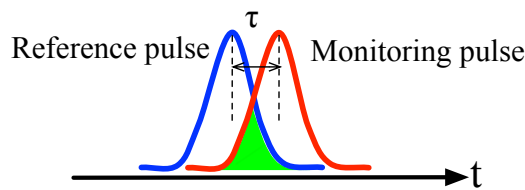


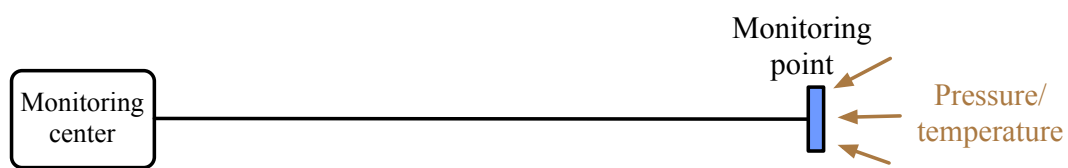
Figure 1.7 Pulse correlation measurement

Pulse correlation measurement provides high accurate, large range linear response. It is an continuous study of our lab [41]–[49], and it is part of the study of this thesis as well.

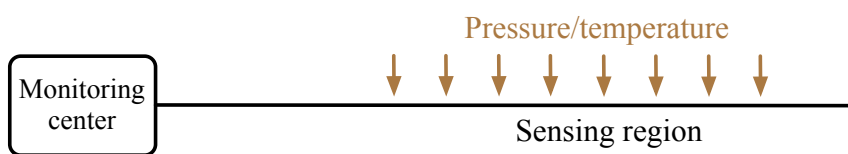
1.2.2 Optical fiber remote sensing

Optical fiber sensors are widely used in the measurement of various measurands, such as strain [50], temperature [51], and pressure [52]. Various optical fiber sensing techniques have been developed, including fiber Bragg grating sensors [53], fiber-optic gyroscopes [54], and fiber-optic current sensors [55].

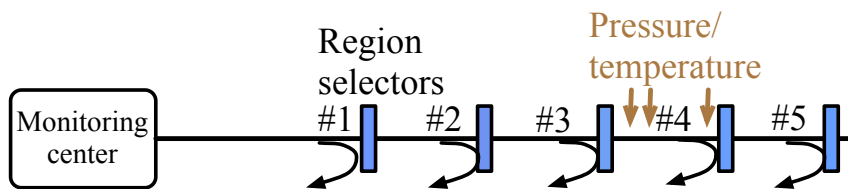
One of the most popular sensor system is point sensor, which is used to measure a particular measurand at a particular location, as shown in Fig 1.8(a). Point sensors are widely used in the measurement of temperature, pressure, acceleration, etc. Alternatively, a sensor system might be designed to be able to monitor the measurand along the length of the fiber, and these sensor systems are known as distributed sensing, as shown by Fig 1.8(b). Distributed sensing employs the nonlinear effects in optical fibers, such as Brillouin scattering, Raman scattering or Rayleigh scattering. Optical Time Domain Reflectometer(OTDR) is one successful example of distributed sensing. Besides point sensor and distributed sensing, there is a sensing system can detect the measurand at particular and pre-determined points along the length of a fiber network, known as quasi-distributed sensing, as shown in Fig 1.8(c). Quasi-distributed sensing can be widely used in temperature or pressure measurement. Fiber Bragg grating (FBG) is one typical optical components used to realized quasi-distributed sensing.



(a) Point sensor.



(b) Distributed sensing.



(c) Quasi-distributed sensing.

Figure 1.8 Configurations of optical fiber sensors.

Distributed sensors

Distributed sensors rely on the Raman, Brillouin, or Rayleigh back scattering. The measurand, typically temperature or pressure, can be revealed by demodulating the backscattered radiation produced by a forward-traveling optical beam [56], [57].

The returned intensity of Rayleigh backscattering represents the intensity arrived at the scattering point. OTDR is one of the most well-developed and commercialized distributed sensing using Rayleigh backscattering has become a standard technique for testing optical fiber links [58], [59].

Brillouin scatter is usually used in the frequency domain. The peak offset frequency for spontaneous/stimulated Brillouin is measured and is a unique function of the acoustic velocity, which is related to the temperature and strain (In fact, the Brillouin frequency shift in an optical fiber depends linearly on the fiber strain [60]–[63]). The disadvantage of the technique is that it suffers from the cross correlation problem as the Brillouin frequency shift depends on both the temperature and strain.

Raman scatter probes the optical phonon spectrum and this in turn can give a unique measure of the temperature at the scattering point. Raman-distributed temperature sensor system is well developed and commercialized. One typical example is the Distributed Anti-Stokes Raman Thermometer (DART), in which a intense laser pulse is used to yield spontaneous Raman scattering in the fiber, resulting Anti-Stokes and Stokes photons a produced along the fiber [2], [64].

1.2.3 Common application of optical fiber sensors

Optical fiber sensors are widely used in the measurement of temperature, pressure, acoustic, strain, displacement, rotation, current/voltage, etc. Thereby, optical fiber sensors have found applications in the fields of Structural health monitoring (SHM), deep sea monitoring, gas detection, etc. As shown in Fig 1.9, Fig 1.10, and Fig 1.11.

Optical fiber sensors for structural health monitoring

The definition of structural health monitoring (SHM) *refers to the use of in-situ, continuous or regular (routine) measurement and analyses of key structural and environmental parameters under operating conditions, for the purpose of warning impending abnormal states or accidents at an early stage to avoid casualties as well as giving maintenance and rehabilitation advice* [65], [66]. SHM requires small, durable sensors able to do multi-point monitoring, with electrical or magnetic interference (EMI). Optical fiber sensors shows intrinsic advantages in this area, such as flexibility, embeddability, multi region and EMI immunity. Fabry-Perot sensors, Fiber Bragg gratings (FBGs), OTDR and BOTDR are the most commonly used optical fiber sensors in this area.

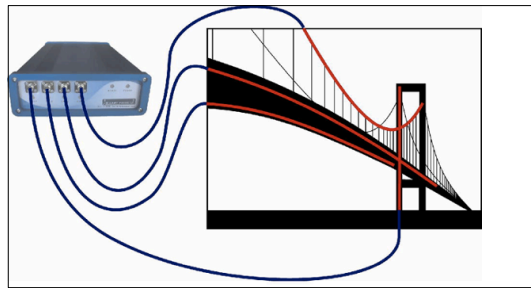


Figure 1.9 Optical fiber sensors for civil structure measurement.

Optical fiber sensors for deep sea

Optical fiber sensors can be used to in deep sea sensor network where optical fiber sensors are installed beyond 1500 meters depth for servicing smart sensors, to monitor the physical parameters, such as pressure and temperature, as shown in Fig 1.10.

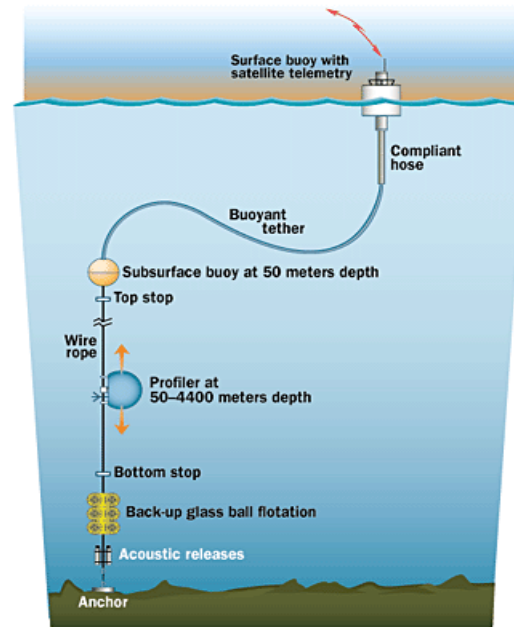


Figure 1.10 Optical fiber sensors used in deep sea monitoring.

Optical fiber sensors for gas detection

There are two genetic gas detection methods using optical fibers. The first is gas absorption spectroscopy, and the second is the combination of chemical sensor heads with optical fiber sensing. Fig 1.11 is a schematic of optical fiber gas detection.

The principle of gas absorption spectroscopy is that a laser output is scanned through an absorption line of the gas species of interest and as the wavelength is scanned the absorption through the gas is measured [57]. Gas absorption are strong in the mid infrared range ($3-7\mu\text{m}$). In the near infrared range ($1-2\mu\text{m}$), the absorption is typically 1-2 orders of magnitude weaker than the mid infrared fundamental. However, much of this weakness can be compensated through the availability of higher power sources and fundamentally better optical detection systems. Techniques using gas absorption spectroscopy requires a gas cell where the propagation light and the gas to be detected can interact with each other, D fibers and hollow core fibers suitable to provide such a function. Nevertheless, multi region detection based on gas absorption spectroscopy are barely realized. In chapter 3 of this article, a method to realize long distance

multi point gas detection has been realized.

The combination of chemical sensor heads with optical fiber sensing where a sensitive probe or dye indicator changes its characteristic (which would alter the power of the transmission signal) or color, in the presence of the gas species to be detected. Optical fiber sensors with chemical sensor head has found applications in toxic or hazardous gas species, such as hydrogens, hydrocarbons, oxygens, and nitrogen oxides. Gas sensitive chemical materials, such as tungsten trioxide (WO_3), metallic platinum (Pt), and palladium (Pd), are widely used. Chemical materials can be coated around the core of silica fiber to realize distributed sensing [67]–[71]. However, when silica fiber based gas sensing is utilized to measure long distance harsh environment, the sensor heads are easy to be broken since silica fibers are fragile. Thereby, plastic optical fibers (POFs) are coated with gas sensitive materials on plastic optical fibers (POFs) which is going to be the topic of chapter 4 in this article.

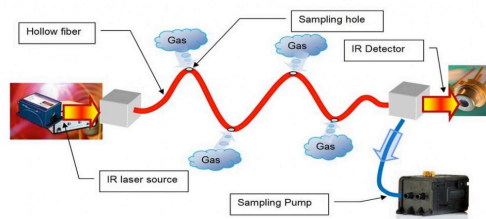


Figure 1.11 Optical fiber sensors for gas detection.

1.3 Outline of the thesis

In this dissertation, I study on quasi-distributed optical fiber sensing system that is capable of tele-monitoring the change of temperature, pressure and the occurrence of gas leakages. Firstly, I work on an improvement technique for the optical pulse correlation sensing which modulates the propagation time according to the transmission fiber expansion caused by the fiber tensile strain force. Secondly, I present on an quasi-distributed optical fiber gas sensing method based on gas spectroscopy and region selectable technique, to monitor the occurrence of gas leakage along gas pipeline. Finally, I propose a quasi-distributed plastic optical fiber (POF) gas sensing

concept using OTDR and POF with one end coated with gas sensitive material. As a result of absorption swelling, the reflective index of the chemical material will be reduced in the presence of gas, leading to the Fresnel reflection change at the POF-air interface from which one can obtain the gas information.

Chapter 2 Polarization-insensitive pulse correlation measurement for remote fiber sensing using polarization scrambled pulses

The variation of measurands, e.g. temperature, pressure, strain, etc., would cause the expansion/compression of sensing fibers which lead to the increase/decrease of the path length of optical signals that finally vary the propagation time of sensing signals. The propagation time drift containing abundant information of ambient environmental change, is a valuable parameter in optical fiber sensors. However, it is difficult to be detected by traditional electrical components as the time drift normally occurs in picosecond. One of the most effective ways to realize high precision timing control/measurement is to use pulse correlation measurement.

Optical pulse correlation sensing system utilizes the time modulation of the optical signal propagating in the optical fiber transmission line to monitor the temperature, stress or pressure around the optical fiber. It provides high accuracy (sub-picosecond), large range linear response (~ 10 ps) and high time resolution (~ 0.01 ps).

Correlation signal detection using second harmonic generation (SHG) in a suitable optical crystal are the most popular and cost-effective experimental methods. The resulting second-harmonic wave is detected by a conventional, slow optical receiver that is capable of sub-picosecond-order time resolution in temporal waveform measurement, such as a semiconductor photodiode or an Avalanche photodiode. However, the SHG conversion efficiency is strongly dependent on the polarization state of the incident light wave. Thus, if the incident polarization state is affected, e.g., by birefringence in the transmission line or optical fiber twisting, the output signal of the pulse correlation measurement is easily disturbed.

One idea to suppress the polarization fluctuation in the correlation signal is utilizing the birefringence compensation approach in a retraced fibre path using Faraday rotator mirror.

However, the technique is not suitable for multi region sensing due to the utilization of Faraday rotator mirror in every region is inconvenient, pricey, and non-immune to electro-magnetic interference (EMI).

A more practical method is proposed in this chapter, using polarization scrambled pulse train (PSP), in which the polarization state of each pulse is randomized. The principle of PSP suppressing the polarization fluctuation in correlation signals is analyzed. A PSP is generated using a GS-LD modulated by an external RF signal to work as a low-coherence pulsed light source (with the central wavelength of 1550nm, frequency of 1.5GHz), an PM optical coupler to split the incident signal into two beams and precisely adjust the polarization state and pulse propagation time of each beam. The stability of PSP-based optical pulse correlation sensing is evaluated using a PSP/PMP, an optical coupler, a half wave plate (HWP), a quarter wave plate (QWP), and a pair of SHG and APD.

Afterwards, wide region optical pulse correlation sensing is explained, including the principle of correlation sensing, the impact of polarization instability on tele-monitoring and improvements of optical pulse correlation technique using PSP light source. Experimental demonstration has been conducted on a pulse correlation sensing utilizing a PSP light source.

Chapter 3 Quasi-distributed region selectable gas sensing for long distance pipeline maintenance

Many chemical species exhibit strong absorption in the UV/visible, near infrared or mid infrared regions of the electromagnetic spectrum. The absorption lines or bands are specific to each species, forming the basis for their detection and measurement. Gas absorption spectroscopy offers direct, accurate and highly selective means of gas measurement. Optical gas sensors can realize high sensitive detection of gas concentration. Owing to the intrinsic advantages of optical fiber sensors, optical fiber gas sensors based on gas absorption spectroscopy are widely studied and applied in the gas detection, such as CH_4 , HCN , and NH_3 , etc. However, multi region detection based on gas absorption spectroscopy are barely realized.

This chapter presents a new concept, which is capable of addressing multiple gas sensors in

one single fiber using region selectable technique. Wavelength scanning LD and wavelength analyzer connect with optical fibers and region selectable reflectors to launch wavelength scanning light pulses and receive the reflected absorption spectroscopy from multi-regions.

Firstly, the concept of region selectable gas sensing using tele-spectroscopy for gas pipeline detection is explained in detail. To demonstrate the concept, gas cells are employed to simulate gas leakages along the pipeline. Along with scanning LD, FBGs and fibers, an optical fiber gas remote sensing based on gas absorption spectroscopy is constructed. The gas absorption spectrum is detected and analyzed. Moreover, some issues that are potentially to impact the performance of the technique is discussed, including absorption line broadening under varied temperatures and pressures, and the impact of FBG instability under high temperature.

To distinguish multi-regions, gas spectroscopy combines with a region selectable technique by synchronizing a fiber Bragg grating (FBG) reflector with the target absorption line in each sensing region. Spectroscopy performances under different temperatures, pressures and different leakage occurrences are measured. The possible optical loss is going to be discussed and the available sensing length of the system is estimated.

In addition, the performance of multi-region tele-monitoring gas sensing is experimentally demonstrated. Available numbers and coverage of multi-sensing regions are estimated using fiber propagation loss and the loss of sensing unit. Also, the sensing length and the maximum number of the sensing regions are estimated by taking into account of the impact of optical transmission loss.

Finally, a method to extend the number of sensing regions is presented using optical partial reflectors and the time dependent wavelength scanning scheme of the FBG sensor monitor, which causes the displayed wavelength shift in long range detection ($>1\text{km}$). The principle of displayed wavelength shift of FBG sensor monitor is explained specifically. The concept of the extension technique of the number of sensing regions is introduced and experimentally demonstrated using FBG sensor monitor, optical partial reflectors, FBGs and long fibers.

Chapter 4 Plastic optical fiber gas sensing using OTDR

Optical chemical sensors are growing quickly over the last few decades driven by such factors as low cost, miniature optoelectronic light sources and detectors. Fiber-optics chemical sensors (FOCS) make particular interrogation methods, e.g., evanescent wave spectroscopy and spatially resolved lifetime spectroscopy, become practical.

A concept for a quasi-distributed gas detection method by plastic optical fiber with one end coated with gas sensitive chemical material, OTDR, silica fibers, and optical couplers is proposed in this chapter. The refractive index of the gas material is reduced in the presence of hydrocarbon gases owing to gas-absorption swelling, leading to the propagation light field change which can be used to estimate the occurrence of the gas. Combing with OTDR technique, the location of the gas can be distinguished.

The concept of the GI-POF gas sensing by OTDR and the principle of Fresnel reflection power variation caused by the refractive index change of the chemical material in the presence of a specific gas is explained. As a pre-demonstration, ethyl alcohol is used as a substitute of gas, the difference of Fresnel reflection power at the POF-air interface, POF-alcohol interface, and POF-water interface are measured and analyzed.

Chapter 5 Summary

A conclusion and discussion is presented in Chapter 5. The whole study is going to be summarized. A future research plan is presented.

Chapter 2

Polarization-insensitive Pulse Correlation Measurement for Remote Fiber Sensing Using Polarization Scrambled Pulses

In order to reduce polarization impairment in remote fiber sensing, a polarization-insensitive pulse correlation measurement technique using polarization scrambled pulse train (PSP), in which the polarization state of each pulse is randomized, was proposed. The principle of the stabilization technique was explained and experimental generation of PSP was verified. Moreover, the fiber strain measurement using PSP-based pulse correlation tele-monitoring under various polarization states on a multi-region fiber sensing system was implemented. The results show good stability against polarization fluctuation, indicating that the technique has great potential for use in harsh environment tele-monitoring.

2.1 Introduction

The time-of-flight (TOF) of light pulse has been applied to direct distance measurement over 50 years [72]. By converting the distance variation into time change and precisely timing control, the technique has been widely used in diagnostic and therapeutic medicine [73], [74], 3D distance measurements [75], complete range cameras [76], [77], and depth sensors [78], etc. The TOF distance measurement has achieved nanometer measurement precision by timing femtosecond pulses through phase-locking control of the pulse repetition rate using the optical cross-correlation technique [79].

In optical fiber sensors, prolonged fiber length caused by the change of measurands, e.g. temperature, strain, etc, can be detected by the propagation time change of optical pulses.

Pulse correlation measurement is an effective way for high precision timing control [41], [80], examples include the electron/electronic performance monitoring using high time resolution pulses [81], [82], precise timing stabilization of light pulse over long distance [83], and time jitter detection between two laser pulses [84], etc. Sub-picosecond, even femtosecond timing control were obtained in the stabilization or synchronization of laser pulses by optical pulse correlation measurement.

When applying pulse correlation measurement in optical fiber sensing systems that monitor the ambient conditions around the optical fiber by fiber length extension, a high accurate, anti-EMI, real-time sensing system with large range linear responsibility was realized [42]–[46].

The principle, development, as well as the long term instabilities of fiber sensing using optical pulse correlation measurement have been illustrated in this chapter. The polarization fluctuation of optical pulse correlation measurement is discussed. A method to solve the polarization fluctuation in optical pulse correlation measurement is proposed and experimentally demonstrated.

2.1.1 Optical fiber sensing based on pulse correlation measurement

When working with optical short pulses, we can not directly measure their temporal waveform using a conventional electrical receiver. The most widely used technique for measuring them

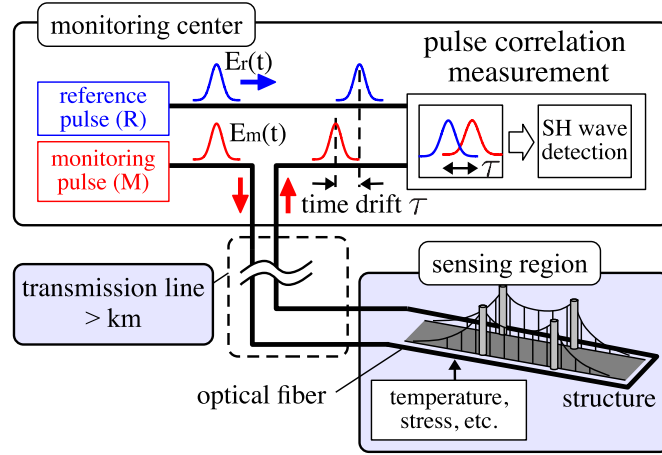


Figure 2.1 Fiber sensing based on pulse correlation measurement.

is to use pulse correlation measurement, in which the short optical pulse is used to measure itself. Correlation techniques using second harmonic generation (SHG) in a suitable optical crystal are the most popular and cost-effective experimental methods, as shown in Fig 2.1. The resulting second-harmonic wave is detected by a conventional, slow optical receiver, such as a semiconductor photodiode or an Avalanche photodiode (APD). The combination of SHG and APD, called a nonlinear optical receiver in this paper, has been shown to be capable of sub-picosecond-order time resolution in temporal waveform measurement. In this study, we use pulse correlation measurement for observing the sub-picosecond time drift variation between two optical pulse trains.

In optical pulse correlation measurement, a reference pulse train $E_r(t)$ is guided to correlate with a monitoring pulse train $E_m(t)$ which is an actual replica of the reference pulse train with a time delay τ caused by the optical path extension in sensing region. As shown in Fig. ??, the area of the overlapped section of $E_r(t)$ and $E_m(t)$, depends on τ , i.e., τ can be indicated by the area of the correlation section of $E_r(t)$ and $E_m(t)$ that can be accurately measured through a nonlinear crystal, e.g., Second Harmonic nonlinear crystal with spatially modulating nonlinear property realizing Second Harmonic Generation (SHG).

2.1.2 Problem of Optical fiber sensing based on pulse correlation measurement

Despite the multiple advantages of optical fiber sensing based on pulse correlation, when using SHG for pulse correlation measurement, the problem is that the SHG conversion efficiency is strongly dependent on the polarization state of the incident light wave. Thus, if the incident polarization state is affected, e.g., by birefringence in the transmission line or optical fiber twisting, the output signal of the pulse correlation measurement is easily disturbed, leading to the system sensitivity reduction and linear range compression. To stabilize the SHG pulse correlation measurement against the polarization fluctuation, we propose the use of a pulse scrambled pulse train (PSP), in which the polarization state of each pulse is randomly scrambled.

2.2 Pulse correlation measurement using collinear SHG process

If the intensity profile of two independent short pulses, the reference and the monitoring pulses, are represented by $I_r(t)$ and $I_m(t)$ with the peak at $t = 0$, respectively,

$$I_r(t) = |E_r(t)|^2, I_m(t) = |E_m(t)|^2 \quad (2.1)$$

The pulse correlation function can be written as

$$G_2(\tau) \equiv \int_{-\infty}^{\infty} I_r(t)I_m(t - \tau)dt, \quad (2.2)$$

here τ is the time difference between the reference and monitoring pulses. If the two fields have the same gaussian waveform with the FWHM (full width at half maximum) pulse width Δt , their intensity distribution is given by

$$I_r(t) = I_m(t) = \frac{1}{\sqrt{2\pi}\Delta t} \exp\left(-\frac{t^2}{2\Delta t^2}\right) = I(t), \quad (2.3)$$

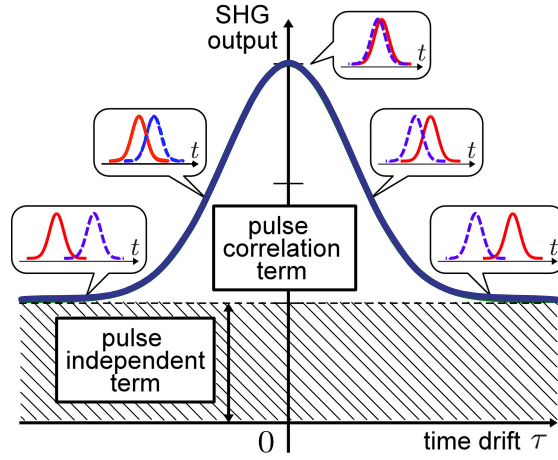


Figure 2.2 SHG output with respect to time drift τ between two pulses. Inset figures show the time-position relationship between the reference pulse (the red solid line) and the monitoring pulse (the blue dashed line). The shaded and the remaining regions correspond to the pulse independent term $G_2(0)$ and the pulse correlation term $G_2(\tau)$ in the SHG output, respectively.

Thus, Eq. (2.2) is calculated as

$$\begin{aligned}
 G_2(\tau) &= \int_{-\infty}^{\infty} I(t)I(t - \tau)dt \\
 &= \frac{\bar{I}^2}{\sqrt{2\pi}\Delta t} \exp\left(-\frac{\tau^2}{2\Delta t^2}\right),
 \end{aligned} \tag{2.4}$$

where \bar{I} is the energy of one pulse. From Eq. (2.4), we can determine the small variation $\Delta\tau$ in the time drift τ from the pre-measured values \bar{I} and Δt .

When using SHG in a collinear geometry to obtain the pulse correlation function, the SHG output recorded by a slow detector includes not only the pulse correlation term but also the τ -independent constant term, as shown below. We assume the electric fields of the reference and monitoring pulse train have the same repetition period T and the same intensity profile $I(t)$. The SHG output power P_{SHG} is given by

$$\begin{aligned}
 P_{SHG}(\tau) &\propto \left\langle \left| \{E_r(t) + E_m(t - \tau)\}^2 \right|^2 \right\rangle \\
 &\propto \langle I(t)^2 + I(t - \tau)^2 + 4I(t)I(t - \tau) + s(t, \tau) \rangle \\
 &\propto G_2(0) + 2G_2(\tau),
 \end{aligned} \tag{2.5}$$

here $|E_r(t)|^2 = I_r(t)$, $|E_m(t)|^2 = I_m(t)$, $s(t, \tau)$ is the oscillation term with the phase term $\arg[E_r(t)E_m(t - \tau)^*]$ induced by the optical interference and $\langle \cdot \rangle$ shows the time averaging in the slow optical receiver. The fast oscillation terms $s(t, \tau)$ can be averaged out to zero over a sufficient long time if the independent two electric fields $E_r(t)$ and $E_m(t)$ have uncorrelated phase terms.

Equation (2.5) shows the pulse correlation term sitting on top of a background with a peak to background ratio of 3:1 (see Fig. 2.2). The SHG output is maximized when the two optical pulses overlap and minimized when the two pulses are completely separated. The SHG output corresponding to the first term on the right-hand side of Eq. (2.5), $G_2(0) \propto \langle I(t)^2 \rangle = \langle I(t - \tau)^2 \rangle$, gives the averaged intensity independent of the time drift τ . This term is called as a pulse independent term of the SHG output in this paper. The SHG output corresponding to the second term on the right-hand side of Eq. (2.5) gives the required pulse correlation term $G_2(\tau) \propto \langle I(t)I(t - \tau) \rangle$. If the pulse independent term $G_2(0)$ can be eliminated from the SHG output, we can obtain the pulse correlation term $G_2(\tau)$.

In order to eliminate the pulse independent term $G_2(0)$ and obtain the pulse correlation term $G_2(\tau)$, differential measurement is employed by splitting the light signal into two identical signals and propagating in two different channels. One signal works as reference pulse, and the other works as monitoring pulse traveling through the monitoring region. At each channel, the signal is going to be measured by a pair of SHG and APD. In the end, the differential power of the reference pulse and monitoring pulse detected.

2.3 Polarization fluctuation of pulse correlation term and its suppression

2.3.1 Polarization-induced fluctuation of pulse correlation term in SHG output

The time-dependent polarization fluctuation in transmission line can be modeled by the special Unitary matrix as follows:

$$\hat{U}_i(t) = \begin{pmatrix} \alpha_i(t) & \beta_i(t) \\ -\beta_i(t)^* & \alpha_i(t)^* \end{pmatrix} \quad (i = r, m), \quad (2.6)$$

where $\alpha_i(t)$ and $\beta_i(t)$ are complex values satisfying $|\alpha_i(t)|^2 + |\beta_i(t)|^2 = 1$, and $i = r, m$ show the polarization fluctuation for the reference (r) and the monitoring (m) pulse train, respectively. In what follows, we assume that the polarization fluctuation is slow and has a longer correlation time than the averaging time of the optical detector. Under this condition, the complex values α_i and β_i can be treated as constant values.

When the horizontal and the vertical components, $E_{iH}(t)$ and $E_{iV}(t)$ ($i = r, m$), have the same intensity profile $I(t)$, we can define the electric field vector $\vec{E}_i(t)$ ($i = r, m$) of the pulse train as

$$\vec{E}_i(t) = \begin{pmatrix} E_{iV}(t) \\ E_{iH}(t) \end{pmatrix} = \sqrt{I(t)} e^{j\bar{\omega}t} \frac{1}{\sqrt{2}} \begin{pmatrix} e^{j\phi_i(t)} \\ e^{j\psi_i(t)} \end{pmatrix}, \quad (2.7)$$

where $\bar{\omega}$ is the central angular frequency and $\phi_i(t)$ and $\psi_i(t)$ show the time-dependent phase terms of the horizontal and the vertical components of the electric field vector, respectively.

For simplicity, the optical axis of the SHG crystal is assumed to be fixed in a vertical direction. Under the polarization fluctuation represented by Eq. (2.6), the intensity $I_i(t)$ of the reference and the monitoring pulse train along the optical axis of the SHG crystal is given by

$$\begin{aligned}
 I_i(t) &= |\alpha_i E_{iV}(t) + \beta_i E_{iH}(t)|^2 \\
 &= \frac{1}{2} I(t) \{1 + f_i(t)\},
 \end{aligned} \tag{2.8}$$

with

$$f_i(t) = 2 |\alpha_i \beta_i| \cos [\phi_i(t) - \psi_i(t) + \arg(\alpha_i \beta_i^*)], \tag{2.9}$$

where $i = r, m$ and $f_i(t)$ shows the intensity fluctuation due to the change in polarization. Assuming that the phase difference $(\phi_i - \psi_i)$ is almost constant within a single optical pulse, the pulse correlation term in the SHG output is calculated as

$$\begin{aligned}
 G_2(\tau) &\propto \langle I_r(t) I_m(t - \tau) \rangle \\
 &= \frac{1}{4} \langle I(t) I(t - \tau) \rangle_T \\
 &\quad \times \langle \{1 + f_r(t)\} \{1 + f_m(t - \tau)\} \rangle_{\text{pulse}},
 \end{aligned} \tag{2.10}$$

where the first bracket $\langle \cdot \rangle_T$ shows the time averaged over the pulse repetition period T and the second one $\langle \cdot \rangle_{\text{pulse}}$ shows the averaging over the number of pulses included in the response time of the detector. In the case of conventional optical pulses, the pulse averaging term including $f_i(t)$ in Eq. (2.10) is strongly dependent on the polarization fluctuation represented by α_i and β_i since the phase difference $(\phi_i - \psi_i)$ is fixed at the constant value in all pulses.

Fig 2.3 shows the differential signal change under polarization fluctuation, the sensitivity of the signal is reduced and the linear range is narrowed down.

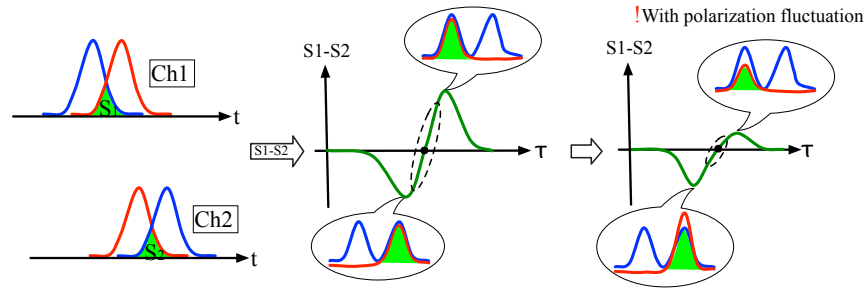


Figure 2.3 Polarization fluctuation caused SHG signal degradation.

2.3.2 Suppression of the polarization fluctuation in the pulses correlation measurement

Suppression of polarization fluctuation of the correlation signal in optical pulse correlation sensing by Faraday rotator mirror and polarization scrambled pulse train (PSP) are discussed in this section.

Faraday rotator Mirror

The polarization fluctuation in correlation signals can be suppressed utilizing the birefringence compensation approach in a retraced fibre path using Faraday rotator mirror, as shown in Fig 2.4.

When the signal passes through the monitoring fiber in the forward direction, some birefringence fluctuation will occur due to birefringence or fiber twisting. After passing through the Faraday rotator mirror twice, the optical polarization state of the optical signal has been rotated 90° . Then some birefringence fluctuations will be exerted on the optical signal when it transmits the sensing region again in the backward direction, which will compensate the birefringence fluctuation in the forward direction.

Using Faraday rotator mirror can effectively improve the polarization stability of pulse correlation sensing, however, the technique is not suitable for multi region sensing due to the utilization of Faraday rotator mirror in every region is inconvenient, pricey, and non-immune to electro-magnetic interference (EMI).

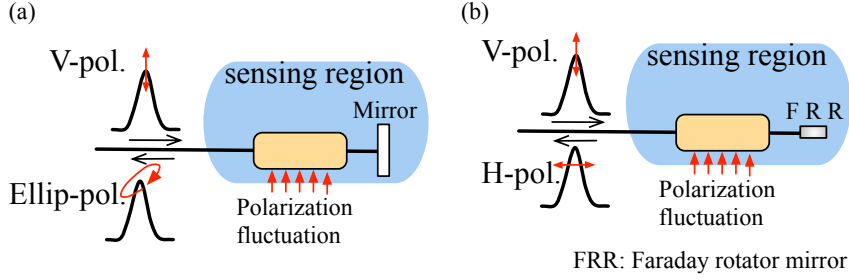


Figure 2.4 Polarization fluctuation suppression Faraday rotator

Polarization scrambled pulse train

Assuming the two phase terms of Eq. 2.10, $\phi_i(t)$ and $\psi_i(t)$, have a correlation time that is much shorter than the response time of the detector and the pulse repetition period. In this case, each pulse has a certain polarization state, while the polarization state of each pulse is randomly changed and there is no correlation between the polarization states in each pulse. We call this pulse train a PSP. When using the PSP, the fluctuation term $\langle f_i(t) \rangle_{\text{pulse}}$ ($i = r, m$) in Eq. (2.10) becomes zero by the pulse averaging. Moreover, if the reference and the monitoring pulses are independent, i.e., $\langle e^{i(\phi_i - \psi_j)} \rangle_{\text{pulse}} = 0$ ($i \neq j$), the fluctuation term $\langle f_r(t) f_m(t - \tau) \rangle_{\text{pulse}}$ in Eq. (2.10) also becomes zero. Thus, the pulse correlation term becomes

$$\langle I_r(t) I_m(t - \tau) \rangle = \frac{1}{4} \langle I(t) I(t - \tau) \rangle_T. \quad (2.11)$$

This is a constant value even under the polarization fluctuation represented by α_i and β_i . Consequently, we can stabilize the pulse correlation measurement with SHG process by using the PSP as shown in Fig 2.5.

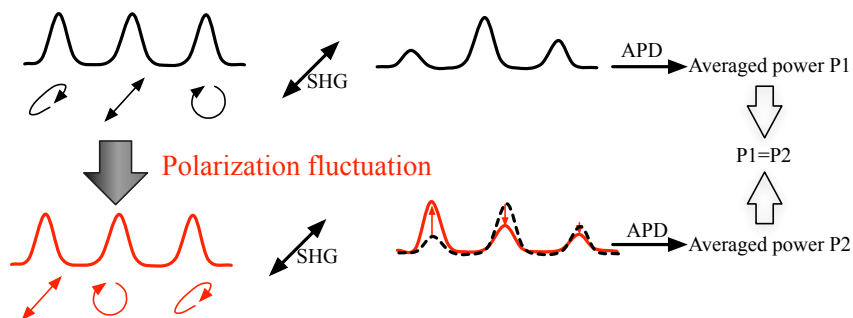


Figure 2.5 Polarization fluctuation suppression polarization scrambled pulse train (PSP). The pulses in black color are the ones did not experience polarization fluctuation, the pulses in red color are the ones experienced polarization fluctuation.

2.3.3 Experimental generation of PSP and stabilization of pulse correlation measurement

Let us consider the conventional optical pulses, which we call a polarization maintained pulse train (PMP), with 45° linear polarization [see Fig. 2.6(a)]. If the horizontal components of the PMP are delayed with the time period greater than the coherence time T_c , the phase difference between the vertical and the horizontal components of the electric field has a correlation time that is much shorter than the average time of the slow detector. Moreover, when the delay time is set to be the integral multiple of the repetition period T , the resultant pulse train has the same intensity waveform as the PMP but the polarization state in each pulse is randomized [Fig. 2.6(b)].

The setup to generate the PSP is shown in Fig. 2.6(c). We used a GS-LD modulated by an external RF signal as a low-coherence pulsed light source. The central wavelength is 1550nm, the repetition frequency is 1.5GHz, and the pulse width is 10ps. First, the incident PMP is split into two components with the same intensity and the same vertical polarization state by the polarization-maintained coupler. Next, the polarization state of one component is changed to horizontal by a horizontal polarizer, and the other component is delayed with a time period larger than the coherence time T_c and equal to the integral multiple of the repetition period T . Finally, two components are recombined at the coupler and the resultant pulse train becomes

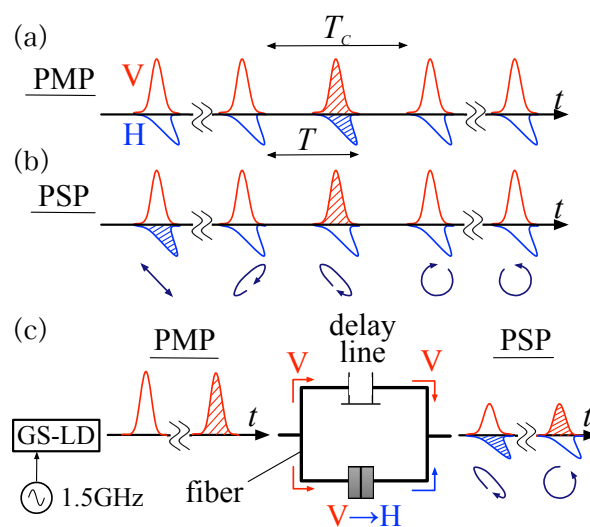


Figure 2.6 (a) PMP with 45° linear polarization. V and H show the vertical and the horizontal polarization, respectively, and T_c is the coherence time of optical pulses. (b) PSP. The dark blue rotating arrows below each pulse show the polarization state. (c) Setup to generate the PSP from the PMP. The temporal delay in the delay line is set to be larger than the coherence time T_c and be integral multiple of the repetition period T .

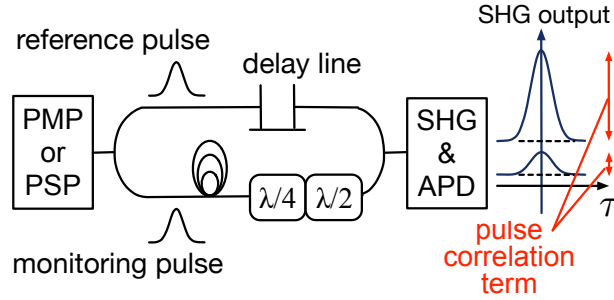


Figure 2.7 Experimental setup of the SHG pulse correlation measurement using the PMP or the PSP under polarization fluctuation.

the PSP.

We performed the SHG pulse correlation measurement through a polarization changing media. The experimental setup is shown in Fig. 2.7. The incident pulse train (PMP or PSP) is divided by a 50% coupler, one of which corresponds to the reference pulse train and the other to the monitoring pulse train. The monitoring pulse train is sent through a transmission fiber longer than the coherence length of the pulse train. Thus, the two pulse trains can be treated as independent. The polarization fluctuation is induced by changing the angle of the half wave plate (HWP) and the quarter wave plate (QWP). The experimental results are shown in Fig. 2.8. The vertical axis corresponds to the pulse correlation term in the SHG output when $\tau = 0$. In the case of PMP, there is a large fluctuation of the pulse correlation term, as shown in Fig. 2.8(a). In contrast, by using the PSP, the fluctuation can be drastically suppressed, as shown in Fig. 2.8(b).

We can estimate the stability of the pulse correlation term in the SHG output under the polarization fluctuation by using R value defined with

$$R \equiv \frac{\text{Max} - \text{Min}}{\text{Max} + \text{Min}}, \quad (2.12)$$

where Max and Min show the maximum and minimum value of the pulse correlation term under the polarization fluctuation. $R = 1$ means that the pulse correlation term of the SHG output is strongly dependent on the incident polarization state and is unstable under the polar-

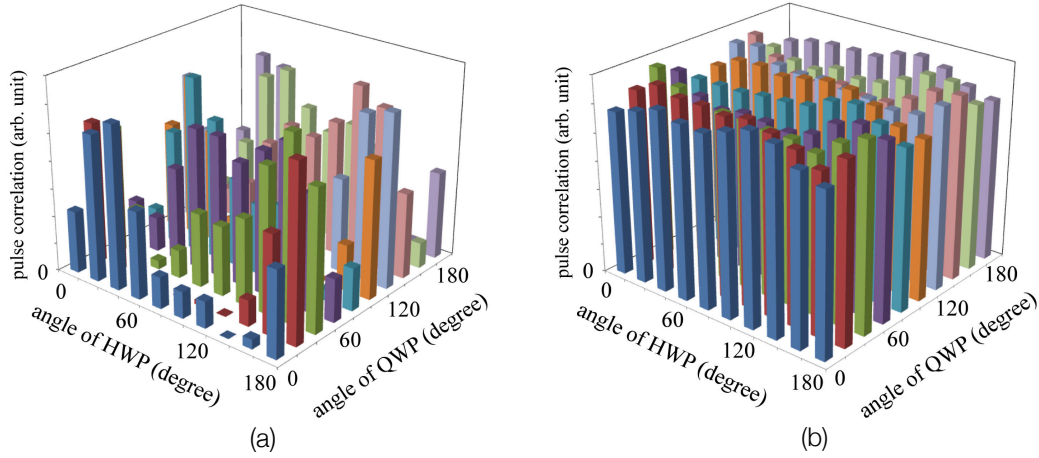


Figure 2.8 Comparison of the pulse correlation terms in the SHG output at $\tau = 0$ induced by (a) the PMP and (b) the PSP during the variation of polarization state.

ization fluctuation, while $R = 0$ means that it is stable even under the polarization fluctuation. In the case of PMP, R value is almost 1, while in the case of PSP, the R value becomes less than 0.1 in this experiment.

2.4 PSP-Based Wide-Region Optical Pulse Correlation Sensing

2.4.1 Principle of pulse correlation measurement for fiber strain/temperature sensing

The schematic of conventional wide region optical pulse correlation sensing is shown in Fig 2.9. Conventional optical pulse train (PMP), is split into reference pulse train and monitoring pulse train which transmits in the optical sensing fiber. When measurands such as strain or temperature are varied, optical sensing region would transduce the variation of the measurand as additional time drift between the monitoring pulse and the reference pulse. From this sub-picosecond order time difference, the variation of measurand can be demodulated by correlation

sensing unit (CSU).

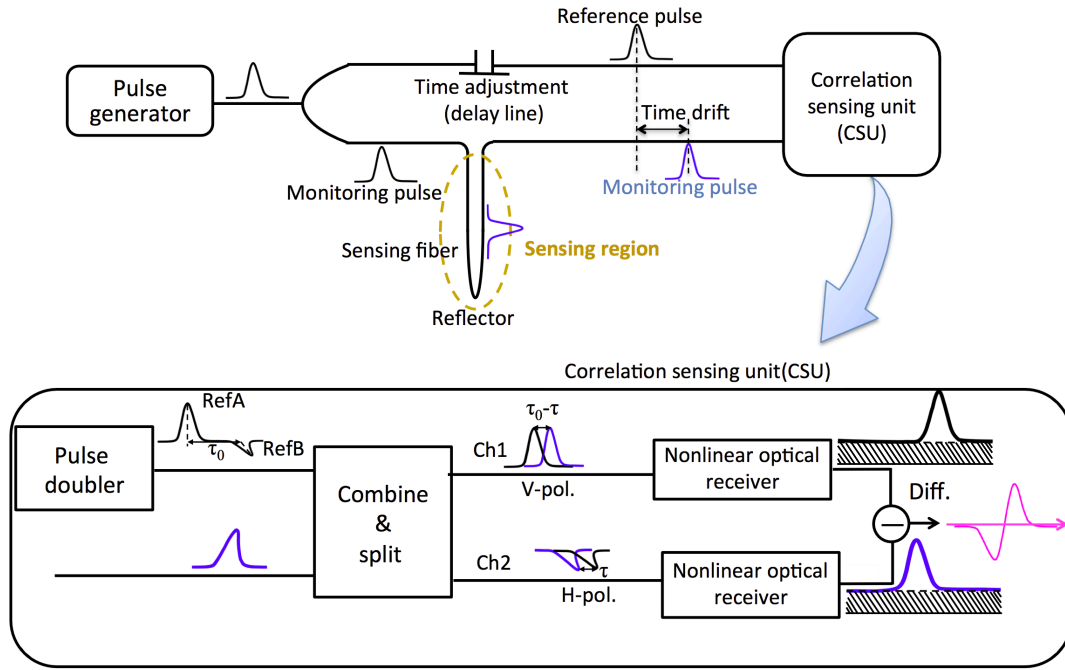


Figure 2.9 Schematic of optical pulse correlation sensing technique.

Correlation sensing unit is comprised of a pulse doubler, an optical pulse combine and split unit and a pair of orthogonally polarized nonlinear optical receiver (Vertical-polarization PPLN SHG and APD, Horizontal-polarization SHG and APD) as shown in inset of Fig 2.9. The pulse doubler is connected to the reference arm. The reference pulse is split into a vertical polarization component (RefA) and a horizontal polarization component (RefB) with a fixed time difference τ_0 . The two reference pulses are combined with monitoring pulses, which are supposed to be polarized at 45° , in the optical pulse combine and split unit. The resulting combination of reference pulses and monitoring pulse are then split into two groups and guided into two separate channels. The combination of backward reference RefA with monitoring pulses have time drift value of $\tau_0 - \tau$, transmitting in one channel. The forward reference RefB with monitoring pulses have a time drift value of τ , transmitting in the other channel.

In each channel, the combined pulses are guided into a SHG crystal to create a second

harmonic wave, of which the averaged intensity is detected by APD within its response time. The averaged intensity of the second harmonic wave approaches maximum value when the two input pulses completely overlap each other, i.e., $\tau_0 - \tau = 0$ or $\tau = 0$. Using this technique, differential signal of the two channels is detected to obtain wide range linear response between signal intensity and time position drift. Each nonlinear optical signal contains both pulse correlation term and pulse independent term, as shown in Fig 2.2. Fortunately, pulse independent terms would be canceled out by the differential process.

2.4.2 Impact of polarization instability on tele-monitoring and improvements of optical pulse correlation technique using PSP light source

The optical pulse correlation sensing system described in the previous section can realize wide-region environment tele-monitoring by applying the multi-region selectable technique using partial reflectors [45]–[47]. Unfortunately, polarization management over long distance and multi-region fiber lines is difficult. Thus, in the CSU, the signal splitting ratio between Ch1 and Ch2 can be easily changed when the polarization states of monitoring pulses are varied, as shown in Fig 2.10. The blue line in Fig 2.10(b) is the result of horizontal-polarization input, and the red line is the result of vertical-polarization input, respectively. The waveforms of differential signals are dramatically changed due to their polarization.

Figure 2.11(a) shows the schematic of PSP-based pulse correlation sensing. The states of polarization of the pulses on PSP are scrambled as described in section 2.3.1. Because of polarization scrambling, averaged signal intensities of Ch1 and Ch2 are stable even when the polarization states fluctuate. Consequently, the polarization fluctuation at the twisting of fibers or fiber links would not impact on the output SHG signal. In addition, the averaged differential signal of two channels will have stable waveform, regardless of the polarization changing on transmission lines, as shown in Fig 2.11(b).

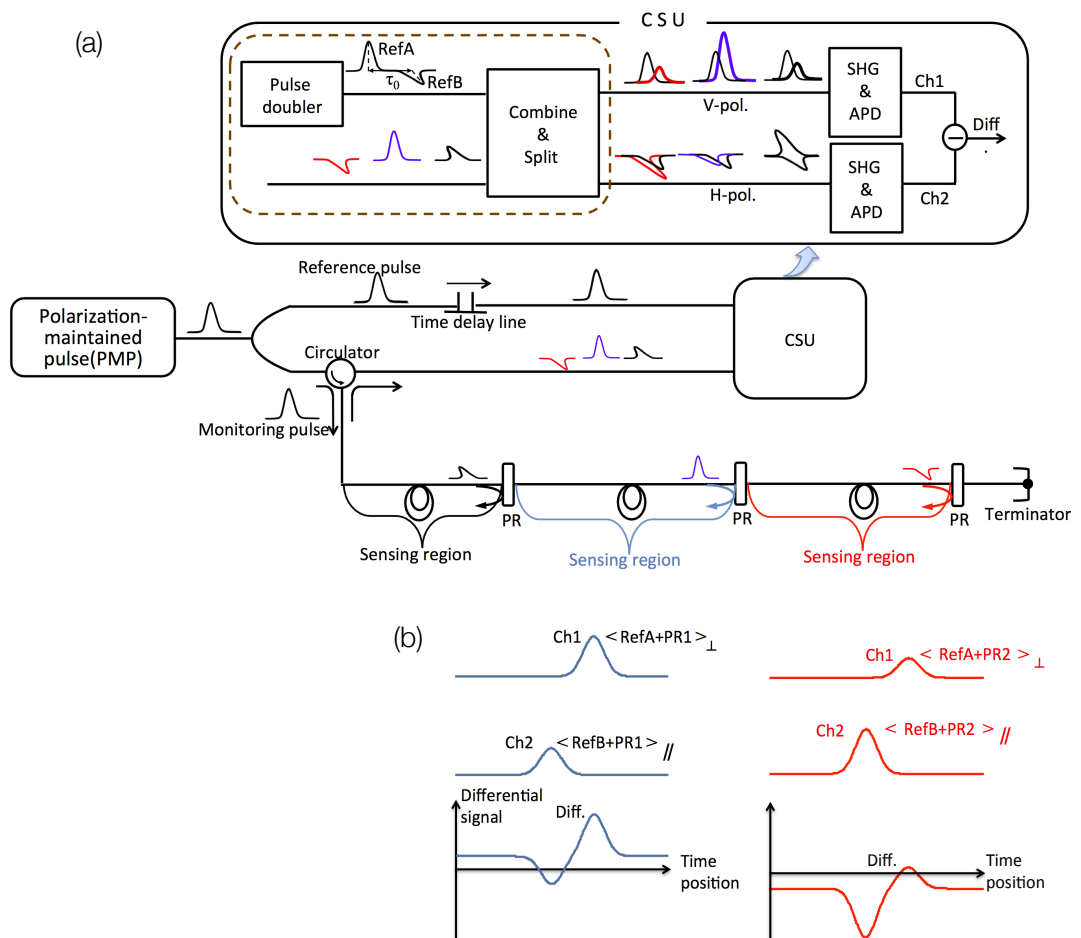


Figure 2.10 (a) Schematic of PMP-based multi-region's optical pulse correlation sensing. (b) Different polarization impacts on signals at two regions.

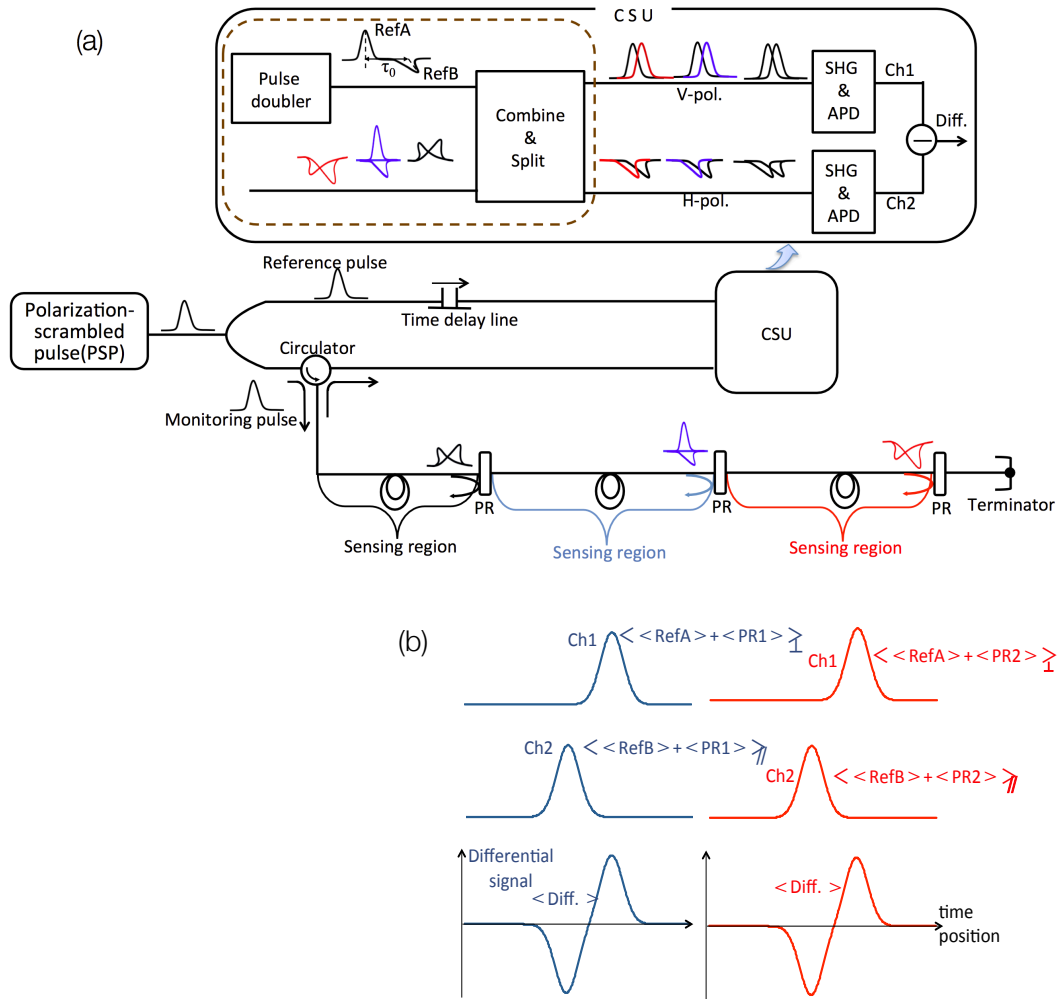


Figure 2.11 (a) Schematic of PSP-based wide region optical pulse correlation sensing. (b) Stabilized signals of different regions.

2.5 Experimental Results of Correlation Measurement under Various Polarization Conditions

2.5.1 Sensitivity stabilization against polarization instability

An experimental setup to investigate polarization impact on the PMP- and PSP-based optical pulse correlation multi-region sensing was constructed as shown in Fig 2.12. An optical pulse correlation two-region sensing system was constructed by connecting two partial reflectors at the end of each region. A pair of wave plates, a half wave plate and a quarter wave plate, worked as polarization change medium in the first region of the transmission line. Meanwhile, the time position measurement in the second sensing region is to demonstrate tensile-strain measurement on the fiber.

First of all, polarization impact of the fiber twisting situation in first region was imitated by rotating the quarter wave plate and half wave plate separately. Under each state of polarization, the differential signal was measured and recorded by scanning the time position of reference pulse which is used to measure the correlation signal versus monitoring pulse time position, as shown in the inset of Fig 2.12. Our tunable optical time delay line has a time resolution of 0.005 ps and a scanning range of 0-330 ps. The differential signals labeled PR1 and PR2 are responses from sensing region 1 and sensing region 1 plus sensing region 2, respectively. The gradient of the linear areas of the differential signal, which are highlighted by red ellipses, indicates the sensitivity of this measurement. Importantly, the time difference between PR1 and PR2 responses (as shown in the inset of Fig 2.12) explains pure impact from selected region 2.

As the first step, the responses of PMP-based optical pulse correlation sensing is measured, in which a conventional pulse is used as the PMP light source. Differential signals and their sensitivities under typical polarization states were estimated. Subsequently, the system sensitivities using PSP were estimated. Experimental results are shown in Figs 2.13 and 2.14. The data in Fig 2.13 was gathered under different polarization conditions, in which the half wave plate and the quarter wave plate were set at $(\lambda/2, \lambda/4) = (150^\circ, 180^\circ)$ and $(\lambda/2, \lambda/4) = (60^\circ, 90^\circ)$, re-

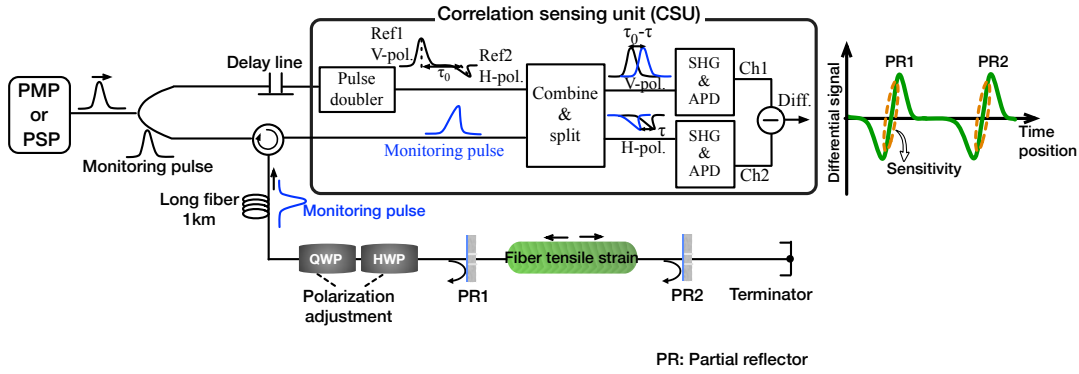


Figure 2.12 Experimental setup of demonstration of PMP and PSP-based optical pulse correlation sensing. Region 1 was demonstrated as polarization fluctuation on transmission line. Region 2 was used as strain sensing region.

spectively. The data in Fig 2.14 was obtained when half wave plate and quarter wave plate were changed from 0 to 180° in steps of 30°. As shown in Figs 2.13(a) and 2.14(a), the differential signals and sensitivities of PMP-based optical pulse correlation sensing were extremely unstable. In the case of PMP, the signal slope and sensitivity fluctuated dramatically between 0 and 1.1 mV/ps, with a fluctuation of 89.4%. Moreover, the responses from sensing region 1 and sensing region 2 had different sensitivities. However, the PSP based optical pulse correlation sensing could be stabilized at around 0.55 mV/ps at any polarization condition, as shown in Figs 2.13(b) and 2.14(b). The results of PSP-based optical correlation sensing technique had good consistency during the variation of polarization. However, they had a small fluctuation within R= 4.5% since the PSP had a power fluctuation.

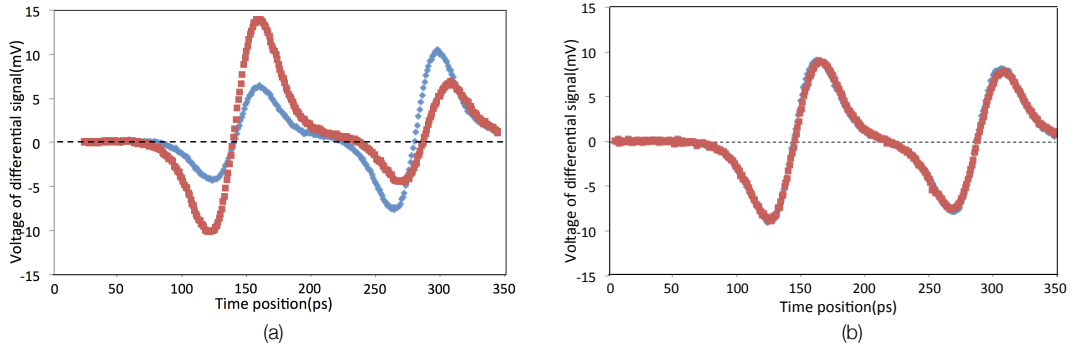


Figure 2.13 Comparison of differential signal of optical pulse correlation sensing based on PMP and PSP during the variation of polarization state. (a) Results of PMP based correlation. (b) Results of PSP based correlation. Blue and red lines were obtained when wave plates were adjusted at $(\lambda/2, \lambda/4)=(150^\circ, 180^\circ)$ and $(\lambda/2, \lambda/4)=(60^\circ, 90^\circ)$, respectively.

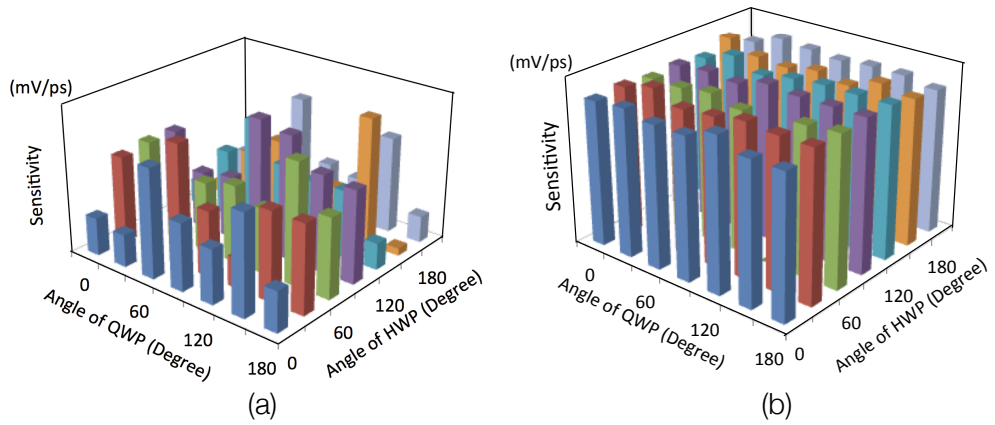


Figure 2.14 Comparison of system sensitivities of optical pulse correlation sensing based on (a) PMP and (b) PSP during the variation of polarization state.

2.5.2 Strain measurement using PSP-based sensing for tele-monitoring

After ensuring the improvement in sensing stability versus polarization drift using PSP based measurement, the region selected strain measurement of PSP-based pulse correlation sensing technique was demonstrated. As shown in Fig 2.12, the polarization state of the monitoring pulse was changed in sensing region 1. Tensile strain was applied to a single mode optical fiber using a mechanical stretcher in sensing region 2. The pulse correlation signal against tensile strain at both short sensing distance (0.2 m) and tele-monitoring (1 km) was measured. Figure 2.15(a) shows the relationship between the pulse correlation signal and the time position. The time difference between zero-cross points of the differential signal explains the optical length of sensing region 2 and its variation can be used to measure the impact of strain change. Figure 2.15 shows the pulse correlation signals against tensile strain, with a 0.2m-long transmission line [Fig 2.15(b)] and a 1km-long transmission line [Fig 2.15(c)]. The diamond, square and triangle dots in Fig 2.15(b) were measured under the angle of half wave plate and quarter wave plate of $(\lambda/2, \lambda/4) = (0^\circ, 0^\circ)$, $(\lambda/2, \lambda/4) = (0^\circ, 45^\circ)$, and $(\lambda/2, \lambda/4) = (0^\circ, 90^\circ)$, respectively. In Fig 2.15(c) the blue and red dots were detected under the angle of wave plates of $(\lambda/2, \lambda/4) = (0^\circ, 45^\circ)$ and $(\lambda/2, \lambda/4) = (0^\circ, 0^\circ)$, respectively. As shown in Figs 2.15(b) and 2.15(c), the time difference change of the differential signal and the strain applied to the fiber has good linear relationship at any polarization change and length of transmission line. The fluctuation in the results is less than 1%. Additionally, with polarization deviation, the experimental results show great consistency meaning that polarization deviation did not affect the sensitivity of this PSP based optical pulse correlation sensing technique.

Polarization instability is usually accentuated by long transmission fiber lines. Thus, this technique is useful in tele-monitoring.

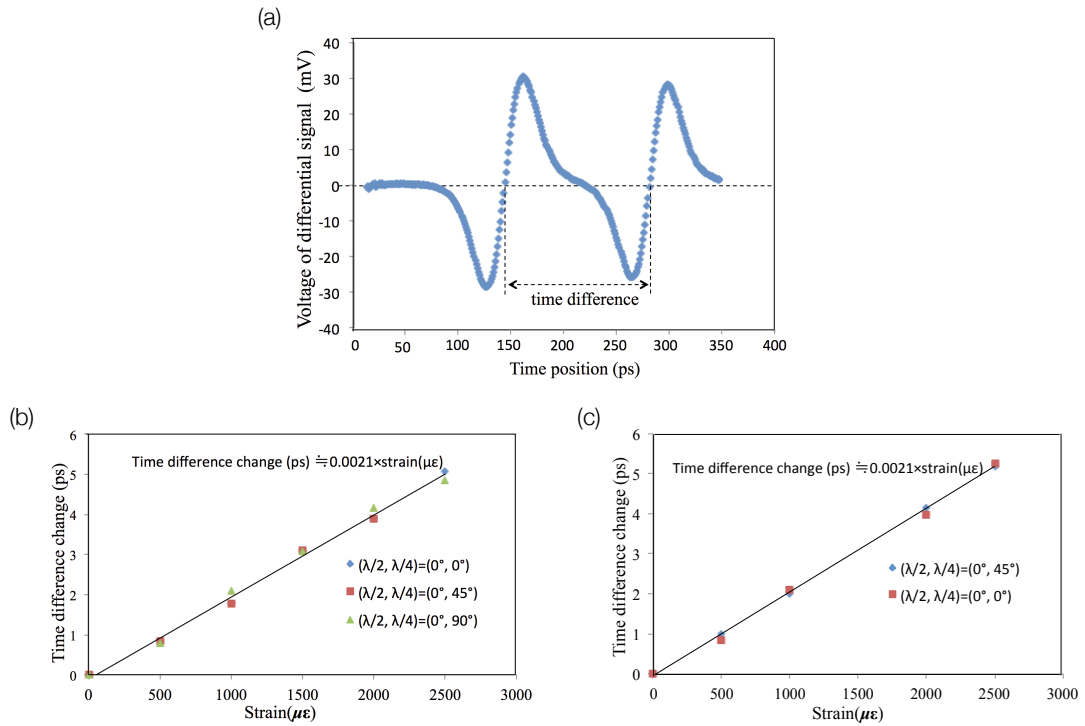


Figure 2.15 Results of strain measurement of PSP based optical pulse correlation sensing. (a) Illustration of time difference, (b) Time difference change versus strain demonstration at short distance (0.2 m). (c) Experimental results of strain demonstration of remote monitoring (1 km).

2.6 Discussion

The maximum sensing length of an optical fiber system is limited by the fiber input power which is restricted by fiber nonlinearity, the propagation loss, the pulse broadening caused by fiber chromatic dispersion and polarization dispersion. The influence of the multiple effects is discussed in the following section, as well as the crosstalk of multi-reflection in each region. In the end, an analysis is given on the sensing length and number of sensing regions of the multi-region optical pulse correlation sensing.

The system configuration of the multi-region optical pulse correlation sensing is shown in Fig 2.16. Fig 2.16(a) shows the physical configuration of sensing region where is assumed each region to have equal coverage length L . P_{in} is the input power for fiber sensing region, P_{out} is

the reflected optical power, PR_n are n th partial reflectors, N is the number of sensing regions, R is the reflectance of partial reflectors. Figure 2.16(b) shows input/output sensing pulses with the repetition of T_p .

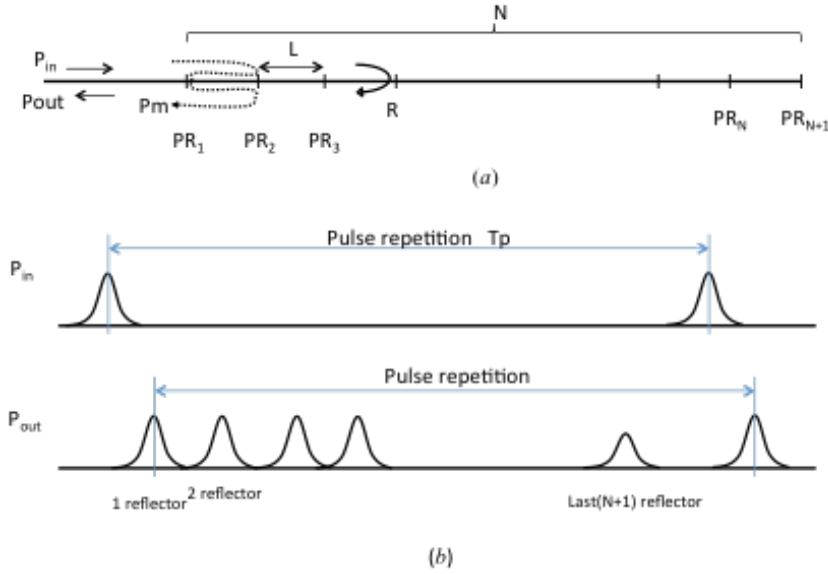


Figure 2.16 Schematic configuration of multi-region optical pulse correlation sensing.

2.6.1 Propagation loss

As a result of fiber loss, the power of an optical wave propagating in optical fibers decreases exponentially as $e^{-\alpha l}$ for a fiber of length L , as expressed by Eq. 2.13

$$P_{out} = P_{in} R (1 - R)^{2N} e^{-2\alpha Nl}, \quad (2.13)$$

where α is the fiber loss factor. It approaches the smallest attenuation value of 0.2dB/km in the spectral region near 1550nm.

The output power P_{out} dependence on the number of regions is calculated as the following equation

$$10\log\frac{P_{out}}{P_{in}} = 2N10\log(1 - R) - \alpha_{dB}L + 10\log R, \quad (2.14)$$

where α_{dB} is the fiber loss factor in decibel. Eq. eq:output dependence indicates that the output power P_{out} gradually decreases with the number of sensing regions. Besides, there are interference pulses by the reflection at partial reflectors. The largest interference pulse power P_m is estimated from the reflection of the second reflector.

$$P_m = P_{in}(1 - R)^2 R^3 e^{-4\alpha L}, \quad (2.15)$$

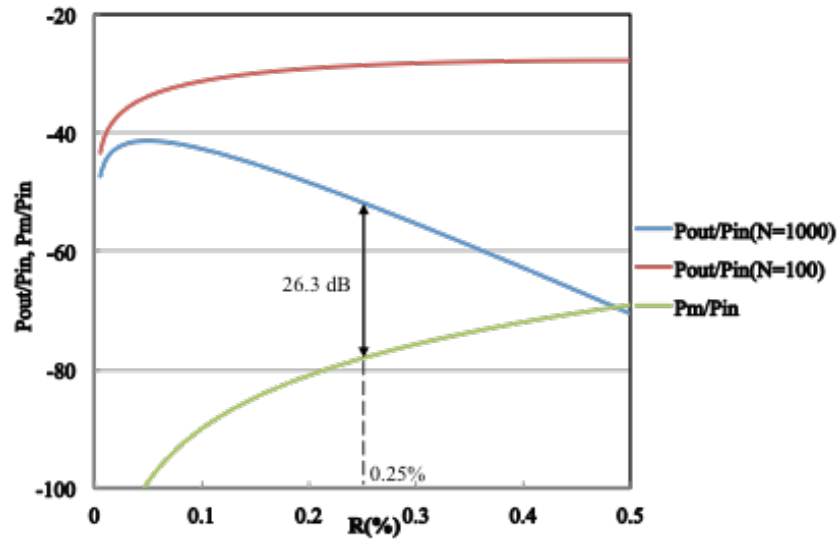


Figure 2.17 The output power P_{out} and the interference power P_m depend on the reflectivity of the partial reflector. Assuming the number of sensing regions $N=100$, the fiber loss factor $\alpha=0.2\text{dB/km}$, and the length of each sensing region $L=10\text{m}$.

The influence can be estimated by the ratio P_{out}/P_{in} and P_m/P_{in} as shown in Fig. 2.17.

Figure 2.17 is calculated on the basis of a 1km-long fiber sensing with the number of regions $N=100$, fiber loss $\alpha=0.2 \text{ dB/km}$ and the length of each region $L=10\text{m}$. These results indicate that P_{out} decreased as the reflectivity of partial reflector increases. On the other hand, interference power increases as R increases. These results mean that if we select low reflection with

partial reflectors, we can avoid the interference problems. Specifically, in the reflectivity range of $0.2\% < R < 0.45\%$, P_{out}/P_{in} approaches the maximum range, simultaneously P_m/P_{in} stays in the minimum range. Analysis of crosstalk shows using partial reflectors with 0.25% reflectivity, time averaged sensor-sensor crosstalk levels can be <30dB for an array of 25 sensors [85].

2.6.2 Chromatic dispersion

In the long sensing region, the sensing pulses are broadened during transmission by fiber chromatic dispersion, fiber nonlinearity and polarization dispersion. Especially, in the case where very short pulses are used to improve the time resolution of the technique. Next, we will analyze the influences of chromatic dispersion. We will consider the influence of the different pulse widths on pulse correlation measurement. Assuming the reference pulse with Full Width at Half Maximum FWHM = $(1 + \delta)\Delta\tau$ is expressed as

$$I_r(t) = \exp\left\{-4\ln 2 \times \frac{t^2}{\Delta\tau^2}\right\}, \quad (2.16)$$

Broadened pulse width approaches $(1 + \delta)\Delta\tau$, where δ is dispersion width factor.

$$I_m(t) = \exp\left\{-4\ln 2 \times \frac{t^2}{(1 + \delta)^2\Delta\tau^2}\right\}, \quad (2.17)$$

The resultant correlation output is

$$\begin{aligned} G(\tau) &= \int_{-\infty}^{\infty} I_r(t)I_m(t - \tau)dt \\ &= \frac{(1 + \delta)\Delta\tau\sqrt{\pi}}{2\sqrt{\{1 + (1 + \delta)^2\}\ln 2}} \times \exp\left[-\frac{4\ln 2}{\{1 + (1 + \delta)^2\}\Delta\tau^2}\tau^2\right] \end{aligned} \quad (2.18)$$

The resultant pulse FWHM width is $a = \sqrt{1 + (1 + \delta)^2}\Delta\tau$. The differential detection can be delayed $\sqrt{2}$ times of the FWHM, with the output

$$\begin{aligned} G_{dif}(\tau) &= \frac{(1 + \delta)\Delta\tau\sqrt{\pi}}{2\sqrt{\{1 + (1 + \delta)^2\}\ln 2}} \\ &\times \left[\exp\left[-\frac{4\ln 2}{a^2}(\tau + a/\sqrt{2})^2\right] - \exp\left[-\frac{4\ln 2}{a^2}(\tau - a/\sqrt{2})^2\right]\right], \end{aligned} \quad (2.19)$$

The slope of the differential output can be obtained by the derivation of Eq 2.19

$$\begin{aligned} \frac{dG_{dif}(\tau)}{d\tau} &= \frac{(1 + \delta)\sqrt{\pi \ln 2}}{2\Delta\tau\{1 + (1 + \delta)^2\}^{\frac{3}{2}}} \\ &\times [(\tau - \sqrt{2}a)\exp\{-\frac{4\ln 2}{a^2}(\tau - \sqrt{2}a)^2\}] \\ &- \tau\exp\{-\frac{4\ln 2}{a^2}\tau^2\}] \end{aligned} \quad (2.20)$$

The center of the slope sits at $\tau = a/\sqrt{2}$, the corresponding slope at this point is

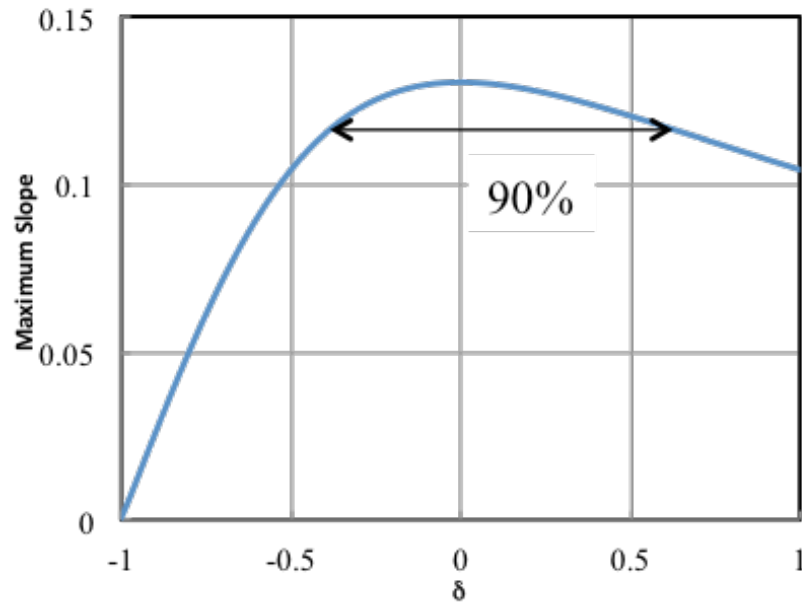


Figure 2.18 Central peak of the slope of output signal changes along with the dispersion width factor δ .

$$Y = \frac{\sqrt{2\pi \ln 2(1 + \delta)}}{8\{1 + (1 + \delta)^2\}}, \quad (2.21)$$

which is dependent on the value of δ as shown in Fig 2.18. If we assume the system can tolerate Y with a 10% reduction from its maximum value, then the allowable δ is obtained as $0.373 < \delta < 0.595$

Considering pulse chirp, the pulse width broadening b_f by chromatic dispersion is expressed as

$$\Delta\tau_m(z) = \sqrt{(1 + sCz/L_D)^2 + (z/L_D)^2}, \quad (2.22)$$

where $s = \text{sgn}(\beta_2)$, C is the chirp parameter, L_D is dispersion length calculated by $L_D = \Delta\tau^2 / (4|\beta_2| \ln 2)$.

And if the sensing fiber input power P_{in} is large, nonlinearity effects in the optical fiber will be observed. The most important nonlinearity is self-phase modulation (SPM) which causes frequency chirp and affects input sensing pulse by fiber chromatic dispersion. The influence of SPM can be expressed with the chirp parameter changes as

$$C = C_0 + C_{SPM}, \quad (2.23)$$

Where C_0 is the chirp parameter without SPM and C_{SPM} is expressed as

$$C_{SPM} = \sqrt{2} \frac{z\gamma P_{in}}{\alpha} \left(1 - \frac{1}{\alpha NL}\right), \quad (2.24)$$

where γ is the nonlinear parameter. The variation of sensing pulse width along with the propagation distance z is shown in Fig 2.19.

If we assume pulse width broadening is less than 1.5, then $z/L_D < 1.118$. Estimated allowable length L is

$$L < 1.118 \times L_D = 1.118 \frac{2\pi c \Delta\tau^2}{\lambda^2 D} = 1.118 \frac{\pi c \Delta\tau^2}{2\lambda^2 D \ln 2}, \quad (2.25)$$

If $\Delta\tau = 10\text{ps}$, $D = 1\text{ps/km/nm}$, then $L < 31.6\text{km}$.

If L is larger than 50 km, $D < 0.6\text{ps/km/nm}$.

Now, we will consider the temperature dependence of the fiber chromatic dispersion. If the technique is applied to a quasi-distributed temperature optical sensor, the chromatic dispersion can be influenced by the ambient temperature. If we use this technique to measure strain

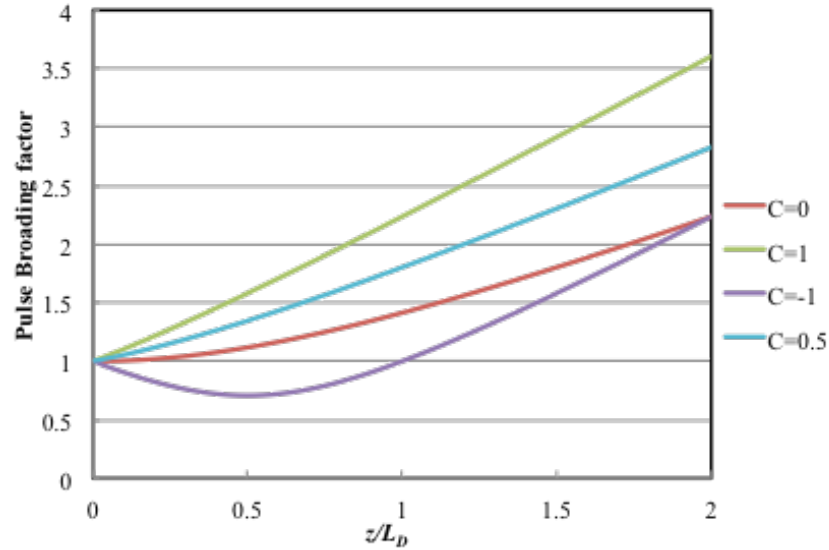


Figure 2.19 Pulse broadening factor changes as a function of propagation distance z for a Gaussian pulse propagating in the fiber. The blue curve corresponds to the case of an unchirped pulse. The green curves are obtained for chirp parameter $C=2$.

distribution, then the influence of chromatic dispersion would be the same observed as when measuring temperature. Therefore, we will estimate temperature dependence here. The dispersion slope S of dispersion shifted fiber (DSF) is $S < 0.085 \text{ps/nm/nm/km}$. Then, the allowable wavelength deviation from zero dispersion wavelength is 7nm, However, there is temperature dependence of the chromatic dispersion as shown in Fig 2.20.

This figure assumed the dispersion slope is 0.085ps/nm/nm/km and the temperature dependence of zero dispersion wavelengths is $0.028 \text{nm/}^\circ\text{C}$. The temperature dependence can be estimated as $0.238 \text{ps/nm/km/}^\circ\text{C}$ by these results. On the other hand, the temperature dependence of the fiber expansion is $0.085 \text{ps/m/}^\circ\text{C}$. Then, the influence of the chromatic dispersion is considered to be small enough.

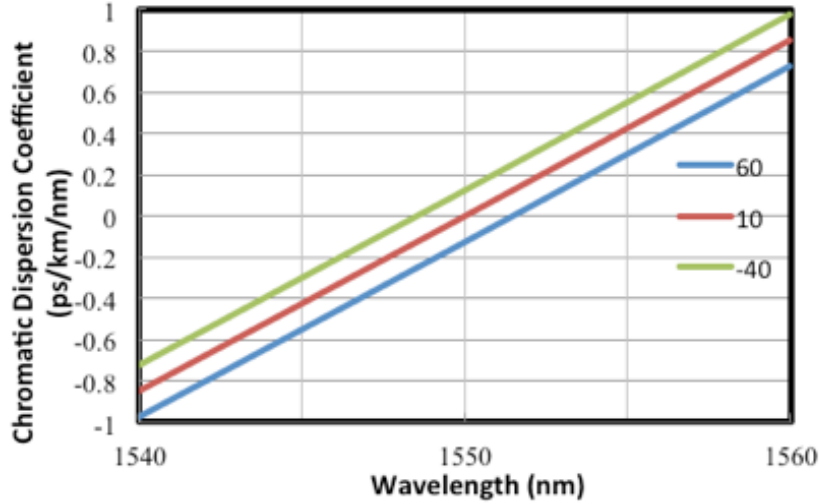


Figure 2.20 Temperature dependence of the chromatic dispersion.

2.6.3 Sensing length and number of sensing regions

According to the above analysis, if we construct the optical pulse correlation sensing using PSP light source ($\Delta\tau=10\text{ps}$), 1000 partial reflectors with 0.25% reflectivity and 10m spacing, the calculated output and input power ratio is $P_{\text{out}}/P_{\text{in}}=-51.8\text{ dB}$, and the signal to interference ratio is $P_{\text{in}}/P_{\text{m}}=28\text{ dB}$. Considering a system where the input pulse peak power is 100mW (20 dBm), the chirp parameter is estimated to be 0.6, and received peak power is -34.8 dBm. The total fiber length is 10 km then the round trip 20km. The chromatic dispersion influence is not large. Thus, a 10km-long optical correlation sensing with 1000 sensing points, 10m-long sensing spacing would be feasible.

2.7 Summary

In summary, a polarization scrambled pulse train (PSP) has been developed and applied to our optical pulse correlation sensing system. The stability of this system with polarization sensitive SHG receiver was well demonstrated. Compared with the results obtained using a conventional optical pulse (PMP), this technique has good resistance to polarization fluctuation.

The strain measurement of the system in various polarization states on a multi-sensing-region system has been demonstrated. Strain measurements along a meter-long region over kilometer distances in varying polarization states have been successfully performed. It is very useful in tele-monitoring situations. The consistency and high accuracy of the results show that this practical technique can be used for reliable sensing even in harsh environment tele-monitoring, such as gas transportation, power plants, and desert sensing.

Chapter 3

Quasi-distributed region selectable gas sensing for long distance pipeline maintenance

In this chapter, a novel optical gas tele-monitoring concept is proposed. By following this concept, we construct a long distance region selectable gas sensing system, which can address gases of single and/or different types at multi-locations. This approach is based on optical spectroscopy of selected absorption lines of gas leakage. A gas line spectrum can be addressed from a long distance monitoring center using optical fiber, gas sensing region and region selector. The region selecting technique monitors the selected gas absorption and identifies the location simultaneously. The technique has potential to be applied to long distance lightweight fiber optic wide-region gas sensing. A multi-region tele-monitoring experiment using FBG monitor as spectroscopy unit, long propagation fibers, gas cells as leakage sensing regions and FBGs as region selectors is demonstrated. Available numbers and coverage of multi-sensing regions are estimated using loss of sensing unit and propagation. Moreover, a technique to extend the number of the sensing regions is proposed and experimentally demonstrated.

3.1 Introduction

Pipelines are playing an increasingly important role in energy transportation, especially in the process of shipping hydrocarbons over long distances. Pipelines are popular infrastructure due to their safety and economy. However, being laid over long distances in remote areas, pipelines are typically affected by geohazards and harsh environmental conditions which may cause failures. Pipeline failure can lead to large business losses and environmental damage. Consequently, there is growing demand for the maintenance of pipeline over long distances. A system is required that has the ability to detect and locate problems such as leakage and emission along the pipeline. A technique that can perform multipoint and real-time monitoring is expected [86]–[88].

A lot of electrical gas sensing systems have been explored in order to satisfy the requirements of the gas industry. Gas sensing electrodes are free of the liquid junction potential problems associated with pH and ion sensitive electrodes, and are free of redox interferences, but the technique suffers from the limitation of dissolved gas [89]. A homogeneous semiconductor gas sensor array simply detects the resistivity from a variety of gases. The sensors can convert the concentrations of gases into an electrical signal. However, these electrical gas sensors are basically onsite point sensors with power supply [90].

Gas absorption spectroscopy [91] offers direct, accurate and highly selective means of gas measurement. Optical gas sensors can realize high sensitive detection of gas concentration [92]–[94]. However, they are not applicable in a long distance monitoring system, since they are usually composed of separate optical components. Optical fiber sensors are proven to be an effective method for environmental monitoring in various environmental processes [46]. When we apply optical fiber sensing technique to gas spectroscopy, we can probably realize a long distance optical gas tele-monitoring technique.

This chapter explains a new concept, which is capable of addressing multiple gas sensors in one single fiber, by inserting optical gas sensors into our region selectable system [47], [95]. Wavelength scanning LD and wavelength analyzer connect with optical fibers and region selectable reflectors to insert the light source and receive the results of spectroscopy of multi-

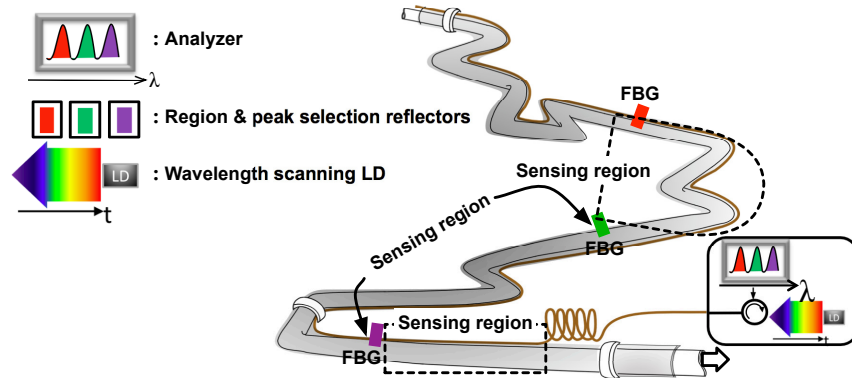


Figure 3.1 Conceptual schematic of the gas sensing for a long distance pipeline.

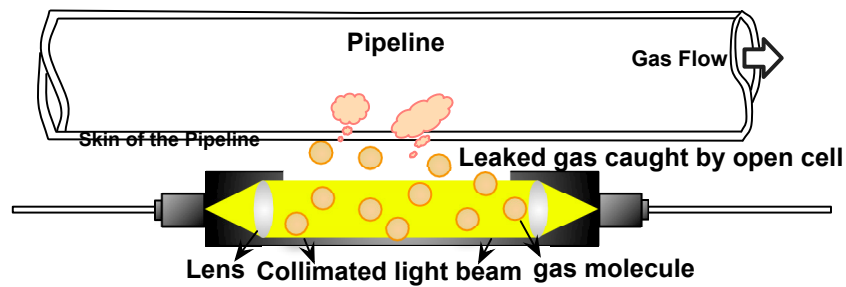


Figure 3.2 Conceptual schematic of the gas sensing for a long distance pipeline.

regions.

To distinguish multi-regions, gas spectroscopy combines with a region selectable technique by synchronizing a fiber Bragg grating (FBG) reflector with the target absorption line in each sensing region, as shown in Fig 3.1 and Fig 3.2. Spectroscopy performance under different temperatures, pressures and different leakage occurrences is measured. We discuss possible optical loss and estimated available sensing length of the system.

The remainder of this chapter is organized as follows. In section 3.2, the concept of quasi-distributed region selectable gas sensing is explained for one of its applications, long distance pipeline maintenance. Section 3.3 discusses basic tele-spectroscopy technique and its performance. Impact factors such as absorption line broadening and FBG instability have been discussed. Section 3.4 discusses multi-region gas sensing. The multi-sensing situation is dis-

cussed. In section 3.5, the performance of multi-region gas sensing over a km long distance is demonstrated and discussed. In section 3.6, a technique to increase the number of sensing regions by power division and time-dependent wavelength scanning and display is proposed and illustrated, the performance of the technique is experimentally demonstrated as well. Finally, a summary of this study is given in section 3.7.

3.2 Concept of region selectable gas sensing by tele-spectroscopy

3.2.1 Gas absorption spectroscopy and tele-spectroscopy

Many chemical species exhibit strong absorption in the UV/visible, near infrared or mid infrared regions of the electromagnetic spectrum. The absorption lines or bands are specific to each species, forming the basis for their detection and measurement. The absorption spectra in different spectra regions originated differently, e.g., the absorption in the UV spectra, 200-400nm, caused by the Electronic transitions; the absorption in near IR, 700nm- 2.5 μ m, originated from the first harmonic molecular vibration and rotation; while the absorption in mid IR, 2.5 μ m-14 μ m, comes from the fundamental molecular vibration and rotation [67]. Fig 3.3 shows the hydrogen cyanide H¹³C¹⁴N spectrum in near IR region, which has more than 50 strong absorption lines in the 1530-1565 nm region.

Optical gas detection using absorption spectroscopy is based on application of the Beer Lambert Law:

$$P = P_0 \exp(-\alpha l), \quad (3.1)$$

Where, P is the power of the light transmitted through the gas cloud, P_0 is the power of the incident light, α is the absorption coefficient of the gas species. L is the optical pathlength through the gas. The absorption coefficient α is the product of the gas concentration and the specific absorptivity of the gas ϵ .

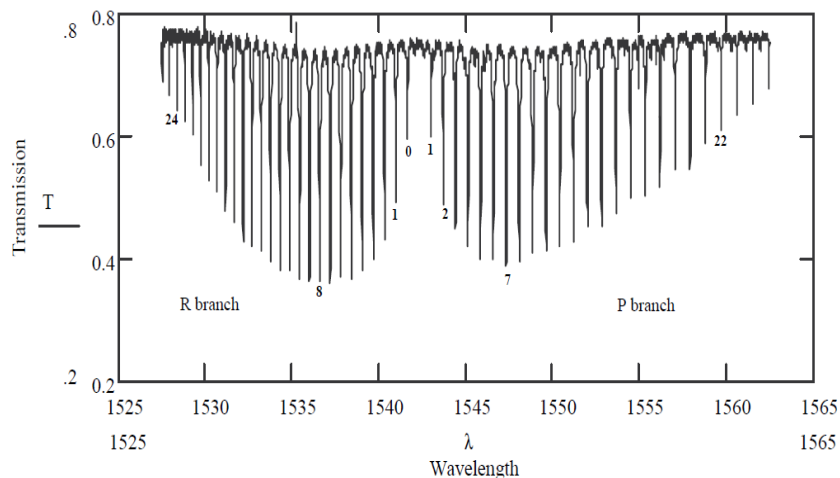


Figure 3.3 Hydrogen cyanide $\text{H}^{13}\text{C}^{14}\text{N } 2\nu_3$ rotational-vibrational band spectrum [96].

3.2.2 Concept of region selectable gas sensing by tele-spectroscopy

In our region selectable concept, we distinguish various sensing regions by different reflection wavelengths, which are selected by bandpass optical filters named region selectors in this work. When a gas absorption line center wavelength is selected in one sensing region, a gas absorption spectrum can be detected when gas exists in the region. In this paper, we would like to explain and demonstrate this concept of spectroscopy-based region selectable gas sensing for one of its potential applications, gas leakage monitoring of a gas pipeline. As shown in Fig 3.1, a pipeline with gas flowing inside is put in a suburb. The gas monitoring system is supposed to be set alongside the pipeline. The entire monitoring area is separated into several sensing regions by region selectors, i.e. FBGs in this study. In each sensing region, the gas absorption spectrum can be reflected back by the region selector. A wavelength scanning light source is needed to provide wavelength scanning light for the monitoring system. An analyzer is required to detect and record the reflected leakage gas spectrum and their distance. Leakage gas can be caught by the corresponding sensing region as shown Fig 3.2. Components which are able to capture the leaks, such as open gas cells or special sensing fiber [95], are used as sensing regions.

To directly detect the leakage, this gas sensing system should be set alongside the gas pipeline. When leaked gas flows out of the pipeline, the gas cell inside the sleeve picks up

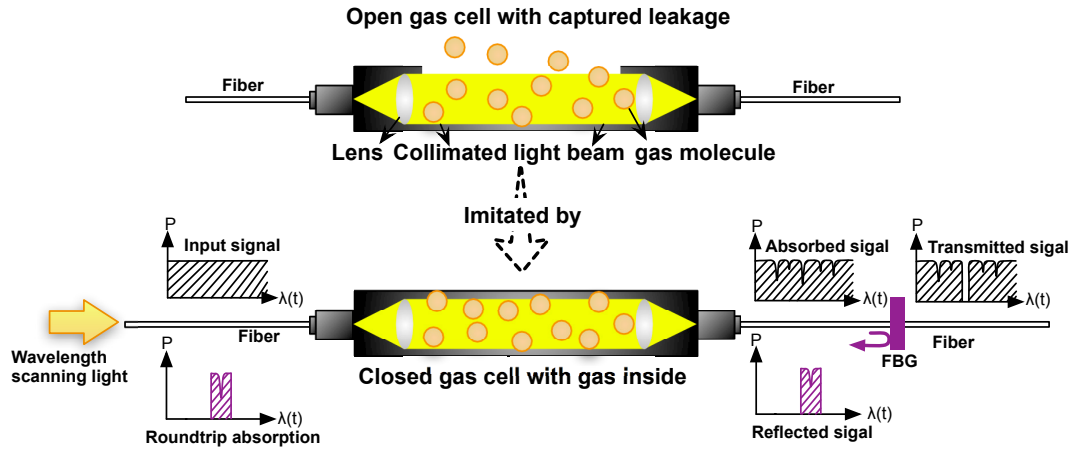


Figure 3.4 Imitation of gas leakage in pipeline using gas cell with fibers.

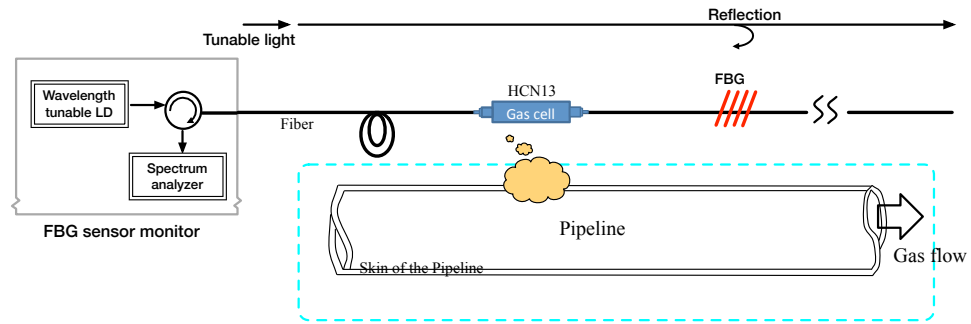
nearby gas leakage as shown Fig 3.1. This process could be imitated using a gas cell with fibers, as shown in Fig 3.4. We use a gas tube cell filled with hydrogen cyanide gas (HCN13) to work as leakage imitation. The cell receives scanning LD light through fibers. Scanning lightwave propagates through the gas cell and is partially reflected back by FBG. The roundtrip absorption profile is monitored.

3.3 Tele-spectroscopy by scanning-LD, FBGs and fibers

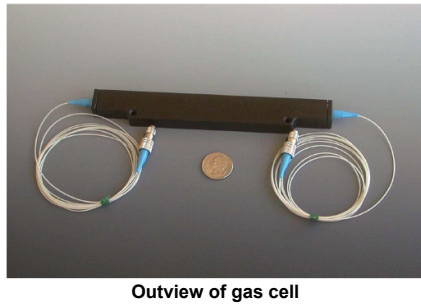
The concept of basic tele-spectroscopy technique and an experimental demonstration are explained in this section, including the schematic and signal analysis. Potential impacts on the technique such as the absorption line broadening and FBG vibration are also discussed here.

3.3.1 Schematic of tele-spectroscopy

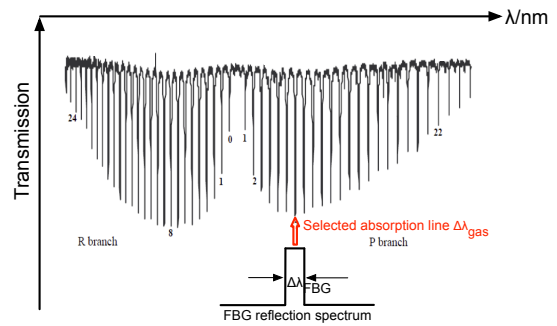
Schematic of tele-spectroscopy is shown in Fig 3.5(a). The technique uses long propagation fibers, an FBG monitor as spectroscopy unit, gas cells as leakage sensing regions and FBGs as region selectors. The FBG, which has almost complete reflection at selected wavelength range, adds to the sensitivity of the system. It is laid behind the sensing region to reflect



(a) Demonstration setup.



(b) Outview of gas cell [96].



(c) Synchronization of FBG and HCN13 gas absorption line.

Figure 3.5 Schematic of tele-spectroscopy gas sensing.

the absorption spectrum from which the location and species of the leakage can be analyzed. An FBG sensor monitor (Anritsu SF3011A) is composed of a wavelength analyzer with 0.01 nm resolution and a wavelength scanning LD with the scanning range from 1520 to 1570 nm. Wavelength scanned light [97] propagates through the sensing region in the fiber. The selected wavelength range is reflected back by FBG into the analyzer. If gas is located in the sensing region, roundtrip absorption will be measured and recorded as spectrum in this demonstration.

A hydrogen cyanide gas cell with fibers, as shown in Fig 3.5(b), is used to simulate the gas leakage from the sensing cell alongside the pipeline. A 16.5 cm long HCN13 gas packaged cell under weak pressure of 10 Torr was used for demonstration.

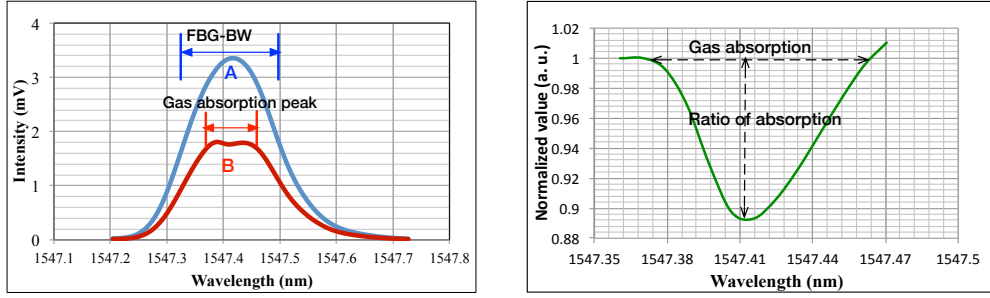
There are many absorption lines for each type of gas. The absorption spectrum of HCN13

gas can be seen from Fig 3.5(c). The wavelength range of the absorption lines of HCN13 gas, from 1525 to 1565 nm, is within the wavelength range of the scanning LD. It has more than 46 absorption lines [91], [98]. According to gas spectroscopy, when a light wave propagates through gas, the intensity of the light will reduce due to gas absorption. If we ensure the sensing region focus on one special absorption line, and select the target absorption line by region selector (FBG), the gas leakage could be detected by analyzing the reflected absorption spectrum. As shown in Fig 3.5(c), we choose one of the absorption lines, λ_{gas} , for detection, and synchronize the peak reflection wavelength of FBG, λ_{FBG} , with the target absorption line. The intensity of the spectrum at λ_{gas} can be monitored in this way. It needs to be noted that the bandwidth of the reflection spectrum of FBG, $\Delta\lambda_{\text{FBG}}$, is required to be broader than that of gas absorption lines, $\Delta\lambda_{\text{gas}}$.

In this demonstration, the target absorption line is P7 of [4, 14], 1547.4 nm. The 3 dB linewidth of the absorption line, which is less than 0.01 nm, is within the 3 dB bandwidth of the FBG reflection spectrum ($\Delta\lambda_{\text{FBG}} = 0.2$ nm). Therefore, absorption line of HCN13 gas, 1547.4 nm, can be monitored and analyzed.

3.3.2 Tele-spectroscopy experiment and analysis

The detected reflection spectrum and the signal analysis are shown in figures 3.6(a) and 3.6(b), respectively. Figure 3.6(a) expresses the intensity distribution of the reflected spectrum. Curve A illustrates the reflected power distribution when there is no gas in the objective region, i.e. gas cell does not exist in the system. Curve B illustrates the reflected power distribution when gas exists in the same sensing region. By comparing the intensity distribution of the two figures, we can see that the peak intensity and spectrum of the reflected signal is obviously reduced when gas cell exists in the region because of link loss with the gas cell. In order to analyze the absorption intensity more clearly, we divided the intensity of curve B spectrum by curve A at around wavelength range of λ_{FBG} and normalized the ratio as shown in Fig 3.6(b). The normalized transmissivity demonstrates the ratio of the cell transmitted power P_{trans} and FBG reflected power P_{in} , referred to as $P_{\text{trans}}/P_{\text{in}}$. Additionally, link loss has been eliminated in the



(a) Intensity distribution of detected signal.

(b) Normalized intensity distribution.

Figure 3.6 Absorption signal of reflected signal and normalized figure.

normalization process. The normalized figure shows that the minimum value appears at the wavelength of 1547.4 nm, which is well matched to the central wavelength of absorption line. The absorption depth is 11% when the gas pressure is 10 Torr, length of gas cell is 16.5 cm.

3.3.3 Discussion of tele-spectroscopy technique

The region selection technique by absorption peak wavelength selection suffers from the impact of the potential absorption line broadening in various temperatures and pressures. Additionally, the FBG profile at various temperatures affects the performance of the system as well. We measure the effects and discuss as follows.

3.3.3.1 Impact of absorption line broadening under varied temperatures and pressures

The transmitted power P_{trans} through gas leakage, is related to the absorption coefficient α and the absorption path length L according to equation 3.1:

$$P_{\text{trans}} = P_{\text{in}} \exp(-\alpha L), \quad (3.2)$$

where P_{in} is the power of the incident light.

We get the absorption ratio when we divide the absorption power ($P_{\text{in}} - P_{\text{trans}}$) by the incident light power P_{in} :

$$\begin{aligned} R &= \frac{P_{\text{in}} - P_{\text{trans}}}{P_{\text{in}}} \\ &= 1 - \exp(-\alpha L) \\ &\approx \alpha L, \end{aligned} \tag{3.3}$$

where we approximate $\alpha L \ll 1$.

The magnitude of absorption coefficient α is determined by absorption line of the gas, it also related to ambient temperature T and pressure P .

Linewidth broadening $\Delta\lambda_{\text{gas}}$ mainly caused by the interaction of the molecules during elastic collisions, which result in *Gaussian* broadening (caused by *Doppler* broadening, for example) and *Lorentzian* line shape, known as temperature broadening or pressure broadening.

The broadening of hydrogen cyanide gas absorption line P7 [91], [96] under different pressures and temperatures are measured in the following experiment. Two different HCN13 gas cells, 10 Torr, 5.5 cm long and 100 Torr, 5.5 cm long, are used for the demonstration under 290 and 320 K, respectively. Absorption depths and full widths at half maximum (FWHM) of the absorption line are measured. Absorption areas are calculated. During this demonstration, we only vary the ambient temperature of the gas cells, while the temperature of FBG is kept in the same range because the line broadening is negligibly small compared with the resolution of spectroscopy.

The experimental results show that temperature change did not impact the absorption linewidth under 100 Torr. HCN gas under 10 Torr, in contrast, suffered a FWHM broadening of 0.02 m from 290 to 320 K. Fortunately, such weak broadening does not impact the performance of the sensing system since the FWHMs of absorption line are within the 0.2 nm FWHM of the reflection spectrum of FBG, which is much wider than the 10 Torr absorption line. And the temperature dependence of other lines of HCN spectrum is not expected to be significantly different [99].

At each temperature, the detected FWHM of line P7 under 100 Torr is broader than that under 10 Torr. The absorption under 10 Torr is less than that under 100 Torr. However, gas

leakages in both cases are within the detectable range.

Table 3.1 Measured and estimated pressure dependence of line P₇ of HCN13 under varied pressures.

Pressure	10 Torr	100 Torr	760 Torr
FWHM(nm)	0.05	Measured 0.09 Estimated \approx 0.065	Estimated \approx 0.05

Table 3.1 lists the measured and estimated pressure broadening of line P₇ of HCN13 under various pressures at 290 K. We estimated the linewidth of line P₇ under 100 and 760 Torr using the data of [96].

Compared with the estimated linewidth under 100 Torr, the measured data are larger. This is reasonable as the measured value includes the error of the measurement device. Therefore, the measured result has good agreement with the estimated value.

In the case of leakage with 760 Torr pressure, that is 1 atm pressure, 100% leakage, the differential technique cannot catch an entire absorption line because the transition linewidth becomes wider than a typical FBG linewidth (0.2 nm). We can only tell the rough amount of gas leakage by directly reviewing the spectrum with selected FBG line disappearance.

In summary, we have demonstrated the temperature dependence and pressure dependence of line P₇ of HCN13 gas as well as the absorption under various temperatures and pressures. The slight temperature broadening of the linewidth of HCN13 gas is tolerable for this technique because the bandwidth of FBG is much larger than that of the absorption line. Compared to temperature broadening, pressure broadening is more obvious and apparently leads to increase of absorption depth; consequently, the absorption ratio has been improved greatly.

Additionally, this system focuses on fuel gases, which possess pure absorption spectroscopy with narrow absorption lines. In the case of fuel gas mixed with water vapor, we would like to treat water vapor as brief background of fuel gas measurement as H₂O has broad absorption band with line center wavelength of 1.38 μ m, from 1.32 to 1.56 μ m, which is not a sensitive chemical phenomena.

3.3.3.2 Impact of FBG instability

The peak reflection wavelength of typical FBG at 1550 nm band has an approximately 1 nm shift over 100°C temperature range which may cause some serious problems in a sensing system.

Fortunately, an athermal packaged FBG with passive or active temperature compensation [] is more reliable. Therefore, it can be applied in an ambient temperature range. An athermal packaged FBG is applicable for -5°C to +70°C in the case of $\Delta\lambda_{\text{FBG}} \sim 0.2$ nm due to the small shift (~ 0.07 nm) of FBG peak. Consequently, the target gas can be detected.

As to realistic pipeline monitoring, in order to avoid the fluctuation of FBG peak caused by the ambient temperature of the pipeline, commercial available athermal packaged FBG can be employed in the system.

3.4 Multi-region gas sensing demonstration

In this section, we would like to explain the concept of wide-region optical gas tele-monitoring by inserting tele-spectroscopy into the region selectable system. The performance of tele-spectroscopy applied to multi-region gas sensing has been demonstrated by constructing three-region gas sensing using FBG selectors. Absorption spectra of different occurrences of gas leakage have been detected. Leaks in different regions have been distinguished. The multi-sensing situation is discussed in this section.

3.4.1 Setup of three-region gas sensing demonstration

The schematic of three-region gas sensing is shown in Fig 3.7. The implementation of three-region selection is explained in the bottom half of figure 3.7. Different absorption lines λ_1 , λ_2 and λ_3 are selected from the P-branch of the gas spectrum in Fig 3.5(c) for sensing regions 1, 2 and 3, respectively. The peak reflection wavelength of $\lambda_{\text{FBG}i}$ ($i = 1, 2, 3$) for region i should be synchronized with $\lambda_{\text{gas}i}$, respectively.

The schematic of three-region gas sensing is shown in Fig 3.7. The implementation of three-region selection is explained in Fig 3.8. Different absorption lines λ_1 , λ_2 and λ_3 are selected

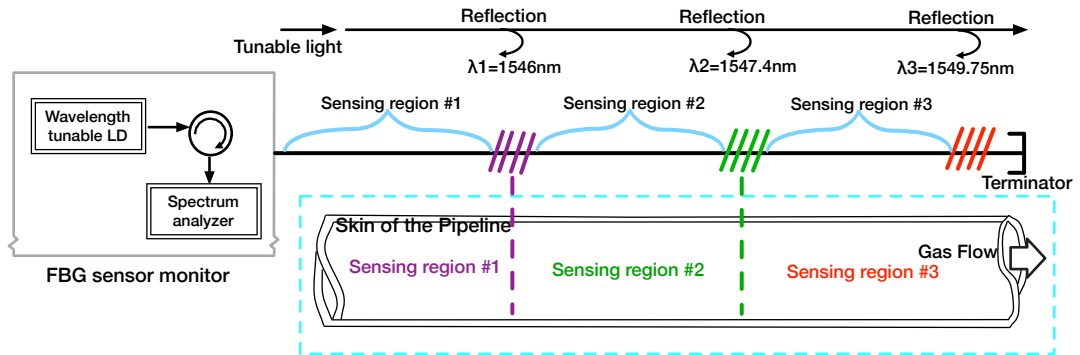


Figure 3.7 Schematic of three-region gas sensing demonstration. Setup of three-region gas sensing demonstration.

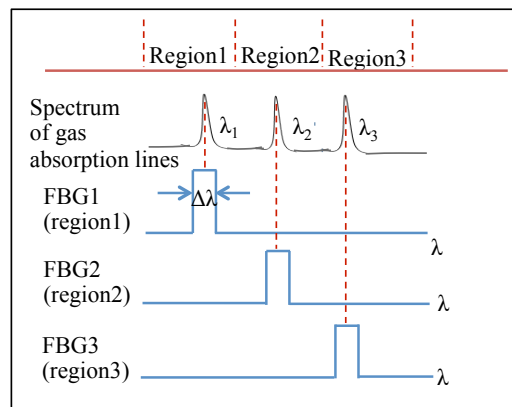


Figure 3.8 Synchronization of the FBG peak and absorption line.

from the P-branch of the gas spectrum in Fig 3.5(c) for sensing regions 1, 2 and 3, respectively. The peak reflection wavelength of $\lambda_{\text{FBG}i}$ ($i=1, 2, 3$) for region i should be synchronized with $\lambda_{\text{gas}i}$, respectively.

The three-region gas sensing setup is shown in figure 3.7. Three FBGs, whose peak reflection wavelength range $\Delta\lambda_{\text{FBG}i}$ includes the target absorption lines $\lambda_{\text{gas}i}$, are used to separate the sensing regions. HCN13 gas cells under pressure of 10 Torr are used to simulate the leakage at the sensing regions.

In this demonstration experiment, major absorption lines of HCN13 gas in Fig 3.5(c) at the wavelengths of P₅ (1546 nm), P₇ (1547.4 nm) and P₁₀ (1549.75 nm) are selected. The reflection peak wavelength of FBG1 is at 1546 nm, FBG2 is at 1547.4 nm, and FBG3 is at 1549.75 nm. The absorption sensitivity can be enhanced due to reflected roundtrip propagating and detection setup.

The reflected spectra of gas under four different situations are demonstrated. Firstly, we detect the spectrum when there is no gas absorption of leakage at any sensing region, defined as situation (a). Secondly, we measure the signal when only sensing region 2 has gas by connecting 16.5 cm long, 10 Torr gas cell in sensing region 2. This is named situation (b). Thirdly, the reflected spectrum when gas only exists in region 3 is measured. The gas cell is connected in sensing region 3 to simulate gas leakage. It is referred to as situation (c). Finally, we demonstrate the performance when both sensing region 2 and sensing region 3 have leakage. In this situation, 10 Torr, 5.5 cm long gas cell is connected in sensing region 2, and 10 Torr, 16.5 cm long hydrogen cyanide gas cell is connected in sensing region 3 simultaneously. This case is known as situation (d). The spectra of the four situations are detected and analyzed as follows.

3.4.2 Results of three-region gas sensing demonstration

The results of the demonstration experiment of the multi- region gas sensing system are shown in Fig 3.9. Reflected absorption spectra of situations (a), (b), (c) and (d) are shown in figures 3.9(a), 3.9(b), 3.9(c), and 3.9(d), respectively. The blue curve of situation (a) is due to the fact that there is no gas in the sensing regions, which becomes the reference of the mea-

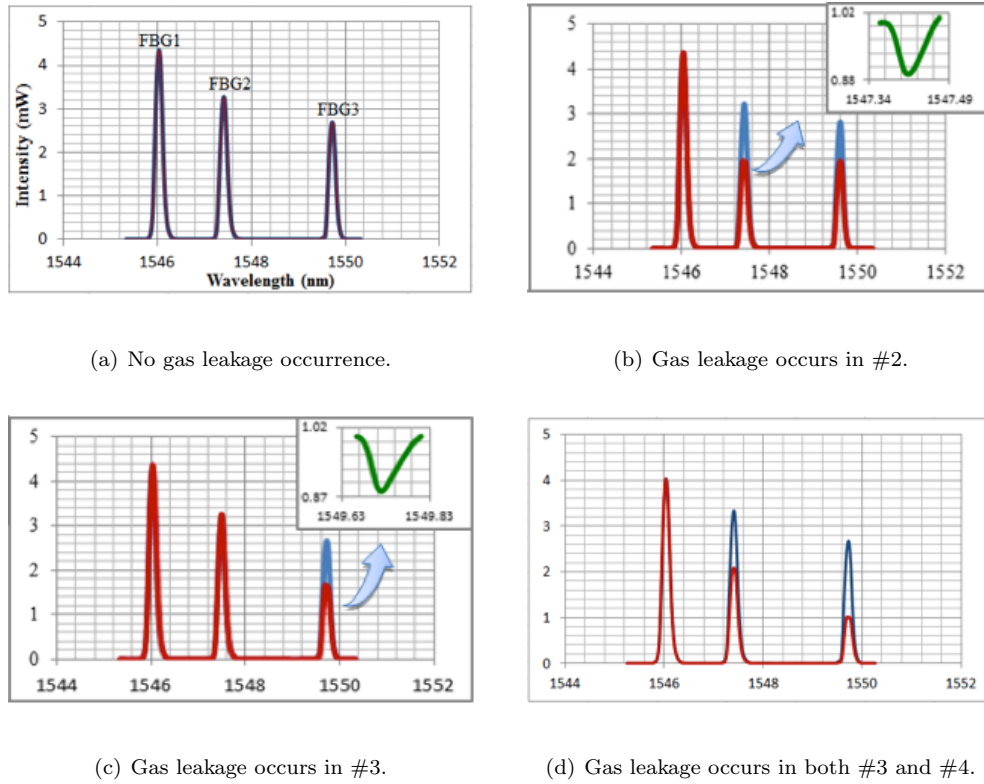


Figure 3.9 Absorption spectra of three-region gas sensing system under different gas leakage occurrences.

surement. The peak reflected spectrum of FBG2 has an absorption peak at the wavelength of 1547.4 nm, as shown in Fig 3.9(b), because gas exists in sensing region 2. The amplitude reduction of peak reflected spectrum of FBG3 is caused by the introduction of link loss. The normalized curve of case 2 in the small inset figure shows that the detected absorption depth is 11%. The absorption peak occurs in the reflected spectrum of FBG3 in case 3, as shown in Fig 3.9(c), due to the fact that gas exists in sensing region 3. The normalized figure shows that the absorption depth in this situation is 12%. In case 4, the absorption depths are 2.6% in sensing region 2 and 10.6% in sensing region 3, respectively, as shown in figure 3.9(d).

3.4.3 Analysis of multi-sensing situation

One of the important issues for multi-region gas sensing system is the discrimination of the locations of each gas leakage when problems occur. Due to the fact that a type of gas absorbs light at all absorption lines, in multi-regions, power reduction is present in the backward sensing regions even when leakage only exists in one sensing region. Using this three-region sensing model, we discuss the difference between situations (b), (c) and (d); gas leakages occur in both region 2 and region 3. The absorption R_{3d} in the peak of FBG3 contains the absorption in both sensing region 2 R_{32} and sensing region 3 R_{33} . Therefore, it is important to estimate the origin of power reduction in each region.

For multi-region gas sensing, the absorption ratio, equation 3.3, for i th absorption line ($i = 1, 2, 3$: where i means the i th sensing region) takes the form of

$$\begin{aligned} R &= \frac{P_{\text{in}} - P_{\text{trans}}}{P_{\text{in}}} \\ &= 1 - \exp(-\alpha_i L_j) \\ &\approx \alpha_i L_j, \end{aligned} \tag{3.4}$$

where α_i shows the absorption coefficient of the i th absorption line, j shows the absorption path length of the j th sensing region, $j = 1, 2, 3$. In situation (d) of this demonstration, $L_2 = 5.5$ cm and $L_3 = 16.5$ cm.

The detected absorption ratio R_{3d} of the third absorption line is given by

$$\begin{aligned} R_{3d} &= 1 - \exp(-\alpha_3 L_2) \times \exp(-\alpha_3 L_3) \\ &\approx \alpha_3 L_2 + \alpha_3 L_3 \\ &= R_{32} + R_{33}, \end{aligned} \tag{3.5}$$

In this demonstration experiment, λ_1 , λ_2 and λ_3 are near to each other, and α_1 , α_2 and α_3 have almost the same value.

Consequently, the detected ratio of the third absorption line is

$$R_{3d} = R_{33} + R_{32} \approx R_{33} + R_{22}, \quad (3.6)$$

The absorption depth in sensing region 2 is 2.6%, sensing region 3 is 10.6%, so the depth of absorption caused by the leakage in sensing region 3 would be about $10.6\% - 2.6\% = 8\%$.

To sum up, when gas absorption is present in sensing region 3, we should compare the detected absorption R_{3d} with forward sensing region R_{3d} .

If $R_{3d} - R_{2d} \approx 0$, it indicates the absorption in the third absorption line comes from leaks in forward sensing region.

If $R_{3d} - R_{2d} \gg 0$, it suggests that leaks also exist in region 3.

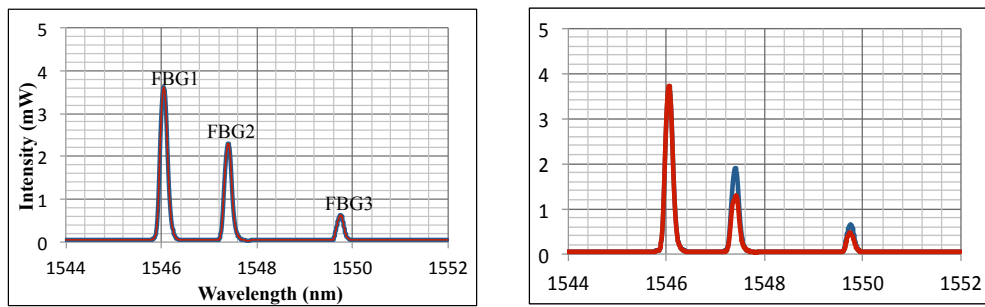
3.5 Long distance multi-region gas sensing

In this section we would like to explain the concept of long distance multi-region gas sensing by reporting both its schematic and performance. Available numbers and coverage of sensing regions are limited by the loss of sensing unit and fiber propagation. The possible sensing length is evaluated.

3.5.1 Demonstration of multi-region tele-monitoring

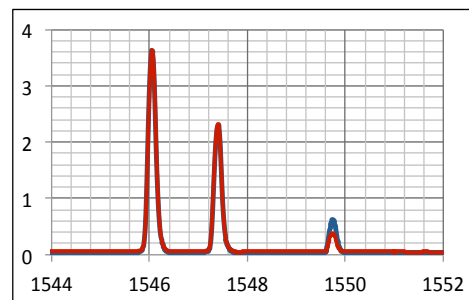
We demonstrated the performance of three-region gas sensing over 3 km. The schematic of the demonstration experiment is shown in figure 3.7. To construct sensing regions far from the monitoring center, long fibers with length of 1 km and 2.005 km are connected in front of sensing region 2 and sensing region 3, respectively. As in the multi-region gas sensing demonstration, this experiment uses FBG sensor monitor as wavelength scanning LD and spectrum analyzer, FBGs as region selectors and gas cell as sensing region.

Three different occurrences of leakage are detected and analyzed. Firstly, we measure the reflected spectrum when there is no leakage in any region, named situation (a). Then, we measure the response when leakage only exists in sensing region 2, called situation (b). Finally, we measure the absorption when leakage only exists in sensing region 3, referred to as situation



(a) No gas leakage occurrence.

(b) Gas leakage occurs in #2.



(c) Gas leakage occurs in #3.

Figure 3.10 Absorption spectra of long distance gas sensing system under different gas leakage occurrences.

(c). The recorded reflection spectrum and normalized absorption depth of the three situations are displayed in Fig 3.10.

When leakage only exists in sensing region 2, the absorption peak appears at the peak reflection wavelength of FBG2, and the analyzed absorption depth is 14.2%. It is 12% when the leakage only occurs in sensing region 3, the absorption peak is at the peak reflection wavelength of FBG3 in this situation.

3.5.2 Impact of optical loss in the design of gas sensing

The sensing length of this technique is limited by optical loss such as numbers of link loss for each sensing region and length of propagation in fiber.

When we take link loss into account, the transmissivity T_i of transmitted power and input power for sensing region i are given by

$$T_i = C^i \exp[-\alpha_F L_i], \quad (3.7)$$

where C is the coefficient of transmitted power related to coupling loss and L_i represents the distance between the monitor center and the i th sensing region. α_F is the loss parameter of optical fiber. It includes not only material absorption but also other sources of power attenuation. A typical optical fiber has 0.2 dB km^{-1} transmission loss, consequently, $\alpha_F \approx 0.046$.

We substitute $C = 0.71$ and $\alpha_F \approx 0.046$ in equation (3.7) and obtain

$$T_i = 0.71^i \exp[-0.046L_i], \quad (3.8)$$

The output power and minimum detectable power of FBG sensor monitor accept system loss within 30 dB. The maximum number of sensing region N is required to satisfy

$$10^{-3} \leq 0.71^N \exp[-0.046L_N], \quad (3.9)$$

Assuming the coverage of each sensing region is 1 km, the maximum number of sensing regions would be 19, the available sensing length is less than 20 km.

If the designed coverage of each sensing region is 10 km, the maximum number of sensing regions is 8, the corresponding sensing length approaches 80 km.

The total length and sensitivity of one system can easily be enhanced by inserting an optical fiber amplifier before detection.

3.6 Extension of the number of sensing regions

The number of regions with synchronized FBGs is limited by the numbers of absorption lines of each gas. In order to make the technique more applicable to long distance quasi-distributed gas sensing system, the technique for reusing the same gas absorption line was explored.

To indicate multiple sensing regions using the same gas absorption line, wavelength division multiplexing implementing in the current system must be converted into other types of multiplexing techniques, e.g., time division multiplexing, power division multiplexing, spacial division multiplexing, etc. Inspired by Optical Time Domain Reflectometer (OTDR), a time division like technique was realized by combing power division technique and time-dependent wavelength scanning and display characteristic of the FBG sensor monitor, making the number extension of sensing regions feasible. The FBG monitor (Anritsu SF3011A) in use is consisted of a wavelength scanning light source and a spectrum analyzer. The wavelength scanning light source in the monitor is capable of emitting time dependent wavelength scanning lightwave into transmission fibers and the spectrum analyzer can detect lightwaves reflected back by FBGs.

Both the wavelength scanning light source and spectrum analyzer read the wavelength of lightwave by time span and wavelength scanning speed of the FBG sensor monitor. The time dependent wavelength scanning scheme of the FBG sensor monitor causes the displayed wavelength shift to longer wavelength area in long range detection. More importantly, the FBG reflection wavelength displayed on the FBG sensor monitor linearly relates to the transmission time of the optical signal, enabling the displayed wavelength of the FBG sensor monitor to be linearly proportional to the transmission fiber length.

3.6.1 Wavelength shift of FBG sensor monitor

In stead of showing the real wavelength of the scanning spectrum, the displayed wavelength on FBG sensor monitor is calculated from the initial wavelength, pulse propagation time, and scanning velocity. Consequently, when connected to long fibers, the displayed wavelength of FBG sensor monitor will shift to longer wavelength as a result of the time-dependent wavelength scanning scheme of the FBG sensor monitor. Initiated at the same time origin, the wavelength scanning light source periodically emits lightwave into FBGs, meanwhile, the spectrum analyzer receives the reflected lightwave of FBGs, calculates the wavelength according to the time interval between the emission and reception of the lightwave which is defined as t_{delay} in this study, and displays on the screen.

For example, if an optical fibre with length of L , and refractive index of n is connected in front of an FBG with a central peak reflected wavelength of $\lambda_{original}$, signal emitted from light source at time t_1 , accounting for transmission time, the reflected signal will arrive the spectrum analyzer at time t_2 ,

$$t_{delay} = t_2 - t_1 = 2nL/c, \quad (3.10)$$

The displayed wavelength of FBG sensor monitor would be

$$\lambda_{dis}(\lambda_{original}, t_{delay}) = \lambda_{original} + \nu * t_{delay} \quad (3.11)$$

where ν is the scanning speed of the FBG sensor monitor. It should be noticed that if the fiber length L is short enough, τ can be neglected, which leads to $\lambda_{dis} \simeq \lambda_0$.

Fig 3.11 shows the relationship of displayed wavelength shift against transmission fiber length. It can be seen that the displayed wavelength of 1547.4nm on FBG sensor monitor shifts linearly to longer wavelength with the growth of transmission fiber length.

Assuming three FBGs with central wavelengths of $\lambda_1=1546\text{nm}$, $\lambda_2=1547.4\text{nm}$, and $\lambda_3=1549.75\text{nm}$ are connected to the FBG sensor monitor, as shown in Fig 3.12.

In short range detection, in which the connection fiber length can be approximate at 0, the displayed wavelength of FBG sensor monitor is $\lambda_{dis1}=1546\text{nm}$, $\lambda_{dis2}=1547.4\text{nm}$, and

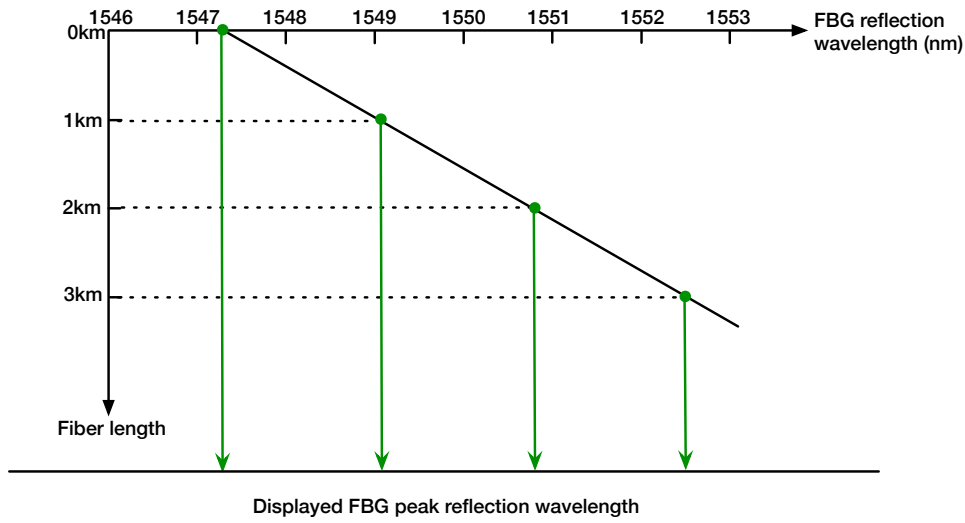


Figure 3.11 Wavelength shift at 1547.4nm over kilometer distance.

$\lambda_{dis3}=1549.75\text{nm}$, as shown in Fig 3.12(a).

By contrast, in long range detection, in which the fiber connection fiber lengths are more than kilometers, say 0km, 1km, and 2km as shown in Fig 3.12(b), redshift would appear in the displayed wavelengths.

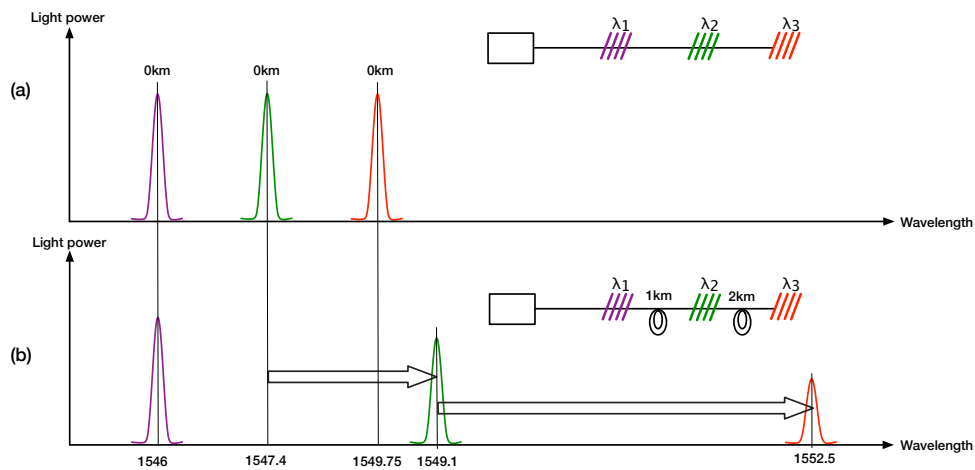


Figure 3.12 Wavelength shift of FBG sensor monitor in long distance.

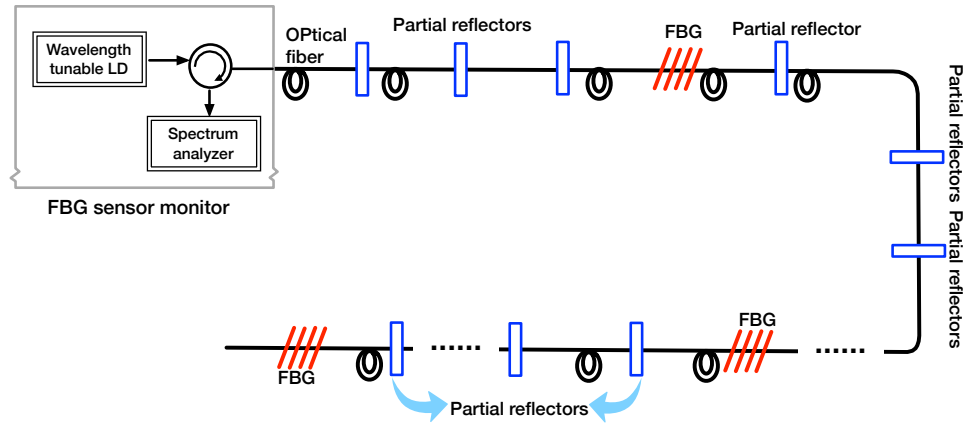


Figure 3.13 The concept of the extension technique of the number of sensing regions.

3.6.2 Principle of the number extension of sensing regions

The technique for increasing the number of sensing regions is shown in Fig 3.13. Regular fibers work as long distance light transmission path. FBG reflectors combine with partial reflectors to work as region separators in the system. FBGs are connected in the system to select different gas absorption lines. In front of each FBG, we set several partial reflectors to work as power separators. In this way, the gas absorption lines can be reused by the partial reflectors. Taking FBG1 in Fig 3.13 for example, if the peak reflection wavelength of FBG1 is synchronized with one gas absorption line λ_0 , the sensing regions in front of FBG1 could be separated by the intensity analysis at the wavelength of λ_0 of the reflected spectrum, because the displayed value λ_{dis} of λ_0 shifts with the transmission time, as expressed by Eq 3.12.

3.6.3 Experimental demonstration of sensing region extension technique

An experimental demonstration of the number of sensing region extension by partial reflector is given in this section.

3.6.3.1 Experimental measurement of displayed wavelength shift on FBG sensor monitor

Prior to the experimental demonstration of the region extension technique, the displayed wavelength shift of FBG sensor monitor has been detected with the absorption line P7=1547.4nm of HCN under test, as shown in table 3.2.

Table 3.2 Experimental measurement of the displayed wavelength shift of FBG sensor monitor over different transmission distances. The original wavelength under test is 1547.4nm

Transmission distance(km)	1	2.005	3.005
Displayed wavelength(nm)	1549.2	1550.89	1552.76

In this demonstration, the experiment relationship between the original wavelength $\lambda_{original}$ and displayed wavelength $\lambda_{dis}(\lambda_{original}, t_{delay})$ is

$$\begin{aligned} \lambda_{shift} &= \lambda_{display}(\lambda_{original}, t_{delay}) - \lambda_{original} \\ &= (1.7 \times c/2n) \times t_{delay}, \end{aligned} \tag{3.12}$$

3.6.3.2 Experimental setup

Fig 3.14 is a simplified experiment set up of Fig 3.13, which constructed by aFBG sensor monitor, a FBG, a partial reflector, and a terminator. The partial reflector whose reflectivity was 14% worked as power separator. FBG reflector worked as a wavelength separator in the system. HCN13 gas cell with fibers was used in the system to construct sensing regions instead of suspended core optical fibre. The selected HCN13 gas absorption line λ_0 in this experiment was 1547.4nm. The peak reflection wavelength of FBG was synchronized with the selected gas absorption line. We connected long fibers in the setup to realize long distance detection. The distance of sensing region1 was $L_1=1\text{km}$, and sensing region2, $L_2=2.005\text{km}$. Reflected spectrum will be detected and recorded by the analyzer in the FBG monitor.

Fig 3.11 shows the relationship of the displayed spectrum profile and the original spec-

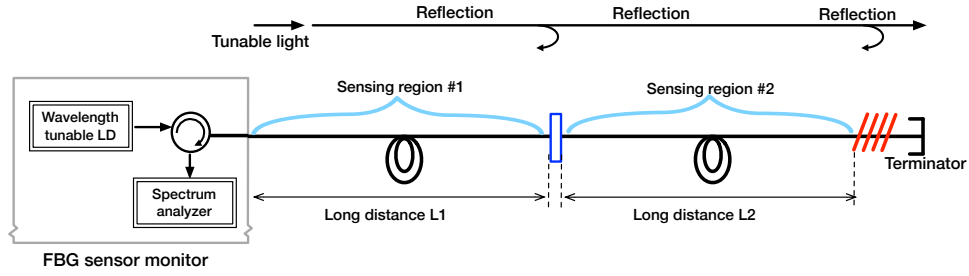


Figure 3.14 Instrument layout for 2 regions demonstration. $L_1=1\text{km}$, $L_2=2.005\text{km}$.

trum profile where time delay occurs. The horizontal axis represents the displayed wavelength of the spectrum analyzer which contains the information of both original light source wavelength and time delay. The vertical axis represents the original wavelength. The solid line shows the displayed spectrum profile when the transmission time is negligible, i.e. short distance measurement. The dashed lines show the displayed spectrum profiles due to time delay at the distances of L_1 and L_2 , respectively. We can see from the figure that the displayed wavelength of absorption line λ_0 at short transmission distance, long distance L_1 and L_2 are L_{short} , $\lambda_{\text{display1}}(\lambda_0, t_{\text{delay1}})$ and $\lambda_{\text{display2}}(\lambda_0, t_{\text{delay2}})$, respectively. if short time delay satisfies that $\lambda_0 \gg 1.7 \times c/2n \times t_{\text{delay}}$, displayed wavelength λ_{short} will be almost equal to original λ_0 , $\lambda_{\text{short}}=\lambda_0$.

According to equation 3.12,

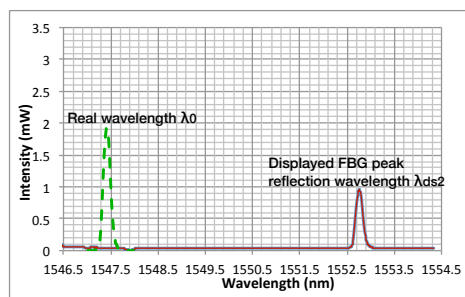
$$\lambda_{\text{display}} = \lambda_0 + 1.7 \times c/2n \times t_{\text{delay}} \quad (3.13)$$

The displayed wavelength of the gas absorption line λ_0 in the reflected spectrum will be $\lambda_{\text{dis1}}(\lambda_0, t_{\text{delay1}})$ for sensing region1 and $\lambda_{\text{dis2}}(\lambda_0, t_{\text{delay2}})$ for sensing region 2. Consequently, the two sensing regions could be separated easily. When gas exists in sensing region 1, the power of the signal at the absorption line, $\lambda_0 = 1547.4\text{nm}$, whose displayed wavelength is $\lambda_{\text{dis1}}(\lambda_0, t_{\text{delay1}})$, will be decreased, from the power reduction, we can estimate the existence and location of the leakage for sensing region 1. 86% of the power transmits to sensing region2 and is reflected back to the analyzer by FBG. The intensity reduction will appear at the absorption line whose

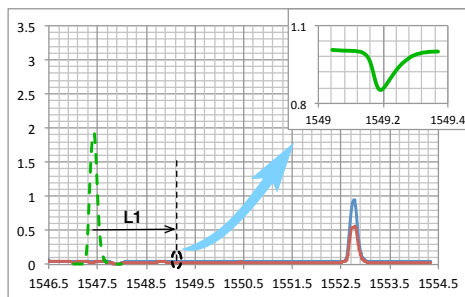
displayed wavelength is $\lambda_{dis2}(\lambda_0, t_{delay2})$ when gas exists in sensing region2. Three different occurrences of gas were detected, case 1, no gas leakage at any sensing region; case 2, only sensing region1 had gas; and case 3, gas only existed in sensing region2.

3.6.3.3 Experimental results

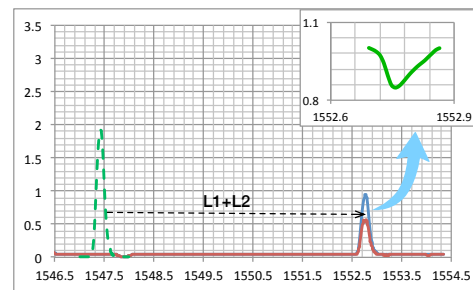
The performance of the demonstration experiment of the quasi-distributed system with partial reflector is estimated. Reflected absorption spectrums of case1, case2 and case3 are shown in Fig 3.15(a), 3.15(b), and 3.15(c), respectively. There is only one reflected peak since the partial reflector reflects the whole spectrum but only part of the power. The displayed wavelength of the gas absorption line is $\lambda_{dis1}(\lambda_0, t_{delay1})=1549.2\text{nm}$ at sensing region1 and $\lambda_{dis2}(\lambda_0, t_{delay2})=1552.76\text{nm}$ at sensing region2 due to time delay. As shown in Fig 3.15(a), the displayed central wavelength of peak reflection spectrum of the FBG reflector is $\lambda_{dis2}(\lambda_0, t_{delay2})=1552.76\text{nm}$, while the original absorption peak wavelength is 1547.4nm , as illustrated in Fig 3.11. When we detect the same absorption line in sensing region1 and sensing region 2, the intensity of the peak reflection spectrum of the FBG will be reduced even when gas only exists in sensing region1 as shown in Fig 3.15(b). However, we could distinguish the leakage location by analyzing the absorption proportion. For case2, we got an absorption proportion of 14.6% in sensing region1 and 12.6% in sensing region2. The absorption proportion of sensing region2 should be larger than that of sensing region1 if gas exists in both sensing region1 and region2, otherwise, leakage only occurs at sensing region 1. Absorption line only exists in the reflection spectrum of the FBG reflector when only sensing region2 has gas as shown in Fig 3.15. The absorption proportion in this case is 15.2%.



(a) No gas leakage occurrence.



(b) Gas leakage occurs in #2.



(c) Gas leakage occurs in #3.

Figure 3.15 Experimental results of the extension of sensing regions demonstration.

3.7 Summary

In this paper we proposed an innovative concept of gas sensing which can be used to detect the types and locations of gas at multiple regions over long distances. The technique is based on optical tele-spectroscopy and the fact that one kind of gas has numerous absorption lines. The basic concept of tele-spectroscopy was explained. Potential impact factors such as absorption line broadening under varied temperatures and pressures were demonstrated and discussed. Low pressure leakage around 10 Torr is detectable.

Multi-region tele-monitoring experiment using FBG monitor as spectroscopy unit, long propagation fibers, gas cells as leakage sensing regions and FBGs as region selectors is demonstrated. Four different situations of the existence of gas were measured. Leakage distinguishing in a multi-sensing situation was also discussed based on the three-region gas sensing demonstration. The location of the gas leakage was estimated by the absorption profile in the reflected spectrum.

The performance of multi-region tele-monitoring was demonstrated in this study as well. Long fibers were used to connect long distance absorption sensing regions. The results indicated that the technique worked well in long distance gas monitoring. Optical loss was analyzed and evaluated based on link loss and fiber propagation loss. The relationships between available region numbers and tele-monitoring length were estimated based on designed coverage of the sensing region. A technique was proposed to extend the number of sensing regions over long distance using the time dependent wavelength scanning scheme of FBG sensor monitor and power division multiplexing realized by partial reflectors. Good results was obtained on a two-region gas sensing experimental demonstration, indicating the technique is feasible.

The advantage of the approach is that it is simple, safe, cost effective and can be easily extended to long distance, multipoint sensing systems. The technique is capable of being used for long distance distributed pipeline maintenance.

Chapter 4

Plastic Optical Fiber Gas Sensing using OTDR

A gas detection concept using POF coated with gas sensitive chemical material has been proposed in this chapter. Combining with OTDR technique and silica fibers, a quasi-distributed gas sensing can be built which provides a practical possibility to be applied in hydrocarbon gas occurrence and location monitoring.

4.1 Introduction

Aside from gas spectroscopy described in chapter 3, chemical sensors are highly effective in gas detection [100]–[104].

A proper definition of chemical sensor is the so called “Cambridge definition” [102], [105]: *Chemical sensors are miniaturized devices that can deliver real time and on-line information on the presence of specific compounds or ions in even complex samples.*

Optical chemical sensors are growing quickly over the last few decades driven by such factors as low cost, miniature optoelectronic light sources and detectors. Fiber-optics chemical sensors (FOCS) enable optical spectroscopy to be performed over long distance, at sites conventional spectroscopy difficult to access, or even multi region detection along the optical fiber. By inte-

grating chemical analysis to optical sensing, particular interrogation methods, e.g., evanescent wave spectroscopy and spatially resolved lifetime spectroscopy, become practical. In addition, FOCSs capacitate the long-wave sensing that embraces weaker background signals and less expensive light sources [106]–[108].

FOCS can be classified into direct and indirect sensing schemes. In direct sensing, the intrinsic physical properties of an analyte, such as absorption and fluorescence, are detected. In the indirect sensing scheme, the analyte is monitored by a change in the optical response of an intermedia agent, such as a coated film, an immobilized indicator probe, an optically detectable label, etc. Another active research field includes advanced interrogation methods, e.g., time-resolved or spatially resolved spectroscopy, leaky mode spectroscopy, evanescent wave and laser-assisted spectroscopy, (localized) surface plasmon resonance, and multidimensional data acquisition [103], [104], [109].

FOCS have found numerous applications in gas detection field, gases such as Hydrogen, hydrocarbons, oxygen, ammonia, carbon dioxide, nitrogen oxides, etc., have been successfully detected by FOCS. Up to date, the detection of hydrocarbons and hydrogens have been attracting more attention in the field out of environmental protection. Distributed gas leakage detection has been successfully demonstrated using silica fiber-optics chemical sensor and OTDR [68]–[71]. However, along with the abundant advantages of FOCS, there is a hot potato in the area that the silica fiber-optics are so fragile that sensor heads based on them are easy to be broken, especially in the applications of reference [70], [71] where only the core of the fiber-optics are used. Plastic optical fiber (POF)s are good substitute to solve the problem [110] as they are flexible, cheap, and developed so fast that they have reasonably low transmission loss.

In this chapter, I would like to explore a quasi-distributed gas detection method by plastic optical fiber with one end coated with gas sensitive chemical material Cis-Polyisoprene (PIP), OTDR, silica fibers, and optical couplers.

The remainder of this chapter is organized as follows. Section 4.2 explains the concept of the GI-POF gas sensing by OTDR and the principle of Fresnel reflection power variation caused by the refractive index change of the chemical material in the presence of a specific gas.

As a pre-demonstration, ethyl alcohol is used as a substitute of gas, the difference of Fresnel reflection power at the POF-air interface, POF-alcohol interface, and POF-water interface are measured and analyzed which is given in section 4.3. A summary of the chapter and an outlook is presented in section 4.4.

4.2 Principle and scheme of POF gas sensing using OTDR

Some chemical polymers are known to be swelling in the presence of gas, such as Cis-Polyisoprene (PIP) meets hydrocarbon gases. Simultaneously, the polymer is undergoing remarkable refractive index reduction. Assuming an optical pulse train is launched into a plastic optical fiber (POF) with PIP coated at one end, in the presence of hydrocarbon gas, taking hexane for example, the Fresnel reflection power at the interface of PIP coating and air is varied, from which the occurrence and concentration of the gas can be assessed. When OTDR technique is introduced to measure the Fresnel reflection, the location of the gas analyte is possible to be determined as well.

4.2.1 Optical Time Domain Reflectometer OTDR [1]

The Optical time-domain reflectometry (OTDR) based on Rayleigh scattering is one of the most popular intrinsic distributed fiber optic sensors. It has been widely used to detect fault/imperfection location in fiber optic communications. As a sensing application, (OTDR can be effectively used to detect localized measurand-induced variations in the loss or scattering coefficient of a continuous sensing fiber.

The basic configuration of an OTDR is shown in Fig 4.1. A short pulse of light from a laser is launched into the fiber that needs to be tested. The photodetector detects the Rayleigh backscattering light intensity as a function of time relative to the input pulse. If the fiber is homogeneous and subject to a uniform environment, the backscattering intensity decays exponentially with time due to the intrinsic loss in the fiber. However, if at a particular location there is a nonuniform environment (e.g., having a localized perturbation), the loss coefficient at that particular location will be different from the regular Rayleigh scattering

coefficient. Thus, the backscattering intensity will not decay according to the exponential issue at other unperturbed locations. If we draw a curve using time as the horizontal axis and $\log(P_s)$ (where P_s is the detected) as the vertical axis, a sudden change in this curve is expected at the perturbed location, as shown in Fig 4.1.

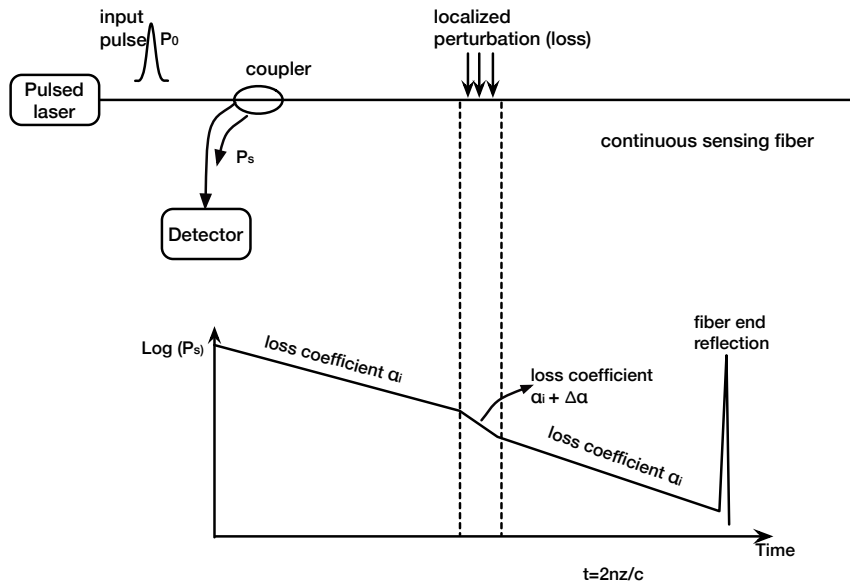


Figure 4.1 Principle of OTDR based on Rayleigh scattering.

When light is launched into an optical fiber, loss occurs due to Rayleigh scattering that arises as a result of random, microscopic (less than wavelength) variations in the index of refraction of the fiber core. A fraction of the light scattered in a counter propagation direction (i.e., 180° relative to the incident direction) is recaptured by the fiber aperture and returned toward the source. When a narrow optical pulse is launched in the fiber, by monitoring the variation of the Rayleigh backscattered signal intensity, one can determine the spatial variations in the fiber scattering coefficient, or attenuation. Since the scattering coefficient of a particular location reflects the local fiber status, by analyzing the reflection coefficient, one can sense the localized external perturbation or fiber status. Thus, distributed sensing can be realized. Since this sensing technique is based on detecting the reflected signal intensity of the light pulse as a function of time, this technique is called optical time-domain reflectometry (OTDR).

The detected scattering light intensity, P_s , is given by

$$P_s(t) = P_0 r(z) \exp\left\{-\int_0^z 2\alpha(z) dz\right\} \quad (4.1)$$

where P_0 is a constant determined by the input pulse energy and the fiber optic coupler power splitting ratio. $z = tc/2n$ reflects the location of the launched pulse at time t (where c is the light speed in vacuum, and n is the refractive index of the fiber), $r(z)$ is the effective backscattering reflection coefficient per unit length that takes into account the Rayleigh back scattering coefficient and fiber numerical aperture, and $\alpha(z)$ is the attenuation coefficient. The slope of the logarithm of the detected signal is proportional to the loss coefficient $\alpha(z)$.

The spatial resolution of an OTDR is the smallest distance between two scatters that can be resolved. If the input pulse has a width t , then the spatial resolution is given by

$$\Delta z = \frac{c\tau}{2n} \quad (4.2)$$

4.2.2 Operation principle of the POF sensor head

Polyisoprene is the polymer of isoprene (C_5H_8) that is the primary chemical constituent of natural rubber. Cis-Polyisoprene (PIP [111]) is one type among all the structures of Polyisoprene, which, however, has a configuration most closely mirrors the properties of natural rubber and is the most important commercially, it is going to be the focus of this article. The molecular structure of PIP is shown as Fig 4.2. In the presence of hydrocarbon gases (CH_x), PIP would swelling as a result of absorption, causing the reduction of refractive index as shown in Fig 4.3, which is the basis of the gas detection concept in this chapter.

Assuming a POF has one end coated with PIP, the other end injected with pulse light, as shown in Fig 4.4. The power of Fresnel reflection, defined as FR at the interface of PIP and air, is the physical parameter interested. Without the existence of gas as shown in Fig 4.4(a), FR_0 is going to be determined by Eq. 4.3,

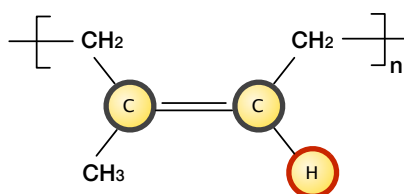


Figure 4.2 Molecular structure of cis isoprene.

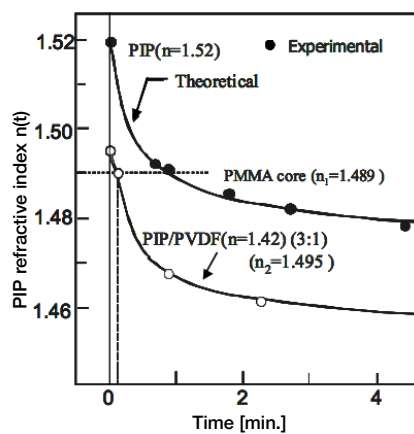


Figure 4.3 Refractive index reduction of PIP against time in the presence of hydrocarbon gases [112].

$$FR_0 = (n_{PIP} - n_{air})^2 / (n_{PIP} + n_{air})^2, \quad (4.3)$$

In the presence of hydrocarbon gases, the refractive index of PIP undergoes a reduction as a result of absorption swelling as shown in Fig 4.4(b), the Fresnel reflection FR_{gas} is defined by Eq. 4.4,

$$FR_{gas} = (n_{swelling} - n_{air})^2 / (n_{swelling} + n_{air})^2, \quad (4.4)$$

Assuming the refractive index of POF is $n_{POF} = 1.35$, $n_{air} = 1.0$, $n_{PIP} = 1.35$, $n_{swelling} = 1.3$, according to equation 4.3 and equation 4.4, the FR_0 and the FR_{gas} (in logarithm) are given by

$$\begin{aligned} FR_0 &= 10\log\{(n_{POF} - n_{PIP})^2 / (n_{POF} + n_{PIP})^2\} \\ &= 10\log\{(1.35 - 1.35)^2 / (1.35 + 1.35)^2\} \\ &= 0dB \end{aligned} \quad (4.5)$$

$$\begin{aligned} FR_{gas} &= 10\log\{(n_{POF} - n_{swelling})^2 / (n_{POF} + n_{swelling})^2\} \\ &= 10\log\{(1.35 - 1.3)^2 / (1.35 + 1.3)^2\} \\ &= -34.49dB \end{aligned} \quad (4.6)$$

Comparing with the case coating PIP at one end of silica fiber whose refractive index is $n_{silica} = 1.46$, the FR_0 and the FR_{gas} are calculated as

$$\begin{aligned} FR_{silica-0} &= 10\log\{(n_{silica} - n_{PIP})^2 / (n_{silica} + n_{PIP})^2\} \\ &= 10\log\{(1.46 - 1.35)^2 / (1.46 + 1.35)^2\} \\ &= -28.15dB \end{aligned} \quad (4.7)$$

$$\begin{aligned}
 FR_{silica-gas} &= 10\log\{(n_{silica} - n_{swelling})^2/(n_{silica} + n_{swelling})^2\} \\
 &= 10\log\{(1.46 - 1.3)^2/(1.46 + 1.3)^2\} \\
 &= -24.74dB
 \end{aligned}
 \tag{4.8}$$

The Fresnel power reduction in the presence of gas comparing that without the presence of gas is much larger using POF as sensing fiber (34.5dB) than silica fiber (3.59dB).

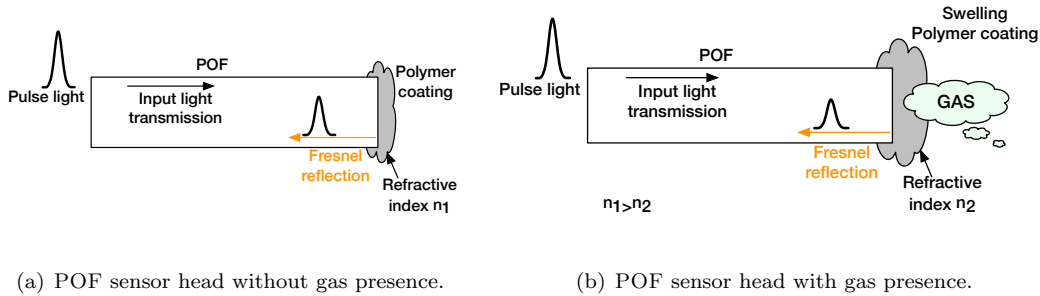


Figure 4.4 Schematic of POF sensor head and the polymer swelling in the presence of hydrocarbon gas.

4.2.3 Scheme of POF gas sensing using OTDR

A quasi-distributed sensing needs an OTDR to launch optical pulse and trace every event along the transmission line, and POF sensor heads are connected to the transmission line by optical couplers, dividing the sensing area into several sensing regions and monitoring the gas occurrence in each sensing region, as shown in Fig 4.5. GI silica fibers are designed to work as transmission line out of the consideration that GI fibers have low loss and less connection loss with POFs than single mode fibers do, as shown in table 4.1.

An optical pulse train from the OTDR transmits along the GI fiber to the first 1×2 optical coupler, where a certain percentage of optical power is guided into the POF sensor head, defined as sensing region #1, and the rest is guided along the transmission line until the second 1×2 optical coupler divides the optical power and guides them into sensing region

Table 4.1 Comparison of systems constructed by different types fibers

Parameter	Distance range	Spatial resolution	Sensitivity
all SMF	○	○	×
all GIF	○	○	×
all POF	×	○	○
GIF+POF	○	○	○

#2 and transmission line. The number of sensing regions depends on the input power and the receiver sensitivity of the OTDR, the transmission loss in fibers (including GI fiber and POF, especially the connection loss from POF to GI fiber), and the coupling ratio of the optical coupler. In the sensing region, the Fresnel reflection power at the interface of PIP coating and air from each sensing region is going to be detected by OTDR as shown in the lower part of Fig 4.5. The Fresnel reflection power in the presence of gas is smaller than that without the presence of gas, from which the gas occurrence can be assured. OTDR is able to tell the distance of the event, enabling the location determination of gas occurrence.

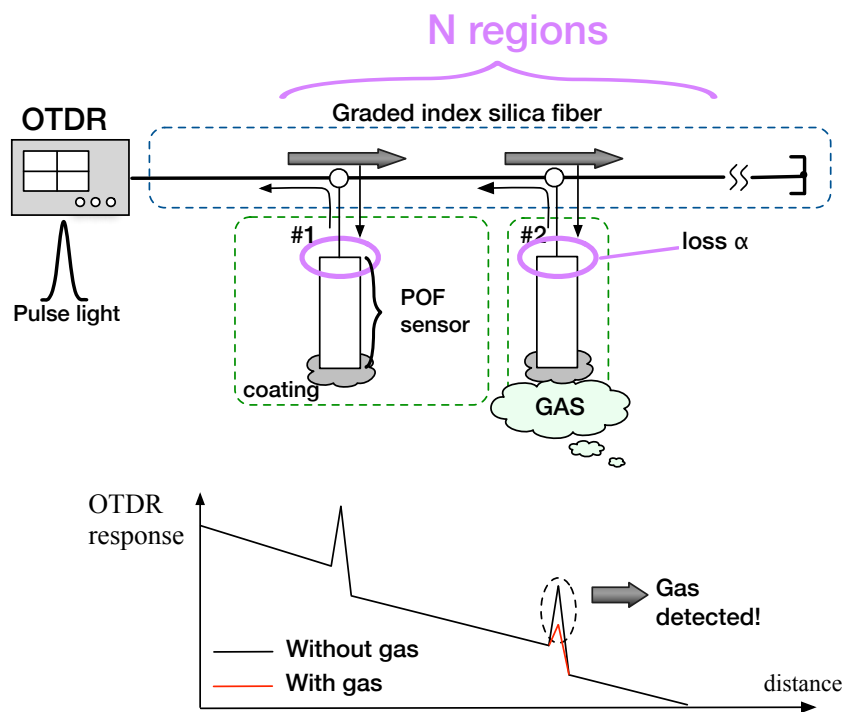


Figure 4.5 Connection loss from POF to silica fiber using pipes.

4.3 Pre-demonstration of POF gas sensing using OTDR

For some reason, the GI-POF sensor head has not prepared yet. Besides, the connection loss between silica fiber and POF has turned out to be difficult to reduce. In an investigation over one year, various connection techniques have been used on trial, such as directly alignment between silica fiber and POF, aligning through POF collimator, and/or GRIN lens. However, the transmission efficiency between silica fiber and POF, especially that from POF to silica fiber was not effectively improved until the commercial available GI-POF which has been decided to be used in the experimental demonstration.

Figure 4.6 to Fig 4.11 show the connection configurations between silica fiber and POF and corresponding losses from POF to silica fiber.

In Fig 4.6, single mode fiber (SMF), POF, and SMF are aligned using two copper pipes with different diameters, ϕ_{out} represents the outer diameter of the pipes, and ϕ_{in} indicates the inner diameter of the pipes. Light pulse at the wavelength of 1550nm is launched into SMF, Propagating to POF and SMF and detected by a power meter (with a resolution of 0.1nW). The transmission loss from light source to the end of the second SMF is 40dB.

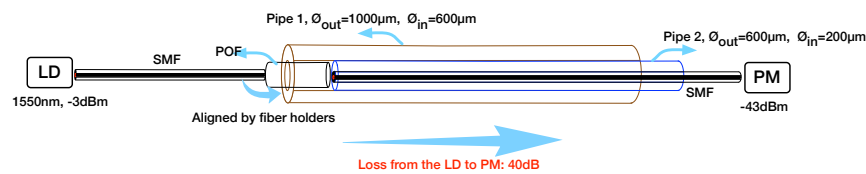


Figure 4.6 Connection loss from POF to silica fiber: using pipes.

In Fig 4.7, SMF collimator, POF collimator are used to align light. Graded-index (GRIN) lens is used to focus parallel light beam into a smaller spot diameter, which would improve the connection efficiency from POF to SMF. The wavelength of light pulse is 1550nm. The transmission loss from POF to SMF is 13.1dB.

In Fig 4.8, POF collimators are connected at the both ends of the POF. Multimode silica fiber with super large core diameter of $105\mu\text{m}$ is used to receive light from the POF. The wavelength of light pulse is 1550nm. The transmission loss from POF to SMF is 19dB.

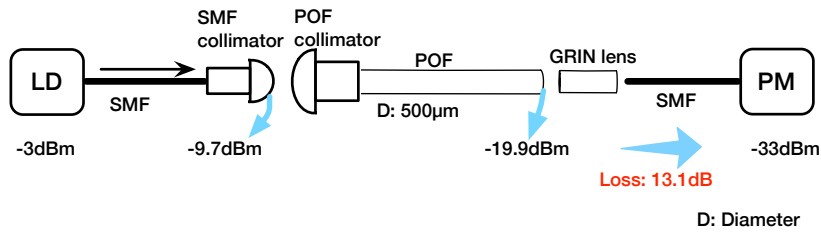


Figure 4.7 Connection loss from POF to silica fiber: using fiber collimator and GRIN lens.

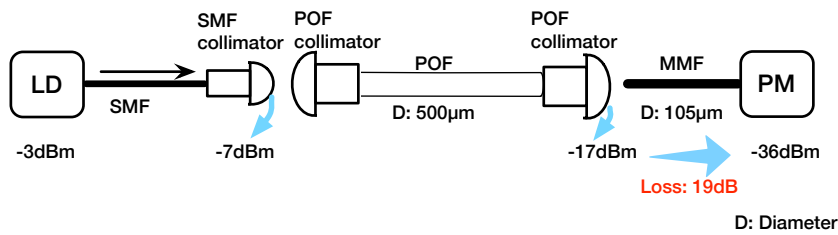


Figure 4.8 Connection loss from POF to silica fiber: using fiber collimator and large diameter silica MMF.

In Fig 4.9, normal multimode silica fiber with core diameter of 50µm is used to receive light from the POF. The wavelength of light pulse is 1550nm. The transmission loss from POF to SMF is 19.36dB.

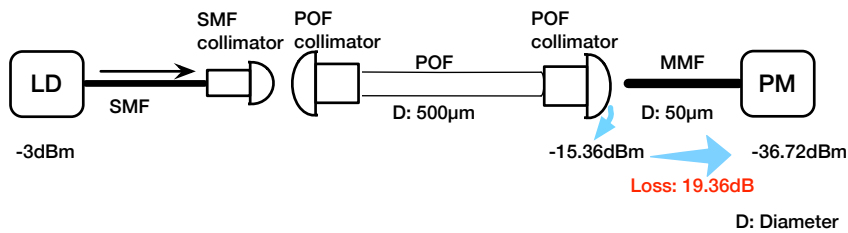


Figure 4.9 Connection loss from POF to silica fiber: using fiber collimator and normal silica MMF.

In Fig 4.10, a larger diameter POF, 900µm is used for test. normal multimode silica fiber with core diameter of 50µm is used to receive light from POF. The wavelength of light pulse is 1550nm. The transmission loss from POF to SMF is 17.4dB.

In Fig 4.11, the POF under test is 500µm, normal multimode silica fiber with core diameter

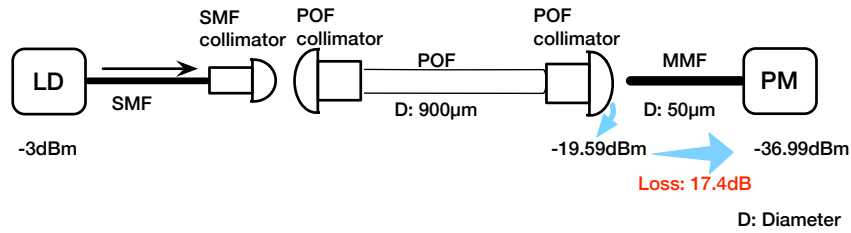


Figure 4.10 Connection loss from POF to silica fiber: using fiber collimator and large diameter POF.

of $50\mu\text{m}$ is used to receive light from POF. Matching oil is put between the POF and the MMF to reduce the connection loss. The wavelength of light pulse is 1550nm . The transmission loss from POF to SMF is 19.8dB .

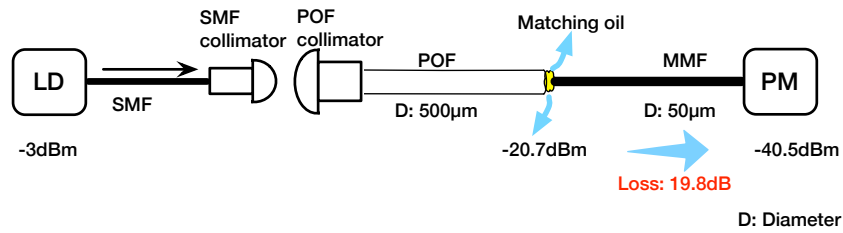


Figure 4.11 Connection loss from POF to silica fiber: using matching oil.

In this section, a pre-demonstration of POF gas sensing using OTDR, GI silica fiber, GI-POF, ethyl alcohol was implemented.

4.3.1 Set-up

The OTDR in use was mini OTDR AQ7275 (GI) with a wavelength capability spans from 850nm (MMF) to 1650nm (SMF), a dynamic range of up to 24dB and an 0.8m spatial resolution. To distinguish the 1m -long POF head in each region, the OTDR was adjusted to launch a light pulse train with a GI mode, wavelength of 1310nm , and pulse width of 3ns . GI silica fiber with lengths of 500m , 500m , and 100m were used to work as transmission line as shown in Fig 4.12. Two 1×2 multi-mode optical couplers with splitting ratio of $50\% \quad 50\%$ separated the whole area into three sensing regions, #1, #2, #3. In each sensing region, a 1m -long POF

worked as sensor head.

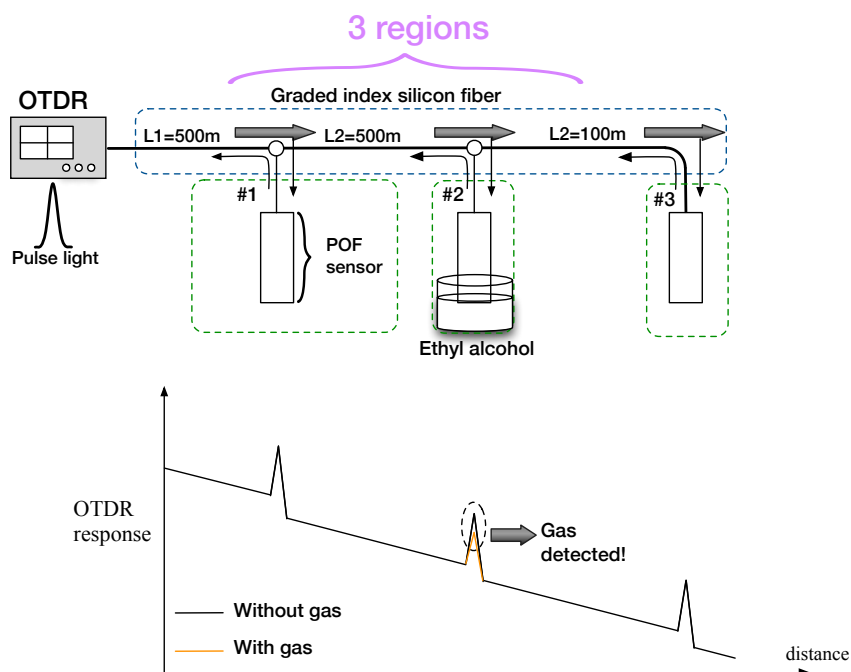


Figure 4.12 Experimental demonstration using OTDR, POF, and ethyl alcohol.

At the beginning, the three POF sensors were left in the air naturally, an averaged backscatter spectrum was recorded as shown by the black line of OTDR response in Fig 4.12. Secondly, POF of #1 was put in the ethyl alcohol (POF in #2 and #3 were left in air) to record a averaged backscatter spectrum. Then, POF of #2 and #3 were put in alcohol respectively to record the averaged reflection spectrum. The refractive index of GI-POF, ethyl alcohol, and water are shown in table 4.2

Table 4.2 Refractive index of GI-POF, ethyl alcohol, and water

	Refractive index
GI-POF	1.342-1.356
Ethyl alcohol	1.364
Water	1.32344 (detected at 1.13 μ m)

In the end, the same procedure went through again using water replace ethyl alcohol.

4.3.2 Results of experimental demonstration

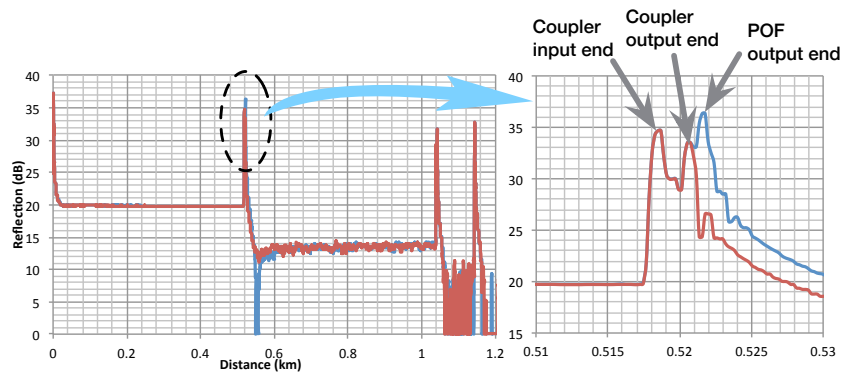
The experimental results are shown in Fig 4.13 and Fig 4.14.

Figure 4.13(a) shows the Fresnel reflection spectrum from the end of the first POF (#1) when it was in air (blue line) and in ethyl alcohol (red line). The right figure is the enlarged view of the part labeled by the ellipse in the left figure. There are three peaks in the spectrum, which caused by the reflection from the coupler input end, the coupler output end, and the POF end, as shown in the right figure of Fig 4.13(a). The blue line shows a peak (Fresnel reflection peak at the POF-air interface) at a length of 0.52156km where a small valley (Fresnel reflection peak at the POF-alcohol interface) appears in the red line. The measured power reduction between the blue peak (POF in air) and red valley (POF in ethyl alcohol) is 27.6dB.

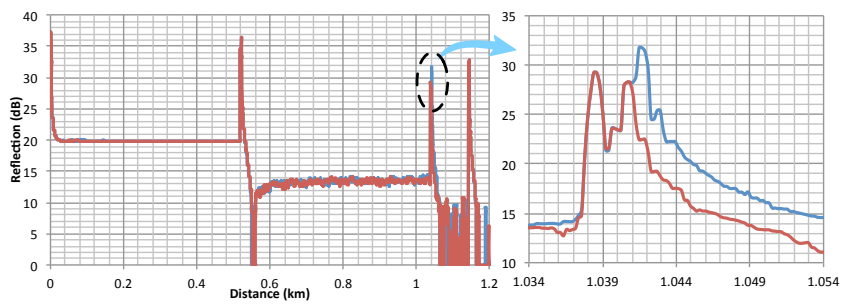
Figure 4.13(b) shows the Fresnel reflection spectrum from the end of the second POF (#2) when it was in air (blue line) and in ethyl alcohol (red line). The right figure is the enlarged view of the part labeled by the ellipse in the left figure. The blue line shows a peak (Fresnel reflection peak at the POF-air interface) at a length of 1.04147km where a small valley (Fresnel reflection peak at the POF-alcohol interface) appears in the red line. The power reduction between the blue peak (POF in air) and red valley (POF in ethyl alcohol) is 20.4dB.

Figure 4.13(c) shows the Fresnel reflection spectrum from the end of the third POF (#3) when it was in air (blue line) and in ethyl alcohol (red line). The right figure is the enlarged view of the part labeled by the ellipse in the left figure. The blue line shows a peak (Fresnel reflection peak at the POF-air interface) at a length of 1.14373km where a small valley (Fresnel reflection peak at the POF-alcohol interface) appears in the red line. The power reduction between the blue peak (POF in air) and red valley (POF in ethyl alcohol) is 22.628dB.

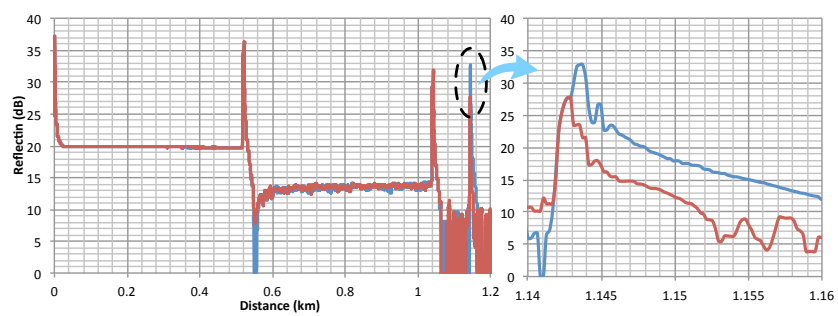
Figure 4.14(a) shows the Fresnel reflection spectrum from the end of the first POF (#1) it was in air (blue line) and in water (red line). The right figure is the enlarged view of the part labeled by the ellipse in the left figure. The blue line shows a peak (Fresnel reflection peak at the POF-air interface) at a length of 0.52258km where a small valley (Fresnel reflection peak



(a) Results of region #1.



(b) Results of #2.



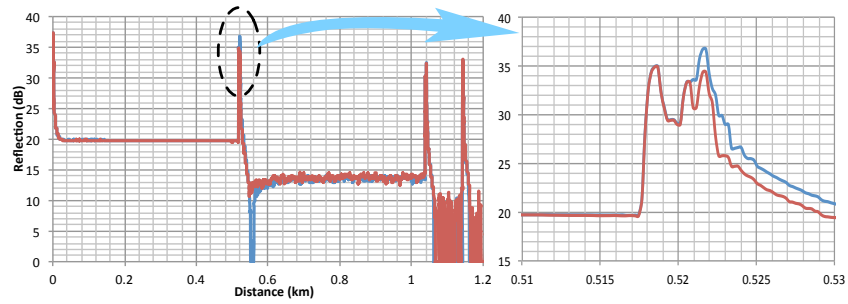
(c) Results of #3.

Figure 4.13 Fresnel reflection at the POF-air interface and the POF-alcohol interface.

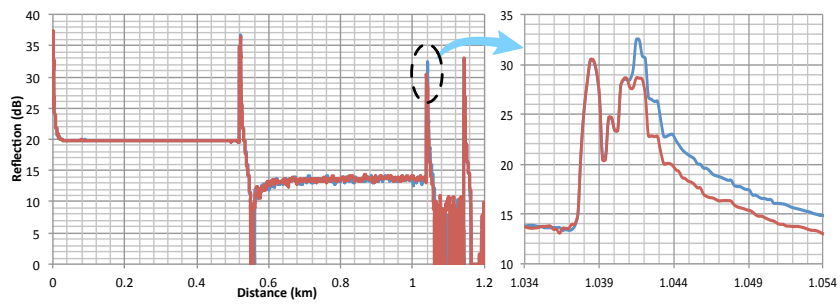
at the POF-water interface) appears in the red line. The power reduced 8.272dB from the blue peak (POF in air) and red valley (POF in water).

Figure 4.14(b) shows the Fresnel reflection spectrum from the end of the first POF (#2) it was in air (blue line) and in water (red line). The right figure is the enlarged view of the part labeled by the ellipse in the left figure. The blue line shows a peak (Fresnel reflection peak at the POF-air interface) at a length of 1.04147km where a small valley (Fresnel reflection peak at the POF-water interface) appears in the red line. The power reduced 7.682dB from the blue peak (POF in air) and red valley (POF in water).

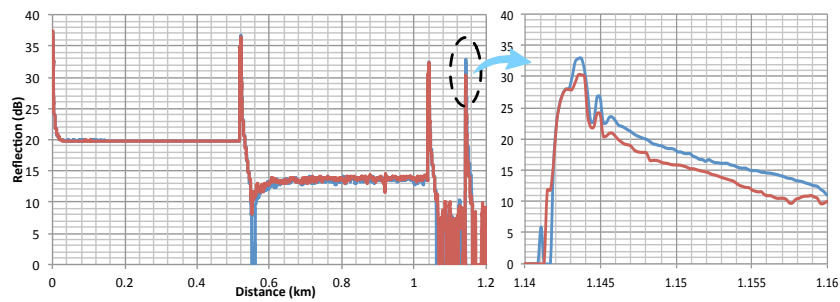
Figure 4.14(c) shows the Fresnel reflection spectrum from the end of the first POF (#3) it was in air (blue line) and in water (red line). The right figure is the enlarged view of the part labeled by the ellipse in the left figure. The blue line shows a peak (Fresnel reflection peak at the POF-air interface) at a length of 1.14352km where a small valley (Fresnel reflection peak at the POF-water interface) appears in the red line. The power reduced 6.638dB from the blue peak (POF in air) and red valley (POF in water).



(a) Results of #1.



(b) Results of #2.



(c) Results of #3.

Figure 4.14 Fresnel reflection at the POF-air interface and the POF-water interface.

4.4 Summary

A concept to realize quasi-distributed gas sensing using OTDR, GI fiber, GI-POF with PIP coating at one end, and optical couplers have been proposed in this chapter. According to the fact that the refractive index of PIP coating is reduced in the presence of hydrocarbon gases caused by PIP absorption swelling, and Fresnel reflection law, the power of reflection peak at the interface of PIP coating and air varies in the presence of hydrocarbon gases enabling the monitoring of hydrocarbon gas occurrence.

However, GI-POF with PIP coating at one end is not ready to use yet, therefore, a pre-demonstration on a three region POF sensing using mini OTDR AQ7275 (GI), GI fiber, GI-POF, optical couplers have been implemented. Power reduction of Fresnel reflection at the POF-air interface and POF-alcohol interface ($\sim 20\text{dB}$), and the power reduction at the POF-air interface and the POF-water interface ($\sim 7\text{dB}$) have been measured. Significant difference of Fresnel power reduction have been detected when dip POF into alcohol and water, showing that the method has practical possibility to be used in gas detection.

This research is going to be carried on when GI-POF with PIP coating is ready to use. The configuration would be the one shown in Fig 4.5. The Fresnel reflection of each sensing region, in air and in the presence of gas, is going to be detected, from which the refractive index change of the PIP in the presence of gas can be calculated, consequently the concentration of the gas can be estimated. The number of measurement points is decided by the input power, receiver sensitivity, coupling ratio, and fiber loss. The maximum measurement distance is dependent on the fiber loss and number of measurement points. And the sensitivity of the system is related to the coupling ratio and back scattering power.

Chapter 5

Conclusions

A summary of the work and a future work plan are given here.

5.1 Summary

Three techniques have been studied in this thesis. Firstly, I studied on polarization stabilized pulse train which can be used to eliminated the polarization fluctuation in pulse correlation sensing signal over long transmission line. On top of that I moved my study to optical gas sensing technique. A long distance region selectable gas sensing technique based on gas spectroscopy and region selectable technique has been successfully demonstrated. Moreover, a POF gas sensing concept has been proposed using GI-POF with PIP coating. A pre-demonstration of the concept has been implemented using OTDR, GI-POF, GI fiber, alcohol and water.

Pulse correlation measurement is a continuous study of our group began in 2004, the technique can be used in wide region, high sensitive temperature and strain measurement. However, the correlation signal suffered from polarization fluctuation over long distance transmission line caused by fiber birefringence and twisting. To solve the issue, I developed a polarization scrambled pulse train (PSP) by GS-LD modulated by an external RF signal, an optical delay line, an optical polarization state converter, optical couplers, and polarization maintain fibers. The pulse correlation signal with PSP light source has been examined in a polarization chang-

ing experiment with polarization sensitive SHG receiver. High consistency, with a fluctuation (defined by Eq 2.12) less than 4%, has been obtained. Next, the PSP has been applied to multi-region strain measurement using optical pulse correlation sensing in various polarization states. Fiber tensile strain measurements along a meter-long region over kilometer distances in varying polarization states have been successfully performed. A stable sensitivity of approximate $0.0021ps/\mu\epsilon$ has been obtained. It is very useful in tele-monitoring situations. The consistency and high accuracy of the results show that this practical technique can be used for reliable sensing even in harsh environment tele-monitoring, such as gas transportation, power plants, and desert sensing.

The second study is a quasi-distributed region selectable gas sensing for the application of long distance pipeline maintenance. In this study, an innovative concept of gas sensing which can be used to detect the types and locations of gas at multiple regions over long distances has been proposed. The technique is based on optical tele-spectroscopy and the fact that one kind of gas has numerous absorption lines. The basic concept of tele-spectroscopy was explained. Potential impact factors such as absorption line broadening under varied temperatures and pressures were demonstrated and discussed. Low pressure leakage around 10 Torr is detectable.

Multi-region tele-monitoring experiment using FBG monitor as spectroscopy unit, long propagation fibers, gas cells as leakage sensing regions and FBGs as region selectors was demonstrated. Four different situations of the existence of gas were measured, obtaining a normalized power reduction of more than 10% in the presence of gas. Leakage distinguishing in a multi-sensing situation was also discussed based on the three-region gas sensing demonstration. The location of the gas leakage was estimated by the absorption profile in the reflected spectrum.

The performance of multi-region tele-monitoring was demonstrated in this study as well. Long fibers were used to connect long distance absorption sensing regions. The results indicated that the technique worked well in long distance gas monitoring. Optical loss was analyzed and evaluated based on link loss and fiber propagation loss. The relationships between available region numbers and tele-monitoring length were estimated based on designed coverage of the sensing region, indicating tens of kilometers distance is possible to be measured. A technique

was proposed to extend the number of sensing regions over long distance using the time dependent wavelength scanning scheme of FBG sensor monitor and power division multiplexing realized by partial reflectors. Good results was obtained on a two-region gas sensing experimental demonstration, indicating the technique is feasible.

Following the above study, a concept to realize quasi-distributed hydrocarbon gas sensing using OTDR, GI fiber, GI-POF with PIP coating at one end, and optical couplers have been proposed. According to the fact that the refractive index of PIP coating is reduced in the presence of hydrocarbon gases caused by PIP absorption swelling, and Fresnel reflection law, the power of reflection peak at the interface of PIP coating and air varies in the presence of hydrocarbon gases, enabling the monitoring of hydrocarbon gas occurrence. However, GI-POF with PIP coating at one end is not ready to use yet, therefore, a pre-demonstration on a three region POF sensing using OTDR, GI fiber, GI-POF, and optical couplers, alcohol, and water have been implemented. Power reduction of Fresnel reflection at the POF-air interface and POF-alcohol interface has been measured, obtaining a approximate Fresnel reflection difference of 20dB. Simultaneously, the Fresnel reflection at the POF-air interface and POF-water interface have been measured, resulting a power difference of ~ 7 dB. The results show that the technique has potential to be used in hydrocarbon gas detection when POF sensor heads are ready to use, on which a discussion about the system parameters has been given in the summary of the chapter.

5.2 Outlooks

The demonstration of POF sensing for Hydrocarbon gas detection is going to be implemented once the POF sensor head with PIP coating is ready to use. Following that, I would like to study further on the topic of chapter 4 using step index POF coated with PIP cladding replaces GI-POF with PIP coating at one end. As discussed in chapter 4, the refractive index of PIP is going to be reduced in the presence of hydrocarbon gases. As shown in Fig 5.2, assuming a sensor head has POF core with refractive index of n_{pof} , and PIP coating with initial refractive index of n_1 , $n_{pof} < n_1$, the transmission mode in the sensor head would be leaky mode, thereby

the OTDR detected power from the sensor head would be limited. However, in the presence of hydrocarbon gases, the refractive index of the sensor head would be reduced to $n_{pof} > n_1$ as a result of absorption, where the transmission light in POF sensor is turning into guiding mode from leaky mode causing a Fresnel reflection peak to show at OTDR. Consequently, the occurrences and locations, even concentrations of hydrocarbon gases can be detected.

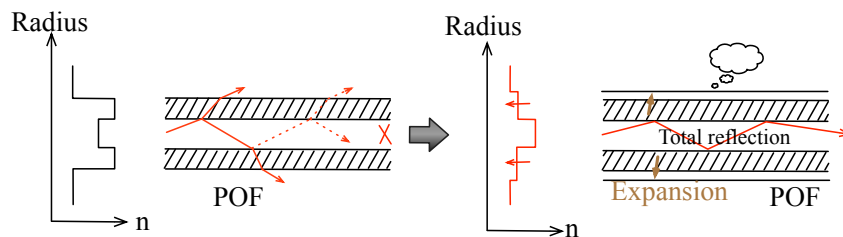


Figure 5.1 Index change of suspended core optical fiber in the presence of gas cloud.

On top of that, if it is possible, I would like to explore the distributed evanescent wave gas sensing using suspended core optical fibers with air hole on its surface, OTDR, and single mode fiber, as shown in Fig 5.2. Small air hole on the surface of suspended-core optical fibers work as gas tunnels where gas can spread inside of empty space of the fiber, as shown in Fig 5.3(a) and Fig 5.3(b) and Fig 5.3(c). A standard silica fiber works as link in and link out fiber. In order to reduce the insertion loss, firstly, it should fess and splicing the standard single mode fiber and the suspended core fiber, and then heating and drawing at the splicing point. In the presence of gas, there is going to be smaller absorption peaks in the OTDR spectrum as a result of gas absorption.

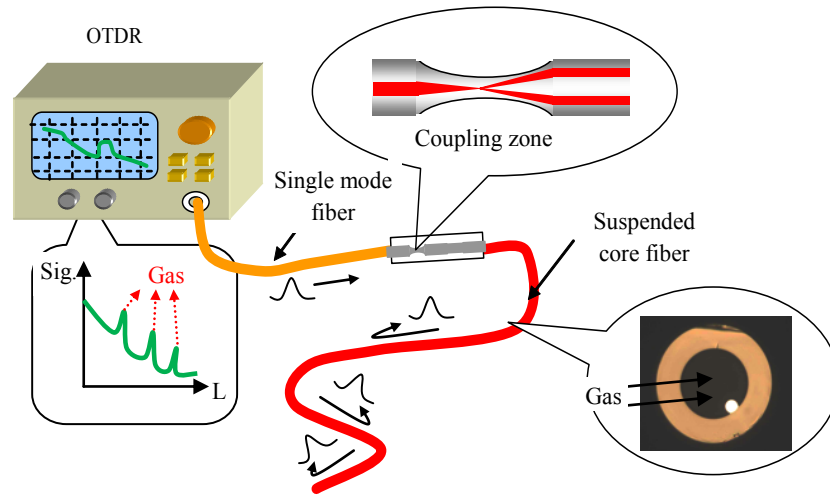
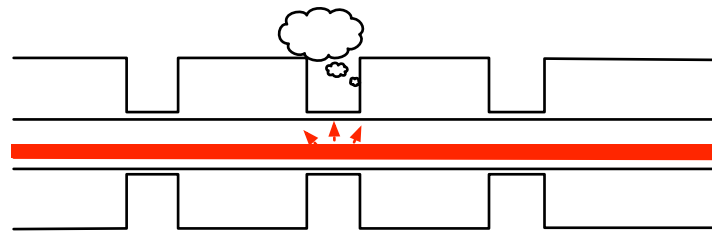
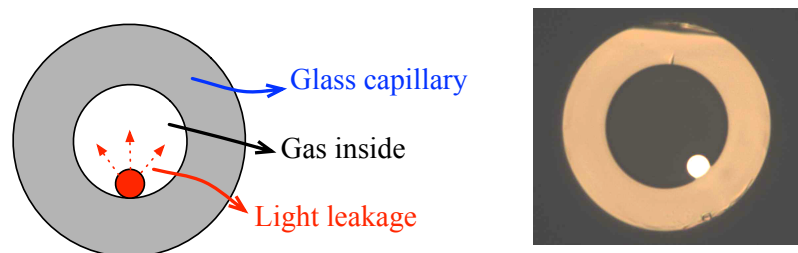


Figure 5.2 Schematic of evanescent gas sensing using suspended core optical fiber with air holes on its surface.



(a) Suspended core optical fiber with air hole on its surface.



(b) Cross section of suspended core optical fiber. (c) Sample of suspended core optical fiber.

Figure 5.3 Suspended core optical fiber for gas detection.

References

- [1] F. T. S. Yu and S. Yin, Eds., *Fiber optic sensors*. Dekker, 2002.
- [2] K. T. V. Grattan and T. Sun, “Fiber optic sensor technology: an overview,” *Sensors and Actuators A: Physical*, vol. 82, pp. 40–61, 11 1999.
- [3] J. Hecht, *City of light: Story of Fiber Optics*. New York: Oxford University Press, 1999.
- [4] A. C. S. V. Heel, “A new method of transporting optical images without aberrations,” *Nature*, vol. 173, 2 1954.
- [5] N. S. Kapany, “Fiber optics. vi. image quality and optical insulation,” *J. Opt. Soc. Am.*, vol. 49, no. 8, pp. 779–787, 2 1959.
- [6] N. S. Kapany, *Fiber Optics: Principles and Application*. San Diego, CA: Academic Press, 1967.
- [7] K. C. Kao and G. A. Hockham, “Dielectric-fibre surface waveguides for optical frequencies,” *Proc. IEE*, vol. 113, no. 7, pp. 1151–1158, 7 1966.
- [8] F. P. Kapron, D. B. Keck, and R. D. Maurer, “Radiation losses in glass optical waveguides,” *Appl. Phys. Lett.*, vol. 17, no. 10, pp. 423–425, 11 1970.
- [9] T. Miya, Y. Terunuma, T. Hosaka, and T. Miyashita, “Ultimate low-loss single-mode fibre at 1.55 μm ,” *Electron. Lett.*, vol. 15, no. 4, pp. 106–108, 2 1979.
- [10] G. P. Agrawal, *Lightwave Technology: components and Devices*. New Jersey: Wiley, 2004.
- [11] B. E. A. Saleh and M. C. Teich, *Fundamentals of Photonics: Chapter 8 Fiber Optics*. New York: Wiley, 1991.
- [12] Y. Koike and M. Asai, “The future of plastic optical fibers,” *NPG Asia Mat.*, vol. 1, pp. 22–28, 2 2009.
- [13] M. Asai, Y. Inuzuka, K. Koike, S. Takahashi, and Y. Koike, “High-bandwidth graded-index plastic optical fiber with low-attenuation, high-bending ability, and high-thermal stability for home-networks,” *J. Lightw. Technol.*, vol. 29, no. 11, pp. 1620–1626, 6 2011.
- [14] U. Fiedler, G. Reiner, P. Schnitzer, and K. J. Ebeling, “Top surface-emitting vertical-cavity LEDs for 10-gb/s data transmission,” *IEEE Photon. Technol. Lett.*, vol. 8, no. 6, pp. 746–748, 6 1996.

REFERENCES

- [15] J. Marcou, Ed., *Plastic optical fibers: practical application*. Wiley, 1997.
- [16] B. E. A. Saleh and M. C. Teich, *Fundamentals of Photonics*. Wiley, 2007.
- [17] P. Russell, "Photonic crystal fibers," *Science*, vol. 299, pp. 358–362, 1 2003.
- [18] P. S. Russell, "Photonic-crystal fibers," *J. Lightw. Technol.*, vol. 24, no. 12, pp. 4729–4749, 12 2006.
- [19] G. Humbert, J. C. Knight, G. Bouwmans, P. S. Russell, D. P. Williams, P. J. Roberts, and B. J. Mangan, "Hollow core photonic crystal fibers for beam delivery," *Opt. Express*, vol. 12, no. 8, pp. 1477–1484, 4 2004.
- [20] F. Luan, J. C. Knight, P. S. Russell, S. Campbell, D. Xiao, D. T. Reid, B. J. Mangan, D. P. Williams, and P. J. Roberts, "Femto- second soliton pulse delivery at 800 nm wavelength in hollow-core photonic bandgap fibers," *Opt. Express*, vol. 12, no. 5, pp. 835–840, 3 2004.
- [21] D. G. Ouzounov, F. R. Ahmad, D. Muller, N. Venkataraman, M. T. Gallagher, M. G. Thomas, J. Silcox, K. W. Koch, and A. L. Gaeta, "Generation of mw optical solitons in hollow-core photonic band-gap fibers," *Science*, vol. 301, no. 5604, pp. 1702–1704, 9 2003.
- [22] D. P. H. J. D. Shephard, J. D. C. Jones, G. Bouwmans, J. C. Knight, P. S. Russell, and B. J. Mangan, "High energy nanosecond pulses delivered single-mode through hollow-core pbg fibers," *Opt. Express*, vol. 12, no. 4, pp. 717–723, 2 2004.
- [23] J. D. Shephard, F. Couny, P. S. Russell, C. Jones, J. C. Knight, and D. P. Hand, "Improved hollow-core photonic crystal fiber design for delivery of nanosecond pulses in laser micromachining applications," *Appl. Opt.*, vol. 44, no. 21, pp. 4582–4588, 7 2005.
- [24] J. Limpert, T. Schriedber, S. Nolte, H. Zellmer, and A. Tünnermann, "All fiber chirped-pulse amplification system based on compression in air-guiding photonic band gap fiber," *Opt. Express*, vol. 11, no. 24, pp. 3332–3337, 2003.
- [25] C. J. S. de Matos, J. R. Taylor, T. P. Hansen, K. P. Hansen, and J. Broeng, "All-fiber chirped pulse amplification using highly dispersive air-core photonic band gap fiber," *Opt. Express*, vol. 11, no. 22, pp. 2832–2037, 2003.
- [26] P. S. J. Russell, "Light in a tight space: Enhancing matter-light interactions using photonic crystals," in *Proc. Conf. Nonlinear Opt. - (Optical Soc. Amer.)*, vol. 79, 2002, pp. 377–379.
- [27] P. S. J. Russell, E. Marin, A. Diez, and A. B. Movchan, "Sonic band gaps in pcf preforms: Enhancing the interaction of sound and light," *Opt. Express*, vol. 11, no. 20, pp. 2555–2560, October 2003.
- [28] S. Guenneau and A. B. Movchan, "Analysis of elastic band structures for oblique incidence," *Arch. Ration. Mech. Anal.*, vol. 171, no. 1, pp. 129–150, 2004.
- [29] V. Laude, A. Khelif, S. Benchabane, M. Wilm, T. Sylvestre, B. Kibler, A. Mussot, J. M. Dudley, and H. Maillotte, "Phononic band-gap guidance of acoustic modes in photonic crystal fibers," *Phys. Rev. B, Condens. Matter*, vol. 71, no. 4, 1 2005.

-
- [30] F. Benabid, G. Antonopoulos, J. C. Knight, and P. S. Russell, "Stimulated raman scattering in hydrogen-filled hollow-core photonic crystal fiber," *Science*, vol. 298, no. 2292, pp. 399–402, October 2002.
- [31] P. Rabinowitz, A. Stein, R. Brickman, and A. Kaldor, "Efficient tunable hydrogen raman laser," *Appl. phys. lett.*, vol. 35, no. 10, pp. 739–741, 11 1979.
- [32] L. S. Meng, K. S. Repasky, P. A. Roos, and J. L. Carlsten, "Widely tunable continuous-wave raman laser in diatomic hydrogen pumped by an external-cavity diode laser," *Opt. Lett.*, vol. 25, no. 7, pp. 472–474, 4 2000.
- [33] M. G. Kuzyk, *Polymer Fiber Optics: Materials, Physics, and Applications*. CRC Press, 2006.
- [34] K. Nakamura, I. R. Husdi, and S. Ueha, "A distributed strain sensor with the memory effect based on the pof otrd," in *Proc. SPIE, 17th international conference on optical fiber sensors*, vol. 5855, 8 2005.
- [35] Y.-J. Rao, "In-fibre bragg grating sensors," *Meas. Sci. Technol.*, vol. 8, pp. 355–375, 11 1996.
- [36] A. D. Kersey, M. A. Davis, H. J. Patrick, M. LeBlanc, and K. P. Koo, "Fiber grating sensors," *J. Lightw. Technol.*, vol. 15, no. 8, pp. 1442–1463, 8 1997.
- [37] V. A. Handerek, "Fiber gratings: principles, fabrication and properties," *Opt. Fiber Technol.*, vol. 2, p. 329, 1998.
- [38] Y. N. Ning and B. T. Meggitt, "Fiber bragg grating sensors: signal processing aspects," *Opt. Fiber Technol.: Devices and Technology*, vol. 2, p. 419, 1998.
- [39] W. Morey, G. Meltz, and W. Glenn, "Fiber bragg grating sensors," *Fiber Optic and Laser Sensors , Proc. SPIE*, vol. 1169, 1989.
- [40] M. Lu, K. Nonaka, H. Kobayashi, J. Yang, and L. Yuan, "Quasi-distributed region selectable gas sensing for long distance pipeline maintenance," *Meas. Sci. Technol.*, vol. 24, p. 095104, 8 2013.
- [41] K. Uchiyama, K. Nonaka, and H. Takara, "Subpicosecond timing control using optical double-pulses correlation measurement," *IEEE Photon. Technol. Lett.*, vol. 16, no. 2, pp. 626–628, 2004.
- [42] K. Nonaka, M. Sato, and T. Suzuki, "Optical pulse timing drift sensing for fiber delay monitoring using pulses correlation and differential detection," in *17th Int. Conf. Optical Fibre Sensors*, vol. 5855. Bellingham, WA: Proc. of SPIE, 2005, pp. 76–79.
- [43] H. B. Song, T. Suzuki, M. Sato, and K. Nonaka, "High time resolution fibre optic sensing system based on correaltion and differential technique," *Meas. Sci. Technol.*, vol. 17, pp. 631–634, 2 2006.
- [44] H. B. Song, T. Suzuki, T. Fujimura, K. Nonaka, T. Shioda, and T. Kurokawa, "Polarization fluctuation suppression and sensitivity enhancement of an optical correlation sensing system," *Meas. Sci. Technol.*, vol. 18, pp. 3230–3234, 9 2007.
- [45] X. Xu and K. Nonaka, "High-sensitivity fiber-optic temperature sensing system based on optical pulse correlation and time-division multiplexer technique," *Jpn. J. Appl. Phys.*, vol. 48, October 2009.

REFERENCES

- [46] X. Xu, A. Bueno, K. Nonaka, and S. Sales, "Fiber strain measurement for wide region quasi-distributed sensign by optical correlation sensor with region separation techniques," *J. Sens.*, vol. 2010, 5 2010.
- [47] X. J. Xu and K. Nonaka, "A region selectable distributed fibre-optic sensing system based on pulse correlation and partial reflectors," *Meas. Sci. Technol.*, vol. 21, no. 9, 7 2010.
- [48] H. Kobayashi, T. Tsuzuki, T. Onishi, Y. Masaoka, X. Xu, and K. Nonaka, "Suppression of instability on sensing signal of optical pulse correlation measurement in remote fiber sensing," *J. Sens.*, vol. 2012, 12 2012.
- [49] M. Lu, H. Kobayashi, and K. Nonaka, "Polarization-stabilized pulse correlation measurement for remote fiber sensing using polarization scrambled pulses," *Jpn. J. Appl. Phys.*, vol. 52, 9 2013.
- [50] B. Culshaw and W. C. Michie, "Optical fiber sensors and their role in smart structures," *Proc. SPIE*, vol. 3211, 1 1998.
- [51] A. Othonos and K. Kalli, *Fiber Bragg Gratings: Fundamentals and Applications in Telecommunications and Sensing, Chap. 3*. Artech House, 1999.
- [52] Y. J. Rao, D. A. Jackson, R. Jones, and C. Shannon, "Development of prototype fiber-optic-based fizeau pressure sensors with temperature compensation and signal recovery by coherence reading," *J. Lightwave Technol.*, vol. 12, no. 9, pp. 1685–1695, 9 1994.
- [53] Y.-J. Rao, "In-fibre bragg grating sensors," *Meas. Sci. Technol.*, vol. 8, 11 1997.
- [54] R. A. Bergh, H. C. Lefevre, and H. J. Shaw, "All-single-mode fiber-optic gyroscope," *Opt. Lett.*, vol. 6, pp. 198–200, 1981.
- [55] K. Bohnert, P. Gabus, J. Nehring, H. Brandle, and M. G. Brunzel, "Fiber-optic current sensor for electrowinning of metals," *J. Lightwave Technol.*, vol. 25, no. 11, pp. 3602–3609, 11 2007.
- [56] B. Culshaw, "Fiber optics in sensing and measurement," *IEEE J. Sel. Top. Quant. Electron.*, vol. 6, no. 6, pp. 1014–1011, 2000.
- [57] B. Culshaw, "Optical fiber sensor technologies: Opportunities and—perhaps—pitfalls," *J. Lightw. Technol.*, vol. 22, no. 1, pp. 39–50, 1 2004.
- [58] B. Lee, "Review of the present status of optical fiber sensors," *Opt. Fiber Technol.*, vol. 9, pp. 57–79, 8 2002.
- [59] J. Beller, "Otdrs and backscatter measurements," *D. Derickson (Ed.), Fiber Optic Test and Measurement*, pp. 434–474, 1998.
- [60] T. Horiguchi, T. Kurashima, and M. Tateda, "Tensile strain dependence of brillouin frequency shift in silica optical fibres," *IEEE Photon. Technol. Lett.*, vol. 1, 1989.
- [61] T. Horiguchi, K. Shimizu, T. Kurashima, M. Tateda, and Y. Koyamada, "Development of a distributed sensing technique using brillouin scattering," *J. Lightw. Technol.*, vol. 13, 1995.

- [62] D. Culverhouse, F. Farahi, C. Pannel, and D. Jackson, "Potential of stimulated brillouin scattering as sensing mechanism for distributed temperature sensors," *Electron. Lett.*, vol. 25, 1989.
- [63] A. Fellay, L. Thévenaz, M. Facchini, M. Niklès, and P. Robert, "Distributed sensing using stimulated brillouin scattering: towards ultimate resolution," in *Proc. 12th International Conference on Optical Fiber Sensors*, Williamsburg, VA, October 1997.
- [64] J. P. Dakin, D. J. Pratt, G. W. Bibby, and J. N. Ross, "Distributed optical fiber raman temperature sensor using a semiconductor light source and detector," *Electron. Lett.*, vol. 21, 1985.
- [65] H. GW, B. LA, C. TK, C. AG, C. RO, M. SF, and et al., "Structural control: past, present, and future," *J. Eng. Mech.*, vol. 123, pp. 897–971, 1997.
- [66] H.-N. Li, D.-S. Li, and G.-B. Song, "Recent applications of fiber optic sensors to health monitoring in civil engineering," *Engineering Structures*, vol. 26, pp. 1647–1657, 2004.
- [67] J. Hodgkinson and R. P. Tatam, "Optical gas sensing: a review," *Meas. Sci. Technol.*, vol. 24, no. 1, 2013.
- [68] S. Sekimotoa, H. Nakagawaa, S. Okazakia, K. Fukudaa, S. Asakuraa, T. Shigemorib, and S. Takahashib, "A fibr-optic evanescent-wave hydrogen gas sensor using palladium-supported tungsten oxide," *Sensors and Actuators B: Chemical*, vol. 66, pp. 142–145, 1 2000.
- [69] S. Okazakia, H. Nakagawab, S. Asakuraa, Y. Tomiuchic, N. Tsujic, H. Murayamad, and M. Washiyad, "Sensing characteristics of an optical fiber sensor for hydrogen leak," *Sensors and Actuators B: Chemical*, vol. 93, pp. 142–147, 8 2003.
- [70] S. Sumida, S. Okazaki, S. Asakura, H. Nakagawa, and T. H. Hideaki Murayama, "Distributed hydrogen determination with fiber-optic sensor," *Sensors and Actuators B: Chemical*, vol. 108, pp. 508–514, 7 2005.
- [71] J. Buerck, K. K. S. Roth, and H. Mathieu, "Otdr fiber-optical chemical sensor system for detection and location of hydrocarbon leakage," *J. Hazard. Mater.*, vol. 102, pp. 13–28, 8 2003.
- [72] L. D. Smullin and G. Fiocco, "Optical echoes from the the moon," *Nature*, vol. 194, p. 1267, 6 1962.
- [73] M. S. Patterson, B.Chance, and B. Wilson, "Time resolved reflectance and transmittance for the non-invasive measurement of tissue optical properties," *Applied Optics*, vol. 28, no. 12, pp. 2331–2336, 6 1989.
- [74] D. T. Delpy, M. cope, P. V. der Zee, S. Arridge, S. Wray, and J. Wyatt, "Estimation of optical pathlength through tissue from direct time of flight measurement," *Phys. Med. Biol.*, vol. 33, no. 12, pp. 1433–1442, 7 1988.
- [75] R. Lange, *3D time-of-flight distance measurement with custom solid-state image sensors in CMOS/CCD-technology*. University of Siegen, 6 2000.
- [76] R. Lange and P. Seitz, "Solid-state time-of-flight range camera," *IEEE Journal of Quantum Electronics*, vol. 37, no. 3, pp. 390–397, 3 2001.

REFERENCES

- [77] R. Lange, P. Seitz, A. Biber, and R. Schwarte, "Time-of-flight range imaging with a custom solid-state image sensor," *Laser Metrology and Inspection*, vol. 3823, 1999.
- [78] S. B. Gokturk, H. Yalcin, and C. Bamji, "A time-of-flight depth sensor – system description, issues and solutions," in *Conference on Computer Vision and Pattern Recognition Workshop, 2004*. IEEE, 6 2004.
- [79] S. O. Arik, D. Askarov, and J. M. Kahn, "Time-of-flight measurement with femtosecond light pulses," *Nat. Photonics*, vol. 2, pp. 733–737, Aug. 2010.
- [80] J. Kim, J. A. Cox, J. Chen, and F. X. Kärtner, "Drift-free femtosecond timing synchronization of remote optical and microwave sources," *Nat. Photonics*, vol. 2, pp. 733–736, 12 2008.
- [81] X. Y. Wang, D. M. Riffe, Y. S. Lee, and M. C. Downer, "Time-resolved electron-temperature measurement in a highly excited gold target using femtosecond thermionic emission," *Physical Review B*, vol. 50, no. 11, pp. 8015–8019, 9 1994.
- [82] P. R. Smith, D. H. Auston, and W. M. Augustyniak, "Measurement of gas field-effect transistor electronic impulse response by picosecond optical electronics," *Appl. Phys. Lett.*, vol. 39, no. 9, pp. 739–741, 9 1981.
- [83] J. Kim, Z. Z. J. Chen, F. N. C. Wong, and F. X. Kärtner, "Long-term femtosecond timing link stabilization using a single-crystal balanced cross-correlator," *Opt. Lett.*, vol. 32, pp. 1044–1066, 2007.
- [84] T. R. Schibli, O. K. J. Kim, J. Gopinath, S. N. Tandon, G. S. Petrich, L. A. Kolodziejski, J. G. Fujimoto, E. P. Ippen, and F. X. Kärtner, "Attosecond active synchronization of passively mode-locked lasers using balanced cross correlation," *Opt. Lett.*, vol. 28, no. 11, pp. 947–949, 1 2003.
- [85] *Fiber Optic Smart Structures*. Wiley, 1995.
- [86] M. Nikles, "Long-distance fiber optic sensing solutions for pipeline leakage, intrusion, and ground movement detection," in *Proc. SPIE 7316, Fiber Optic Sensors and Applications VI*, vol. 7216, Orlando, Florida, USA, 4 2009.
- [87] D. Inaudi and B. Glisic, "Long-range pipeline monitoring by distributed fiber optic sensing," *Journal of Pressure Vessel Technology*, vol. 132, 2 2010.
- [88] F. Tanimola and D. Hill, "Distributed fibre optic sensors for pipeline protection," *Journal of Natural Gas Science and Engineering*, vol. 1, pp. 134–143, 9 2009.
- [89] J. W. Ross, J. H. Riseman, and J. A. Krueger, "Potentiometric gas sensing electrodes," *Pure and Applied Chemistry*, vol. 36, 1973.
- [90] P. Clifford and P. Alto, "Selective gas detection and measurement system," *US Patent Specification*, vol. 4542640, 1985.
- [91] L. S. Rothman and etal, "The hitran 2008 molecular spectroscopic database," *J. Quant. Spectrosc. Radiat. Transfer*, vol. 110, pp. 533–572, 2009.

REFERENCES

- [92] C. S. Patterson, L. C. McMillan, C. Longbottom, G. M. Gibson, M. J. Padgett, and K. D. Skeldon, "Portable optical spectroscopy for accurate analysis of ethane in exhaled breath," *Meas. Sci. Technol.*, vol. 18, pp. 1459–1464, 2007.
- [93] D. G. Lancaster, D. Richter, and F. K. Tittel, "Portable fiber-coupled diode-laser-based sensor for multiple trace gas detection," *Appl. Phys. B*, vol. 69, pp. 459–465, 1999.
- [94] G. Stewart and et al, "Design of a fibre optic multi-point sensor for gas detection," *Sensors Actuators B*, vol. 51, pp. 227–232, 1998.
- [95] C. Y. Guan, F. J. Tian, Q. Dai, and L. B. Yuan, "Characteristics of embedded-core hollow optical fiber," *Opt. Express*, vol. 19, no. 120069-20078, 2011.
- [96] W. C. Swann and S. L. Gilbert, "Line centers, pressure shift, and pressure broadening of 1530–1560 nm hydrogen cyanide wavelength calibration lines," *J. Opt. Opt. Am. B*, vol. 22, pp. 1749–1756, 2005.
- [97] M. Krips, A. F. Crocker, M. Bureau, F. Combes, and L. M. Young, "Molecular gas in sauron early-type galaxies: detection of 13co and hcn emission," *Mon. Not. R. Astron. Soc.*, vol. 407, pp. 2261–2268, 2010.
- [98] *C-Band Wavelength Calibrator Hydrogen Cyanide Gas Cell H13C14N*.
- [99] Y.-L. Lo and C.-P. Kuo, "Packaging a fiber bragg grating with metal coating for an athermal design," *J. Lightwave Technol.*, vol. 21, pp. 1377–1383, 2003.
- [100] O. S. Wolfbeis, "Fiber-optic chemical sensors and biosensors," *Anal. Chem.*, vol. 74, pp. 2663–2677, 2002.
- [101] O. S. Wolfbeis, "Fiber-optic chemical sensors and biosensors," *Anal. Chem.*, vol. 76, no. 12, pp. 3269–3284, 6 2004.
- [102] O. S. Wolfbeis, "Fiber-optic chemical sensors and biosensors," *Anal. Chem.*, vol. 78, no. 12, pp. 3859–3874, 2006.
- [103] O. S. Wolfbeis, "Fiber-optic chemical sensors and biosensors," *Anal. Chem.*, vol. 80, no. 12, pp. 4269–4283, 2008.
- [104] X.-D. Wang and O. S. Wolfbeis, "Fiber-optic chemical sensors and biosensors (2008-2012)," *Anal. Chem.*, vol. 85, no. 487-508, 9 2012.
- [105] G. G. Cammann, E. A. Guilbault, H. Hal, R. Kellner, and O. S. Wolfbeis, *The Cambridge Definition of Chemical Sensors, ambridge Workshop on Chemical Sensors and Biosensors*. Cambridge University Press: New York, 1996.
- [106] G. Orellana and M. C. Moreno-Bondi, *Frontiers in Chemical Sensors: Novel Principles and Techniques*. New York: Springer, 2005.
- [107] F. Baldini, A. N. Chester, J. Homola, and S. Martellucci, *Optical Chemical Sensors*. New York: NA TO Science Series 224; Springer, 2006.

REFERENCES

- [108] Narayanaswamy and O. S. Wolfbeis, Eds., *Optical Sensors - Industrial, Environmental and Diagnostic Applications*. Springer, 2004, vol. 1.
- [109] C. McDonagh, C. S. Burke, and B. D. MacCraith, "Optical chemical sensors," *Chem. Rev.*, vol. 108, pp. 400–422, 1 2008.
- [110] Y. Mizuno, N. Hayashi, and K. Nakamura, "Distributed strain and temperature sensing based on Brillouin scattering in plastic optical fibers," in *23rd International Conference on Optical Fiber Sensors*, J. M. López-Higuera, J. Jones, M. López-Amo, and J. L. Santos, Eds., Santander, Spain, 6 2014.
- [111] Y. Matsumiya, T. Inoue, H. Watanabe, S. Kihara, and M. Ohshima, "Dielectric behavior of cis-polyisoprene in carbon dioxide under high pressure," *Nihon Reoroji Gakkaishi*, vol. 35, no. 3, pp. 155–161, 2007.
- [112] H. Suzumori, S. Honma, M. Morisawa, and S. Muto, "Plastic optical fiber sensor system for detection multi-point gas leakage," in *Advanced Material and Devices for Sensing and Imaging*, *Proc. of SPIE*, vol. 6829, 2007.

Appendix A

The development of optical fiber sensing based on pulse correlation in the lab

The concept of timing control using optical double-pulses correlation measurement was proposed in 2004 [?], [?]. The technique constructed a high resolution signal timing monitoring and control scheme for short optical pulses utilizing a high-speed optical-to-electrical (O/E) receiver, a phase comparator, a master clock, and a voltage controlled oscillator. Real time temperature and fiber tensile strain has been monitored by pulse correlation and differential measurement, obtaining 0.04 m°C resolution in temperature measurement, and 0.2 $\mu\epsilon$ resolution in fiber tensile strain measurement. Besides, the obtained linearity of temperature/fiber tensile strain-time difference change relationship was more than 99% [43]. However, polarization fluctuation caused by the birefringence in fibers or fiber links was observed in the correlation signals. Further study proposed a method to eliminate the polarization fluctuation over transmission line by the birefringence compensation approach putting a Faraday rotator mirror in a retraced fiber path [44]. The polarization fluctuation of the output correlation signal was suppressed by more than 15dB. Afterwards, the technique was applied to a time multiplexing fiber optic

APPENDIX A

temperature sensing system combining with 3- and 100-m long monitoring fibers to achieve high sensitive and dynamic measurable range [45]. On top of that, a multi-region quasi-distributed fiber tensile strain measurement was successfully demonstrated combining pulse correlation measurement and region selectable technique consisting of Fiber Bragg Grating (FBG) or partial reflectors [46],[47]. However, when applied to remote sensing, the technique suffered from long term instability at transmission line, i.e., time drift fluctuation and polarization instability. A method to eliminate the long term time drift was proposed in 2012 [48], using a remote reference pulse against the time drift fluctuation caused by the long transmission line. Remote temperature monitoring over the 30 km-long transmission line was demonstrated utilizing a remote reference pulse and obtained good linearity of the time drift value with respect to the temperature around the sensing region.

List of Figures

1.1	Fountain sparkles with light from an arc lamp, illustrated by Colladon in 1884 [3].	2
1.2	Structure of step-index fibers. (a) Light propagation. (b) Cross section. (c) Refractive index distribution.	4
1.3	Structure of graded-index fibers. (a) Light propagation. (b) Cross section. (c) Refractive index distribution.	4
1.4	Scanning electron micrographs of microstructure fibers	6
1.5	Principle of optical fiber sensors	7
1.6	Time drift in optical fibers.	10
1.7	Pulse correlation measurement	10
1.8	Configurations of optical fiber sensors.	12
1.9	Optical fiber sensors for civil structure measurement.	14
1.10	Optical fiber sensors used in deep sea monitoring.	15
1.11	Optical fiber sensors for gas detection.	16
2.1	Fiber sensing based on pulse correlation measurement.	23
2.2	SHG output with respect to time drift τ between two pulses. Inset figures show the time-position relationship between the reference pulse (the red solid line) and the monitoring pulse (the blue dashed line). The shaded and the remaining regions correspond to the pulse independent term $G_2(0)$ and the pulse correlation term $G_2(\tau)$ in the SHG output, respectively.	25
2.3	Polarization fluctuation caused SHG signal degradation.	29
2.4	Polarization fluctuation suppression Faraday rotator	30

LIST OF FIGURES

2.5	Polarization fluctuation suppression polarization scrambled pulse train (PSP). The pulses in black color are the ones did not experience polarization fluctuation, the pulses in red color are the ones experienced polarization fluctuation.	31
2.6	(a) PMP with 45° linear polarization. V and H show the vertical and the horizontal polarization, respectively, and T_c is the coherence time of optical pulses. (b) PSP. The dark blue rotating arrows below each pulse show the polarization state. (c) Setup to generate the PSP from the PMP. The temporal delay in the delay line is set to be larger than the coherence time T_c and be integral multiple of the repetition period T	32
2.7	Experimental setup of the SHG pulse correlation measurement using the PMP or the PSP under polarization fluctuation.	33
2.8	Comparison of the pulse correlation terms in the SHG output at $\tau = 0$ induced by (a) the PMP and (b) the PSP during the variation of polarization state. . . .	34
2.9	Schematic of optical pulse correlation sensing technique.	35
2.10	(a) Schematic of PMP-based multi-region's optical pulse correlation sensing. (b) Different polarization impacts on signals at two regions.	37
2.11	(a) Schematic of PSP-based wide region optical pulse correlation sensing. (b) Stabilized signals of different regions.	38
2.12	Experimental setup of demonstration of PMP and PSP-based optical pulse cor- relation sensing. Region 1 was demonstrated as polarization fluctuation on trans- mission line. Region 2 was used as strain sensing region.	40
2.13	Comparison of differential signal of optical pulse correlation sensing based on PMP and PSP during the variation of polarization state. (a) Results of PMP based correlation. (b) Results of PSP based correlation. Blue and red lines were obtained when wave plates were adjusted at $(\lambda/2, \lambda/4)=(150^\circ, 180^\circ)$ and $(\lambda/2, \lambda/4)=(60^\circ, 90^\circ)$, respectively.	41
2.14	Comparison of system sensitivities of optical pulse correlation sensing based on (a) PMP and (b) PSP during the variation of polarization state.	41

2.15	Results of strain measurement of PSP based optical pulse correlation sensing. (a) Illustration of time difference, (b) Time difference change versus strain demonstration at short distance (0.2 m). (c) Experimental results of strain demonstration of remote monitoring (1 km).	43
2.16	Schematic configuration of multi-region optical pulse correlation sensing.	44
2.17	The output power P_{out} and the interference power P_m depend on the reflectivity of the partial reflector. Assuming the number of sensing regions $N=100$, the fiber loss factor $\alpha=0.2\text{dB/km}$, and the length of each sensing region $L=10\text{m}$	45
2.18	Central peak of the slope of output signal changes along with the dispersion width factor δ	47
2.19	Pulse broadening factor changes as a function of propagation distance z for a Gaussian pulse propagating in the fiber. The blue curve corresponds to the case of an unchirped pulse. The green curves are obtained for chirp parameter $C=2$	49
2.20	Temperature dependence of the chromatic dispersion.	50
3.1	Conceptual schematic of the gas sensing for a long distance pipeline.	55
3.2	Conceptual schematic of the gas sensing for a long distance pipeline.	55
3.3	Hydrogen cyanide $\text{H}^{13}\text{C}^{14}\text{N } 2\nu_3$ rotational-vibrational band spectrum [96].	57
3.4	Imitation of gas leakage in pipeline using gas cell with fibers.	58
3.5	Schematic of tele-spectroscopy gas sensing.	59
3.6	Absorption signal of reflected signal and normalized figure.	61
3.7	Schematic of three-region gas sensing demonstration. Setup of three-region gas sensing demonstration.	65
3.8	Synchronization of the FBG peak and absorption line.	65
3.9	Absorption spectra of three-region gas sensing system under different gas leakage occurrences.	67
3.10	Absorption spectra of long distance gas sensing system under different gas leakage occurrences.	70
3.11	Wavelength shift at 1547.4nm over kilometer distance.	74

LIST OF FIGURES

3.12	Wavelength shift of FBG sensor monitor in long distance.	74
3.13	The concept of the extension technique of the number of sensing regions.	75
3.14	Instrument layout for 2 regions demonstration. L1=1km, L2=2.005km.	77
3.15	Experimental results of the extension of sensing regions demonstration.	79
4.1	Principle of OTDR based on Rayleigh scattering.	84
4.2	Molecular structure of cis isoprene.	86
4.3	Refractive index reduction of PIP against time in the presence of hydrocarbon gases [112].	86
4.4	Schematic of POF sensor head and the polymer swelling in the presence of hydrocarbon gas.	88
4.5	Connection loss from POF to silica fiber using pipes.	90
4.6	Connection loss from POF to silica fiber: using pipes.	91
4.7	Connection loss from POF to silica fiber: using fiber collimator and GRIN lens.	92
4.8	Connection loss from POF to silica fiber: using fiber collimator and large diameter silica MMF.	92
4.9	Connection loss from POF to silica fiber: using fiber collimator and normal silica MMF.	92
4.10	Connection loss from POF to silica fiber: using fiber collimator and large diameter POF.	93
4.11	Connection loss from POF to silica fiber: using matching oil.	93
4.12	Experimental demonstration using OTDR, POF, and ethyl alcohol.	94
4.13	Fresnel reflection at the POF-air interface and the POF-alcohol interface.	96
4.14	Fresnel reflection at the POF-air interface and the POF-water interface.	98
5.1	Index change of suspended core optical fiber in the presence of gas cloud.	104
5.2	Schematic of evanescent gas sensing using suspended core optical fiber with air holes on its surface.	105
5.3	Suspended core optical fiber for gas detection.	105

List of Tables

3.1	Measured and estimated pressure dependence of line P ₇ of HCN13 under varied pressures.	63
3.2	Experimental measurement of the displayed wavelength shift of FBG sensor monitor over different transmission distances. The original wavelength under test is 1547.4nm	76
4.1	Comparison of systems constructed by different types fibers	89
4.2	Refractive index of GI-POF, ethyl alcohol, and water	94

LIST OF TABLES

Glossary

APD	avalanche photodiode
BOTDR	Brillouin Optical Time-domain Reflectometer
CSU	correlation sensing unit
CW	continuous wave
DFB	distributed feedback
EFPI	Extrinsic Fabry-Perot interferometer
EMI	electromagnetic interference
FBG	fiber Bragg grating
FOC	Fiber-optics chemical sensor
FOG	fiber optic gyroscope
FPI	Fabry-Perot interferometer
FWHM	full width at half maximum
GI	graded index
GI-POF	graded-index plastic optical fiber
GRIN lens	graded-index lens
GS-LD	Gain-switched laser diode

GLOSSARY

HWP	half wave plate
LD	laser diode
LPFG	long-period fiber grating
MMF	multimode fiber
MZI	Mach-Zehnder interferometer
OTDR	optical time domain reflectometer
PC	polycarbonate
PCF	photonic-crystal fiber
PFBVE	perfluoro-butenylvinylether
PIP	Cis-Polyisoprene
PMMA	polymathy methacrylate
PMP	polarization maintained pulse train
POF	plastic optical fiber
PS	polystyrene
PSP	polarization scrambled pulse train
QWP	quarter wave plate
SHG	second harmonic generation
SHM	structural health monitoring
SMF	single mode fiber
TOF	time-of-flight

Acknowledgement

I would like to express my deepest thanks to my advisers, Prof. Katsushi Iwashita, Prof. Koji Nonaka, and Dr. Hirokazu Kobayashi, for their patient guidance and encouragement throughout the research. Different styles they have, I've seen the attitude and substance of an excellent researcher and teacher from all of them: the spirit of continual innovation in research, and an excitement in teaching. Without their support, supervision, and constant help this dissertation would not have been possible. It is such a big luck to have their guidance not only for research but also for life.

I would like to send my sincere gratitude to Prof. Akimitsu Hatta and Prof. Hiroshi Furusawa for being in my committee and for their valuable suggestions.

Special appreciation is given to my master degree's supervisor, Prof. Libo Yuan in Harbin Engineering University, who is also the collaborator of my Ph.D research project, for having recommended me to KUT, and for the fruitful discussions on my study. I would like to send my deep gratitude to Prof. Yuan for his constant help in my life and career. I would also like to thank Prof. Jun Yang in Harbin Engineering University for his help with my research.

I would like to acknowledge all my Chinese friends in KUT for their precious friendship, tremendous help and encouragement.

I would like to thank all my colleagues and friends in the lab, especially Mr. Yusuke Kohashi, for the great help with my life in Japan.

I also thank to the support of SSP of KUT.

My sincerely thanks but not the last belong to family, my dear parents, my brothers, my sisters in law and their little kids, for their love and supports.

ACKNOWLEDGEMENT

Publications

Journal papers

- 1) Mifang Lu, Horokazu Kobayashi, Koji Nonaka, “Polarization-Stabilized Pulse Correlation Measurement for Remote Fiber Sensing Using Polarization Scrambled Pulses,” *Jpn. J. Appl. Phys.*, vol. 52, no. 12R, pp. 126603-1–126603-8, Nov. 2013
- 2) Mifang Lu, Koji Nonaka, Hirokazu Kobayashi, Jun Yang, Libo Yuan, “Region selectable gas sensing for long distance pipeline maintenance,” *Meas. Sci. Technol.*, vol. 24, no. 9, pp. 095104-1–095104-8, Aug. 2013
- 3) Wang Xue, Lu Mifang, Yang Jun, Yuan Libo, “Twin-core Fiber-based Long Period Fiber Grating and Its Coupling Characteristics,” *Acta Optica Sinica*, vol. 30, no. 12, pp. 3391–3397, Dec. 2010

International Conferences

- 1) Mifang Lu, Hirokazu Kobayashi, Koji Nonaka, “Suppression of polarization instability in optical pulse correlation remote sensing,” in *23rd International Conference on Optical Fiber Sensor (OFS)*, Santander, Spain, Jun. 2014
- 2) Mifang Lu, Koji Nonaka, Hirokazu Kobayashi, “Extension of number of sensing regions on tele-optical fibre gas spectroscopy by partial reflectors,” in *The 4th International Symposium for Frontier Technology (ISFT)*, Shenyang, China, Jul. 2013
- 3) Mifang Lu, Koji Nonaka, Hirokazu Kobayashi, Jun Yang, Libo Yuan, “Region selectable gas sensing for long distance pipeline maintenance,” in *22nd International Conference on Optical Fiber Sensors (OFS)*, Beijing, China, Oct. 2012

Domestic Conferences

- 1) Hirokazu Kobayashi, Mifang Lu, Xunjian Xu, Koji Nonaka, "Suppression of polarization instability on wide area fiber sensing using polarization scrambled pulse train," in *51th Meeting on Lightwave Sensing Technology (LST)*, Tokyo, Japan, Jun. 2013
- 2) Mifang Lu, Koji Nonaka, Hirokazu Kobayashi, Jun Yang, Libo Yuan, "Region selectable gas sensing for pipeline tele-monitoring," in *The Society Conference of IEICE*, Yamanashi, Japan, Sep. 2012